High-Directive Metasurface Printed Antennas for Low-Profile Applications

by

Mohammed Alharbi

A Dissertation Presented in Partial Fulfillment
of the Requirement for the Degree
Doctor of Philosophy

Approved June 2020 by the
Graduate Supervisory Committee:

Constantine A. Balanis, Chair
James T. Aberle
Joseph Palais
Georgios C. Trichopoulos

ARIZONA STATE UNIVERSITY

August 2020

ABSTRACT

Since the advent of *High Impedance Surfaces (HISs)* and *metasurfaces*, researchers have proposed many low profile antenna configurations. HISs possess in-phase reflection, which reinforces the radiation, and enhances the directivity and matching bandwidth of radiating elements. Most of the proposed dipole and loop element designs that have used HISs as a ground plane, have attained a maximum directivity of 8 dBi. While HISs are more attractive ground planes for low profile antennas,these HISs result in a low directivity as compared to PEC ground planes. Various studies have shown that Perfect Electric Conductor (PEC) ground planes are capable of achieving higher directivity, at the expense of matching efficiency, when the spacing between the radiating element and the PEC ground plane is less than 0.25λ.

To establish an efficient ground plane for low profile applications, PEC (Perfect Electric Conductor) and PMC (Perfect Magnetic Conductor) ground planes are examined in the vicinity of electric and magnetic radiating elements. The limitation of the two ground planes, in terms of radiation efficiency and the impedance matching, are discussed. Far-field analytical formulations are derived and the results are compared with full-wave EM simulations performed using the High-Frequency Structure Simulator (HFSS).

Based on PEC and PMC designs, two engineered ground planes are proposed. The designed ground planes depend on two metasurface properties; namely in-phase reflection and excitation of surface waves. Two ground plane geometries are considered. The first one is designed for a circular loop radiating element, which utilizes a circular HIS ring deployed on a circular ground plane. The integration of the loop element with the circular HIS ground plane enhances the maximum directivity up to 10.5 dB with a 13% fractional bandwidth. The second ground plane is designed for a square loop radiating element. Unlike the first design, rectangular HIS patches

are utilized to control the excitation of surface waves in the principal planes. The final design operates from 3.8 to 5 GHz (27% fractional bandwidth) with a stable broadside maximum realized gain up to 11.9 dBi. To verify the proposed designs, a prototype was fabricated and measurements were conducted. A good agreement between simulations and measurements was observed.

Furthermore, multiple square ring elements are embedded within the periodic patches to form a surface wave planar antenna array. Linear and circular polarizations are proposed and compared to a conventional square ring array. The implementation of periodic patches result in a better matching bandwidth and higher broadside gain compared to a conventional array.

To my beloved Family

ACKNOWLEDGEMENTS

First and foremost all praise goes to Allah (God), the Almighty, for giving me the blessing, the strength, the opportunity and endurance to complete my Ph.D. degree.

I am especially grateful to all of my family for their love, support, and unwavering belief in me. My deepest gratitude goes to my beloved parents, Saeed and Zakiah Alharbi, and to my brothers and sisters for their endless prayers and encouragements despite the long distance between us. I am deeply thankful to my wife, Neda Kasim, for her enormous understanding, constant support and patience during my study. You have been my great companion and best friend, and unending inspiration. My two bundles of joy, Malak and Omar, have continuously provided the much-needed breaks from research and the motivation to finish my degree with expediency. Special thanks to my father-in-law and brothers-in-law for all support and the great times. Without such a wonderful family, I doubt that I would be in this place today.

I would like to express my sincere gratitude to my advisor Professor Constantine A. Balanis, for his guidance, advice, and support throughout this thesis. Without his knowledge and time this research work would not have been possible. The continuous feedback in the weekly meetings, and the valuable comments when reviewing all manuscripts and this dissertation are deeply appreciated. It has been pleasure and honor to have him as my advisor.

I would also like to express my gratitude to the committee members Professor James Aberle, Professor Georgios Trichopoulos and Professor Joseph C. Palais for their valuable suggestions and feedback. Special thanks to Craig Birtcher for the technical training, all suggestions in the weekly meetings, and for performing all fabrications and measurements needed for this dissertation.

I also want to extend my thanks to my former and current labmates Dr. Siva Pandi, Dr. Saud Saeed, Dr. Wengang Chen, Dr. Mikal Amiri, Dr. Subramanian Ramalingam, Dr. Anuj Modi and Dr. Meshaal Alyahya for the technical discussions, creating a joyful environment.

Finally, I would like to thank KACST (King Abdulaziz City for Science and Technology) for their generous financial support and scholarship to complete my Ph.D degree. Special thanks to the Saudi Arabian Cultural Mission (SACM) in the United States for their valuable support during my study.

TABLE OF CONTENTS

Page

LIST OF TABLES ix

LIST OF FIGURES x

CHAPTER

1 INTRODUCTION 1

1.1 Previous Work 1

1.2 Scope of the Work 5

2 PERFORMANCE OF THE RADIATING ELEMENT ABOVE PEC AND PMC GROUND PLANES 8

2.1 Electric Radiating Element 9

2.1.1 PEC Ground Plane 9

2.1.2 PMC Ground Plane 12

2.2 Magnetic Radiating Element 15

2.2.1 PMC Ground Plane 15

2.2.2 PEC Ground Plane 19

2.3 Physical Explanation 22

3 REFLECTION BEHAVIOR OF ENGINEERED SURFACES 24

3.1 Corrugated PEC Plate 24

3.2 Dielectric Covered PEC 27

3.3 Mushroom-Like Surface 30

3.4 Circularly Symmetric Surface 33

4 DISPERSION AND MATERIAL CHARACTERIZATION 37

4.1 Corrugated PEC 37

4.2 Dielectric Covered Flat PEC 40

4.3 Multi-Dielectric Covered Flat PEC 43

CHAPTER Page

4.4 Metasurface 47
4.4.1 Square Metasurface 47
4.4.2 Annular Sector Patch Metasurface 50
4.5 Extracting Resonances From Dispersion Diagrams 52
4.5.1 Rectangular Patch Dispersion and Resonances 53
4.5.2 Metasurface Resonances 54
5 HYBRID CIRCULAR GROUND PLANES FOR HIGH REALIZED GAIN LOW-PROFILE LOOP ANTENNAS 57
5.1 Introduction 57
5.2 Loop Antenna on Grounded Dielectric 58
5.3 Loop Antenna Loaded with Annular Sector HIS 61
5.4 Loop Antenna Above the Proposed Hybrid Ground Plane 68
5.5 Fabrication and Measurements 73
6 PERFORMANCE ENHANCEMENT OF SQUARE-RING ANTENNAS EXPLOITING SURFACE-WAVE METASURFACES 78
6.1 Introduction 78
6.2 Surface Waves and HIS Resonances 79
6.3 Ring Antenna and Metasurfaces 82
6.4 Impact of Surface-Wave Resonances on Performance of RWMS 89
6.5 Fabrication and Measurements 94
7 LINEAR AND CIRCULAR POLARIZED METASURFACES ANTENNA ARRAY UTILIZING SQUARE-RING ELEMENT 98
7.1 Introduction 98
7.2 1x4 Linearly Polarized Metasurface Array 100

CHAPTER Page

7.3 2x2 Circularly Polarized Metasurface Array 104
7.4 Fabrication and Measurements 110
8 CONCLUSIONS AND FUTURE WORK 113
8.1 Conclusions 113
8.2 Future Work 114
REFERENCES 117

LIST OF TABLES

Table Page

5.1 Dimensions of the Loop Antenna 59

5.2 Dimensions of the Circular HIS 63

5.3 Dimensions of the Proposed Ground Plane. 70

6.1 Surface Wave and HIS Resonances 82

LIST OF FIGURES

Figure Page

2.1 (a) Electric Dipole Above PEC. (b) Electric Dipole Above PMC. 9

2.2 Horizontal Electric Dipole Above PEC Ground Plane. 10

2.3 Comparison Between the Directivity of a Horizontal Electric Dipole at a Height h Above a PEC Ground Plane Obtained Using HFSS and the Derived Analytical Expression of (2.7). 12

2.4 Horizontal Electric Dipole Above PMC Ground Plane. 13

2.5 Comparison Between the Directivity of a Horizontal Electric Dipole at a Height h Above a PMC Ground Plane Obtained Using HFSS and the Derived Analytical Expression of (2.14). 14

2.6 The Analogy of Laser and a Narrow Beam Lens Integration for Higher Directivity. 15

2.7 (a) Horizontal Magnetic Dipole Above PEC. (b) Horizontal Magnetic Dipole Above PMC. 16

2.8 Horizontal Magnetic Dipole Above PMC Ground Plane. 17

2.9 Equivalent Horizontal Magnetic Dipole Above a PMC Ground Plane. . . 18

2.10 Comparison Between Directivity of a Horizontal Magnetic Dipole at a Height h Above a PMC Ground Plane Obtained Using HFSS and the Derived Analytical Expression of (2.21). 19

2.11 Horizontal Magnetic Dipole Above PEC Ground Plane. 20

2.12 Comparison Between the Directivity of a Horizontal Magnetic Dipole at a Height h Above a PEC Ground Plane Obtained Using HFSS and the Derived Analytical Expression of (2.28). 21

Figure Page

2.13 Field Distribution (a) Uniform Distribution. (b) TE_{10}-mode Distribution. 22
2.14 Field Distribution for an Electrical Dipole Above (a) PEC. (b) PMC. . . 23
2.15 Field Distribution for a Magnetic Dipole Above (a) PMC. (b) PEC. . . . 23
3.1 Geometry of a Corrugated Surface. 25
3.2 HFSS Simulation Setup for Corrugated PEC. 26
3.3 Reflection Phase Comparison for Different Corrugated PEC Dimensions. 27
3.4 Grounded Dielectric Geometry. 28
3.5 HFSS Setup to Calculate the Reflection Phase of a Grounded Dielectric. 29
3.6 Reflection Phase Comparison for Different Dielectric Materials Covering a PEC Plate. 30
3.7 Geometry of a Mushroom-Like Surface (a) Side View. (b) Top View. . . 31
3.8 Appropriate Boundary Conditions for Simulating Unit Cells. 32
3.9 Reflection Phase of a Unit Cell. 33
3.10 Geometry of a Circular HIS. 34
3.11 Unit Ring of a Circular HIS. 35
3.12 Reflection Phase of a Circular HIS Unit. 36
4.1 Geometry of a Corrugated Surface, with Its Equivalent Transmission Line Model. 38
4.2 Corrugated Surface Setup to Calculate the Dispersion in HFSS. The Letters M and S Printed on the Wall Represent the Assigned Master and Slave Boundary Conditions. 39
4.3 Analytical and Simulation Comparison of the Calculated Dispersion Diagram of a Corrugated PEC. 40

Figure Page

4.4 Geometry of a Grounded Dielectric, with Its Equivalent Transmission Line Model. 41
4.5 HFSS Setup for Calculating the Dispersion Diagram. The Master (M) and Slave (S) Boundary Conditions are Assigned to the Walls. 42
4.6 Dispersion Diagram for a Dielectric Covered PEC. Left: Rogers RT/Duroid 5880 ($\varepsilon_r = 2.2$). Right: Rogers RT/duroid 6010 ($\varepsilon_r = 10.2$). 42
4.7 Geometry of Multiple Dielectric Materials Covering a Flat PEC, and Its Equivalent Transmission Line Model. 43
4.8 Geometry of a Corrugated Dielectric on a Flat PEC, with Its Equivalent Transmission Line Model. 45
4.9 Dispersion of Two Side-by-Side Dielectric Materials Covering a PEC with Different Lengths for the Two Substrates. 46
4.10 Dispersion of a Corrugated Dielectric (Rogers RT/Duroid 5880) Covering a PEC. 46
4.11 Transverse Resonance Method for a Metasurface Unit Cell. 47
4.12 HFSS Setup to Extract the Dispersion of a Square Metasurface. 49
4.13 Analytical and Simulated Comparison of Dispersion Diagrams of a Square Metasurface. 49
4.14 Layout of an Annular Sector Metasurface Unit Cell. 50
4.15 Dispersion of Different Shapes of Patches Loaded on a Rounded Dielectric. 51
4.16 Approximate Dispersion of the Annular Sector Metasurface. 52
4.17 Dispersion of a Parallel Plate Filled with Rogers RT/Duroid 5880 Dielectric. 54

Figure Page

4.18 The Impact of Doubling the Electrical Length on the Possible Resonances. 55
4.19 Dispersion of Multiple Periods of Rectangular Metasurfaces. 56
5.1 A Loop Antenna Printed on a Grounded Dielectric. 59
5.2 Current Distribution Along the Circumference of the Printed Loop. 60
5.3 Simulated Broadside Directivity of the Loop Antenna Above a Grounded Dielectric. 61
5.4 Simulated S_{11} of the Loop Antenna Placed Above a Grounded Dielectric. 61
5.5 Loop Element Surrounded by Annular Sector at Each Side. 62
5.6 Geometry of the Loop Along with HIS Section Positioned on the Top Surface of the Grounded Dielectric. 63
5.7 Dispersion Diagram for Annular Sector. 64
5.8 Simulated S_{11} of the Loop in the Vicinity of the HIS and Grounded Dielectric. 65
5.9 Simulated Broadside Directivity of the Loop Surrounded by Periodic Annular Patches and Above Grounded Dielectric. 65
5.10 The Magnitude and Phase of the E-Field Inside the Substrate. 66
5.11 HFSS Setup to Calculate the Reflection Phase of Annular Sector Unit Cell. 67
5.12 The Simulated Reflection Phase for Annular Sector Unit Cell. 67
5.13 The Maximum Directivity of a Dipole as a Function of Length. 68
5.14 The Proposed Ground Plane with a Printed Loop Placed in the Middle. 69
5.15 The Input Impedance and the Broadside Directivity as a Function of p_b. 70

Figure Page

5.16 Simulated Reflection Coefficient of the Loop Antenna Above the Three Different Ground Planes. 72
5.17 Simulated Broadside Directivity of the Loop Antenna Above the Three Different Ground Planes. 72
5.18 Sectional View of the Proposed Antenna. 73
5.19 A Photograph of the Fabricated Antenna. 74
5.20 (a) Return Loss Measurement Setup. (b) Radiation Pattern Measurement Setup. 75
5.21 Comparison of the Measured and the Simulated Reflection Coefficients. 76
5.22 Comparison of the Measured and the Simulated Broadside Realized Gain. 76
5.23 Comparison of the Measured and the Simulated Amplitude Radiation Patterns at 3 GHz. 77
6.1 (a) Dispersion Diagram and (b) Reflection Phase of Various Unit Layouts. The Design Parameters (in mm): $h_1 = 5.08$, $h_2 = 1$, $p_x = 20.5$, $p_y = 12.5$, $l = 16$, $w = 9$. 80
6.2 Different Configurations of the Ring Element in Vicinity of the MS. The Design Parameters are: $h_1 = 5.08$ mm, $h_2 = 1$ mm, $l = 16$ mm, $w = 9$ mm, $g_x = 4.5$ mm, $g_y = 3.5$ mm, $w_i = 11$ mm, $w_o = 20$ mm, $l_s = 61.5$ mm, $w_s = 50$ mm. The Coaxial Dielectric is Teflon ($\varepsilon_r = 2.08$) with a Diameter (d_o) of 4.1 mm. 83

Figure Page

6.3 (a) Real Part of Input Impedance, and (b) Reflection Coefficient for the Different Designs Illustrated in Fig.6.2. 85
6.4 (a) Broadside Realized Gain of the Various Configurations, with Inset Showing the Radiation Pattern for RAMS at 4.9 GHz. (b) Normalized Magnitude of E_z Inside the Substrate, with Inset Displaying the Position (Dotted White Line) of the Extracted Field. 88
6.5 Impact of Varying the Length of the Periodic Patches on Reflection Coefficient (a) and Broadside Realized Gain (b). 90
6.6 Impact of Sweeping the Width of the Periodic Patches on the Reflection Coefficient (a) and Broadside Realized Gain (b). 92
6.7 Impact of Varying the Substrate Size on Reflection Coefficient (a) and Broadside Realized Gain (b). 94
6.8 Different Views of the Fabricated Prototype of the RWMS Design..... 95
6.9 Comparison Between Simulated and Measured Data. (a) Reflection Coefficient. (b) Broadside Realized Gain ($\theta = 0°$, $\phi = 0°$)..... 96
6.10 Comparison Between Simulated and Measured Radiation Patterns of the RWMS Design at Two Frequencies (4 and 5 GHz) at $xz-$ and $yz-$Planes. 97

Figure Page

7.1 1x4 Square Ring Elements Embedded Within Metasurface and Excited with (a) Four Coaxial Probes and (b) Feed Network. The RWMS Parameters are: w_i = 10 mm, w_o =20 mm, l = 16 mm, w= 9 mm, g_x = 4.5 mm, and g_y = 3.5 mm. The Feed Network Parameters are: l_1 = 96.3 mm, l_2 = 10 mm, l_3 = 11.85 mm, l_4 = 25.65 mm, l_5 = 10 mm, l_6 = 11.85 mm, l_7 = 9.29 mm, l_8 = 6.9 mm, g_s = 2.74 mm, v = 1.143 mm, w_{50}= 1.1 mm, and w_{70}= 0.7 mm. 101

7.2 S-Parameters for the 1x4 RWMS Array. 103

7.3 Broadside Realized Gain for the 1x4 RWMS Scheme. 104

7.4 2x2 Square Ring Elements Embedded Within Metasurface and Excited with (a) Four Coaxial Probes, and (b) Feed Network. 105

7.5 S-Parameters for the 2x2 RWMS Array. 106

7.6 Broadside RHCP Gain and Axial Ratio for 2x2 RWMS Scheme. 108

7.7 Delivered Current Magnitude to Each Ring Element (a), and Current Phase Difference Between Adjacent Elements (b). 109

7.8 Top and Bottom Views of the Fabricated Prototype of the 2x2 RWMS Array Incorporated with the Feed Network. 110

7.9 Comparison Between Simulated and Measured Reflection Coefficient, RHCP Broadside Gain, and Axial Ratio. 111

7.10 Simulated and Measured Radiation Patterns at xz- and yz-Planes. 112

8.1 Geometry of RWMS Leaky-Wave Structure. 115

8.2 Geometry of Conventional Square Ring Array and RWMS Array. 116

Chapter 1

INTRODUCTION

The rapid improvement in technology and computational analyses for electromagnetic applications contributed in increasing the complexity of antenna designs. These advances decrease the required time to analyze most electromagnetic designs and provide a deeper intuitive understanding of the topic under investigation. One major breakthrough that has contributed greatly to the antenna technology was the introduction of mushroom structures proposed in 1999 [1]. While perfect magnetic conductors (PMCs) do not exist in nature, synthetic mushroom structures alter the boundary condition, and resemble AMC behavior over a range of frequencies. This allows antenna engineers to develop new designs that meet requirements of modern communication technology. Several studies [2–5] conducted on synthetic mushroom structures have resulted in interesting phenomena when integrated with radiating elements. This integration solves one of the major challenges that the antenna community faces, which is to reduce the coupling between the antenna and the ground plane in low-profile configurations. It leads to a series of novel low-profile antenna designs that meet the requirements of modern communication systems such as GPS, WiFi, satellite and mobile communications.

1.1 Previous Work

Placing a radiating element above a ground plane has been investigated extensively in the past decades. Although perfect electric conductor (PEC) and perfect magnetic conductor (PMC) ground planes introduce unique characteristics, there are several limitations when they are placed in the vicinity of radiating elements. For instance,

a radiating element can be placed at a very close distance above a PMC ground plane. However, a minimum distance of 0.25λ is required when the ground plane is PEC so that the reflected field is in-phase and the two, direct and reflected, form a constructive interference. This exemplifies a reason as to why PMC ground planes are more attractive for low-profile applications. As PMCs do not exist in nature, synthetic metasurfaces have been developed, which mimic AMC characteristics.

The two most attractive characteristics that metasurfaces possess, when integrated with radiating elements, are surface wave excitation/suppression and in-phase reflection [1]. These types of behavior, depending on the design of the metasurface structure, might occur at the same or at a different frequency range [6]. The presence of surface waves in antennas sometimes is considered as a major drawback because they impact the performance of the radiating element by reducing the radiation efficiency, directivity, and gain [7]. When mushroom-like structures are used to suppress surface waves, the structure is identified as an Electromagnetic Band Gap (EBG) surface. As a result, a number of applications have been developed which use the feature of EBG to optimize the antenna performance [8, 9].

The second interesting feature of mushroom-like structures is to ideally reflect the incident wave with a magnitude of nearly unity and zero phase over a certain bandwidth [1]. To distinguish this feature in a mushroom-like structure, the surface is referred to as a High Impedance Surface (HIS), which enables practitioners to use it as a ground plane in antenna designs. Low profile is one of the modern communication requirements for antennas, and it is especially important for aerodynamic and low-observable radar applications [6]. The introduction of HISs has increased the number of novel low-profile antenna designs, where a variety of configurations have been proposed for different radiating elements such as dipoles, loops, and spirals [10], [11], [12]. HISs have attracted investigators to explore different geometries that are needed

for various antenna applications, such as conformal and curved cartesian HIS designs [13], [14], and circular HIS [15–17]. An investigation has explored the performance of curvilinear radiating elements above couple of HIS geometries and has determined that the circular HIS is a better choice as a ground plane for curvilinear radiating elements [15].

Circularly symmetric structures have been examined extensively in the field of Optics and Lasers [18], and they were adapted and integrated with EBG and HIS structures for RF antenna applications. One example of an EBG circular structure has been proposed in [19], where the structure was designed to suppress surface waves in all directions of printed antennas. Another circularly periodic EBG structure has been reported in [20] to increase the gain of a microstrip patch antenna. Besides circular EBG structures, a few studies [12], [15] have proposed HIS circular structures to enhance the gain and the operational bandwidth of loop and spiral radiating elements.

Modern communication applications frequently require highly directive radiation allowing long distance communications, less coupling with unwanted signal and higher power performance in the broadside direction. While HIS surfaces are known to be superior ground planes for low profile antennas, one limitation of these surfaces is that they result in low directivity, compared to PEC ground planes. When a radiating element is placed less than a quarter wavelength above a ground plane, PEC ground planes are capable of achieving higher directivity compared to PMC [21], [22]. While these studies were conducted using the finite element method (Ansys HFSS) and electromagnetic numerical methods (NECPro), no analytical formulation with physical interpretation has been provided as to why PEC ground planes lead to higher directivity than PMC.

Although HIS ground planes are used in most of the current low-profiles antenna designs, a few studies have examined the use of PEC for low-profile configurations.

One obstacle to the use of PEC is that as the spacing is reduced between the radiating element and the PEC, a reduction in the radiation resistance of the radiating element as well as an increase in reactance are observed, thus degrading the total radiation efficiency. One approach that overcomes this challenge is to increase the free space impedance of the radiating element to be at least hundreds of ohms [21]. This can be achieved for a dipole antenna by replacing the thin linear wire with folded multiple arms. Thus, a folded dipole placed closely above a PEC ground plane (0.02λ) has been shown to improve the radiation efficiency and a gain of 8.7 dB was achieved [21]. However, one limitation of this design is that it has a narrow fractional bandwidth (2.2 %) due to their high quality factor ($Q = 91.2$). Another approach to improve the radiation resistance of the dipole, when placed closely above PEC, is to load the dipole with a parasitic strip. A half-wave dipole positioned 0.05λ above a PEC ground plane, with a parasitic strip placed in between, improves the radiation performance [23]. With this configuration, a gain of 7.8 dB with a fractional bandwidth of 0.6 % were achieved. While the previous designs utilized PEC for low profile applications, a directivity higher than 9 dB was not attained. Furthermore, all the proposed low profile designs with PEC ground planes have a very narrow fractional bandwidth due to the high Q. A question arises: is it possible to design a low profile antenna with a HIS ground plane which has a directivity that is comparable to or greater than a similar antenna on a PEC ground plane without degrading the total radiation efficiency and the fractional bandwidth? This dissertation addresses this question and offers solution.

The small spacing between the radiating elements and ground planes involves the excitation of surface waves. Surface waves have always been considered undesired, and several designs were proposed to suppress their propagation [24], [25]. Nevertheless, these surface waves can be exploited to introduce extra resonances to broaden the

fractional bandwidth. A dipole positioned above a metasurface with square patches to launch surface waves resulted in a 6% fractional bandwidth with omnidirectional radiation [26]. In addition to surface wave resonances, a dipole resonance was also excited [27] leading to a wider bandwidth with broadside radiation. Besides radiating elements above metasurfaces, a center-fed circular patch was placed below square-patch metasurfaces, yielding an omnidirectional radiation with a matching bandwidth of 5.6% [28]. The reported matching bandwidth, as will be proposed in this dissertation, can be further broaden by controlling individually the excited surface waves along the principal planes.

1.2 Scope of the Work

A reduced overall antenna height is a favorable feature for most modern low-profile communication applications. In Chapter 2, PEC and PMC ground planes are investigated for low-profile electric and magnetic radiating elements. Furthermore, far-field analytical expressions are derived, and the results are compared with full-wave EM simulations performed with HFSS. This study is focused on highlighting the effect of different ground planes on directivity. An analytical formulation with physical interpretation is provided as to why PEC ground planes provide higher directivity than PMC when the spacing/height between the radiating elements and the ground planes is less than 0.25λ. The analytical formulation and physical interpretation are based on image theory.

The limitation that PEC and PMC ground planes possess can be overcome by some engineered surfaces, namely corrugated PECs, coated PECs, corrugated coating covered PECs, and HISs. In Chapter 3, these engineered surfaces are introduced. The reflection phase for all aforementioned methods is analytically obtained and compared with HFSS.

In addition to the analysis of the reflection phase, Chapter 4 discusses the dispersion behavior for different engineered structures. Analytical models for the dispersion diagrams are derived, which can be used to analyze the behavior of the surface waves. The results of the analytical expressions are compared with simulation. Furthermore, a simple approach of extracting possible surface wave resonances utilizing the dispersion diagram is outlined. To validate the approach, the extracted resonances are compared with the cavity model resonance.

Based on the analytical formulation, a circular loop loaded with a circular HIS is presented in Chapter 5. Since a curvilinear radiating element (circular loop antenna) is utilized, a circular HIS is considered and printed on a circular ground plane. To advance the directivity, a dual circular HIS is deployed forming a hybrid ground plane. Integrating the loop element with the hybrid ground plane enhances the directivity up to 10.5 dB with a 13% fractional bandwidth. The design is analyzed using the reflection phase and the dispersion behaviors; both analyses agree with the simulated results. Along with the obtained simulation results, a prototype was fabricated and measured. A good agreement between simulations and measurements were observed; Journal article [29] "Hybrid Circular Ground Planes for High-Realized-Gain Low-Profile Loop Antennas" is a by-product of this effort.

The fractional bandwidth and the broadside directivity are further enhanced, as discussed in Chapter 6, exploiting the introduction of a square ring element in the vicinity of a metasurface with rectangular-patches. The advantage of utilizing rectangular HIS is that it gives individual control over the excited surface waves along the principal planes. To excite the surface waves, various configurations have been considered; namely, square-ring element above, below, and within the metasurface. The latter design, with a $0.07\lambda_o$ height-profile, provides superior matching and gain performances compared to the others. It operates from 3.8 to 5 GHz (27% fractional

bandwidth) with a stable realized gain up to 11.9 dBi in the broadside direction. A prototype of the structure, with a simple probe feeding mechanism, was fabricated and measured. An excellent agreement was attained between the simulated and measured data. Journal article [30] "Performance Enhancement of Square-Ring Antennas Exploiting Surface-Wave Metasurfaces" is based on this technology.

The square ring element embedded within HIS is introduced in Chapter 7 to further enhance the directivity by forming different array arrangements. Four square ring elements are embedded within metasurface to launch surface waves and form a planar metasurface antenna array. The incorporation of the metasurface enhances impedance matching and gain compared to a conventional square ring array. Two array designs are considered for different polarizations. The first design investigates the performance of 1x4 array of ring elements when placed within periodic patches. With a spacing of $0.56\lambda_o$ between the ring elements, a peak gain of 15.8 dBi with an aperture efficiency of 83% are attained. Unlike the 1x4 linearly polarized structure, the second design consists of an array of 2x2 ring elements for circular polarization. A similar peak gain is realized with a better port isolation compared to the linearly polarized design. Due to the similarity of the two designs, only the 2x2 array is experimentally validated; good agreements are observed between the simulated and measured data. Journal article [31] "Metasurfaces for Reconfiguration of Multi-Polarization Antenna and Van Atta Reflector Arrays" is partially based on this technology.

Chapter 2

PERFORMANCE OF THE RADIATING ELEMENT ABOVE PEC AND PMC GROUND PLANES

Placing an electric or magnetic radiating element on top of a ground plane has significant impact on the performance of the radiating element. As the distance between the ground plane and the radiating element approaches zero, mutual coupling between the radiating element and the ground plane becomes pronounced. Furthermore, the fields generated by the radiating element will be reflected by the ground plane and cause constructive and destructive interferences. The magnitude and the phase of the reflected waves depend on the geometry and the material properties of the ground plane [32]. As a consequence, the overall radiation performance of the antenna will be impacted. In this section, the directivity of electric and magnetic radiating elements is investigated when they placed above PEC and PMC ground planes. An analytical far-field model will be derived and validated by the finite element method using HFSS.

The term *low profile* usually refers to an antenna whose overall height is less than one tenth of the operating frequency [33]. To meet the overall height, only horizontal electric and magnetic dipoles will be considered as the radiating elements. The horizontal electric and magnetic dipoles will be placed above PEC and then PMC ground planes, and the far-field model will be derived for all four configurations. The four configurations are:

- Electric dipole above PEC ground plane.
- Electric dipole above PMC ground plane.

- Magnetic dipole above PEC ground plane.
- Magnetic dipole above PMC ground plane.

2.1 Electric Radiating Element

The configurations of an electric dipole positioned above PEC and PMC ground planes are shown in Fig. 2.1. Although PMCs do not exist in nature, the configuration is considered for comparison purposes.

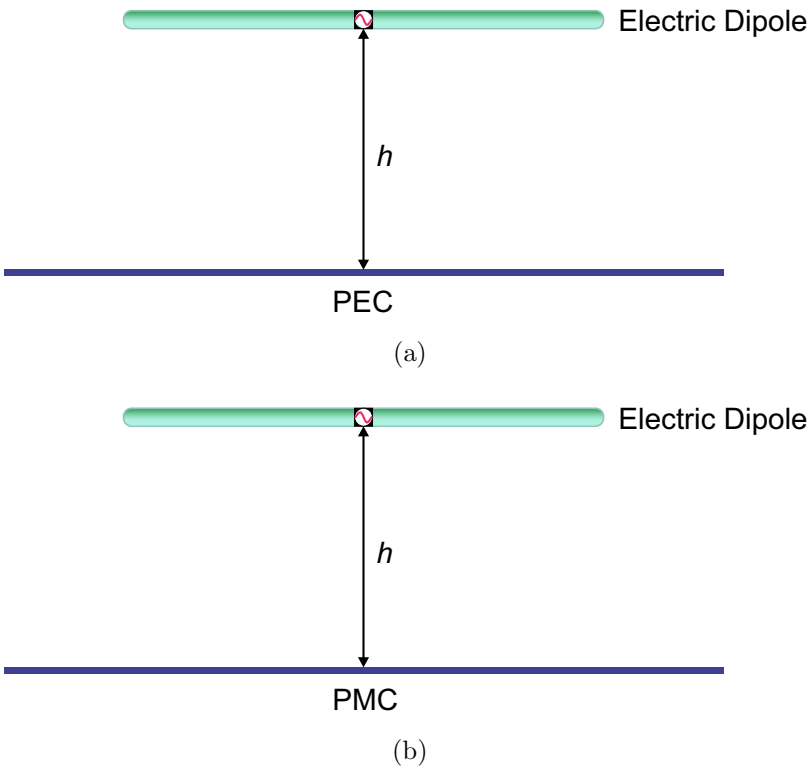

Figure 2.1: (a) Electric Dipole Above PEC. (b) Electric Dipole Above PMC.

2.1.1 PEC Ground Plane

When a radiating element is placed above a ground plane, reflections are introduced. To account for the reflections, image theory can be used. When an electric

dipole is positioned horizontally at a distance above a PEC, an image can be introduced that is 180 degree out of phase with the actual electric dipole, as shown in Fig. 2.2. In other words, the PEC will reflect the fields radiated by the element and directed toward the ground plane with a reflection coefficient of a unity magnitude and a phase of 180 degrees. From Fig. 2.2, the far-zone radiated electric field for a

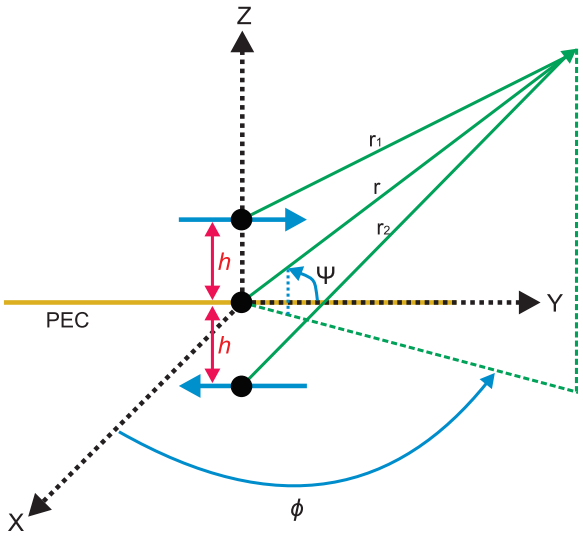

Figure 2.2: Horizontal Electric Dipole Above PEC Ground Plane.

horizontal dipole is represented by [32]

$$E_{\psi}^{d} = j\eta \frac{kI_o l e^{-jkr_1}}{4\pi r_1} \sin\psi \tag{2.1}$$

and the reflected field by the PEC ground plane is expressed as [32]

$$E_{\psi}^{r} = -j\eta \frac{kI_o l e^{-jkr_2}}{4\pi r_2} \sin\psi \tag{2.2}$$

The total radiated field valid on and above the ground plane is represented by

$$E_{\psi} = E_{\psi}^{d} + E_{\psi}^{r} \quad = \quad j\eta \frac{kI_o l\, e^{-jkr}}{4\pi r} \sqrt{1 - \sin^2\theta\, \sin^2\phi}\, [2\, j\, \sin(k\, h\, \cos\theta)] \tag{2.3}$$

Once the total radiated field is found, the radiated power and radiation intensity can be derived as follows [32]

$$\begin{aligned} P_{rad} &= \frac{1}{2\,\eta}\int_0^{2\pi}\int_0^{\pi/2} |E_\psi|^2 \cdot r^2 \sin\theta\, d\theta\, d\phi \\ &= \eta\frac{\pi}{2}\left(\frac{I_o\, l}{\lambda}\right)^2 \left[\frac{2}{3} - \frac{\cos(2\,k\,h)}{(2\,k\,h)^2} - \frac{\sin(2\,k\,h)}{2\,k\,h} + \frac{\sin(2\,k\,h)}{(2\,k\,h)^3}\right] \end{aligned} \tag{2.4}$$

$$\begin{aligned} U &\simeq \frac{r^2}{2\,\eta}\,|E_\psi|^2 \\ &= \frac{\eta}{2}\left(\frac{I_o\, l}{\lambda}\right)^2 (1 - \sin^2\theta\, \sin^2\phi)\, \left[\sin^2(k\,h\,\cos\theta)\right] \end{aligned} \tag{2.5}$$

The maximum radiation intensity when $h \leq 0.25\lambda$ occurs along the broadside ($\theta = 0$)

$$U_{max} = \frac{\eta}{2}\left(\frac{I_o\, l}{\lambda}\right)^2 \left(\sin^2(k\,h)\right) \tag{2.6}$$

Using the radiated power and the maximum radiation intensity, the maximum directivity (when $h \leq 0.25\lambda$) can be expressed as [32]

$$\begin{aligned} D_o &= \frac{4\,\pi\, U_{max}}{P_{rad}} \\ &= \frac{4\,\sin^2(k\,h)}{\left[\frac{2}{3} - \frac{\cos(2\,k\,h)}{(2\,k\,h)^2} - \frac{\sin(2\,k\,h)}{2\,k\,h} + \frac{\sin(2\,k\,h)}{(2\,k\,h)^3}\right]} \end{aligned} \tag{2.7}$$

To validate the expression for the directivity, a horizontal dipole above an infinite PEC is modeled using full-wave simulation (HFSS) and the directivity in the broadside direction is plotted as a function of height h between the dipole and the PEC ground plane. The dipole is 0.45λ long and the distance h is varied from 0 to 0.5λ, where λ is the wavelength at 3 GHz. As shown in Fig. 2.3, the directivity obtained by HFSS and (2.7) are in a good agreement.

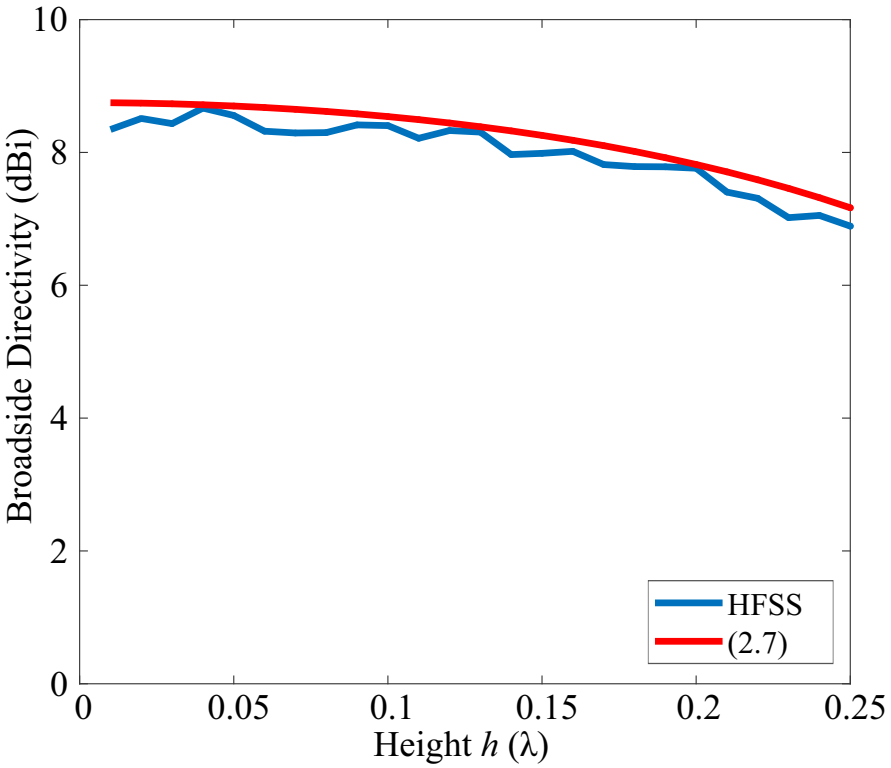

Figure 2.3: Comparison Between the Directivity of a Horizontal Electric Dipole at a Height h Above a PEC Ground Plane Obtained Using HFSS and the Derived Analytical Expression of (2.7).

2.1.2 PMC Ground Plane

According to image theory, placing an electric horizontal radiating element above a PMC ground plane produces constructive interference and the image reinforces the radiation, as shown in Fig 2.4. As a result, the radiated and reflected fields are in phase and can be written as shown [32]

$$E_{\psi}^{d} = j\eta \frac{kI_o l\, e^{-jkr_1}}{4\pi r_1} \sin\psi \tag{2.8}$$

$$E_{\psi}^{r} = j\eta \frac{kI_o l e^{-jkr_2}}{4\pi r_2} \sin\psi \tag{2.9}$$

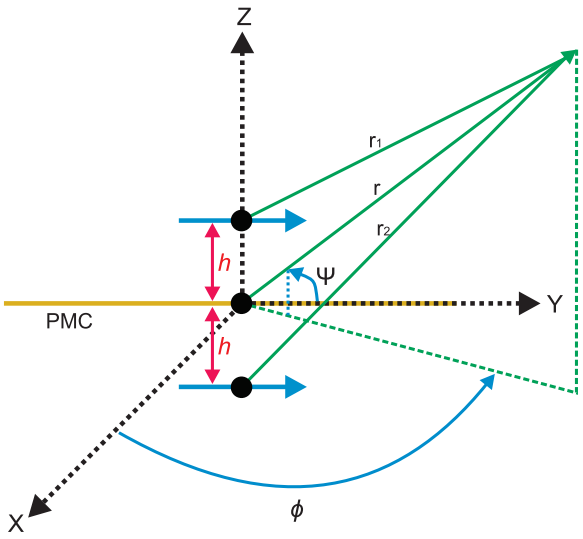

Figure 2.4: Horizontal Electric Dipole Above PMC Ground Plane.

Thus, the total radiated field can be expressed as

$$E_{\psi} = j\eta \frac{k I_o l \, e^{-jkr}}{2\pi r} \sqrt{1 - \sin^2\theta \, \sin^2\phi} \, [\cos(k\,h\,\cos\theta)] \tag{2.10}$$

Similar to the above steps for the electrical dipole above a PEC, the respective radiated power and radiation intensity can be written, respectively, as

$$P_{rad} = \eta \frac{\pi}{2} \left(\frac{I_o\, l}{\lambda}\right)^2 \left[\frac{2}{3} + \frac{\cos(2\,k\,h)}{(2\,k\,h)^2} + \frac{\sin(2\,k\,h)}{2\,k\,h} - \frac{\sin(2\,k\,h)}{(2\,k\,h)^3}\right] \tag{2.11}$$

$$U = \frac{\eta}{2} \left(\frac{I_o\, l}{\lambda}\right)^2 \left[(1 - \sin^2\theta \, \sin^2\phi) \, \left(\cos^2(k\,h\,\cos\theta)\right)\right] \tag{2.12}$$

$$U_{max} = \frac{\eta}{2} \left(\frac{I_o\, l}{\lambda}\right)^2 \left[\cos^2(k\,h)\right] \qquad \text{For } (h \leq 0.25\lambda) \tag{2.13}$$

Based on its definition of (2.7), the maximum directivity (when $h \leq 0.25\lambda$) can be expressed as

$$D_o = \frac{4\,\cos^2(k\,h)}{\left[\frac{2}{3} + \frac{\cos(2\,k\,h)}{(2\,k\,h)^2} + \frac{\sin(2\,k\,h)}{2\,k\,h} - \frac{\sin(2\,k\,h)}{(2\,k\,h)^3}\right]} \tag{2.14}$$

The validation of (2.14) for a horizontal electric dipole above a PMC is similar to the one above PEC except that the boundary conditions for the ground plane are changed

to PMC. The directivity in the broadside direction (θ) is obtained and plotted. The results of the directivity obtained by (2.14) and the full-wave simulation (HFSS) are plotted in Fig. 2.5, and they are in a good agreement.

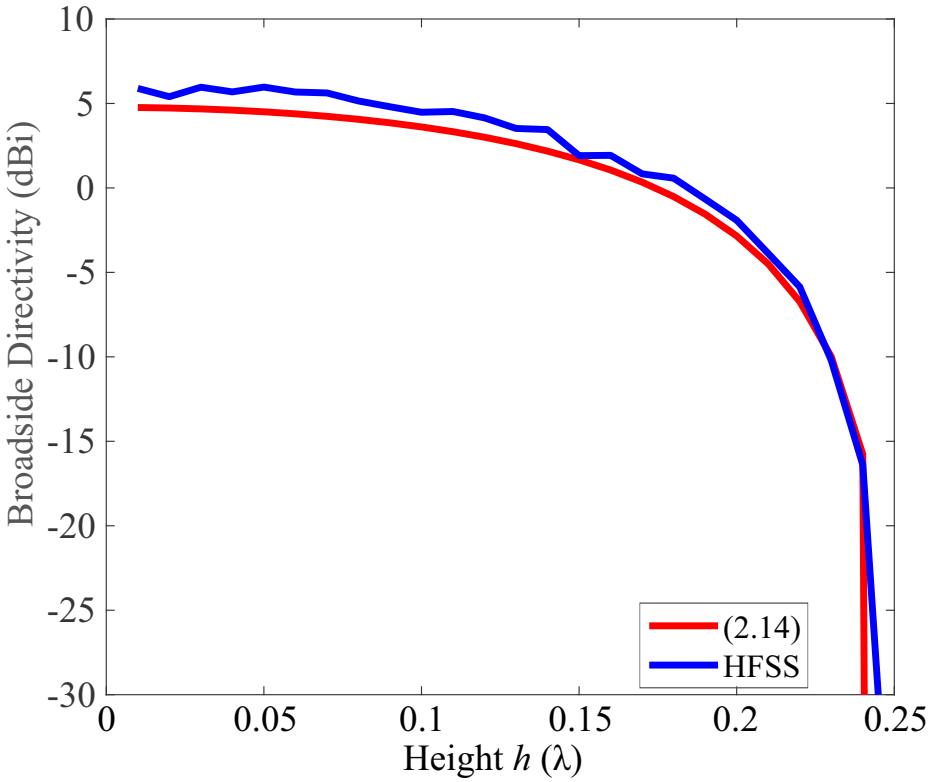

Figure 2.5: Comparison Between the Directivity of a Horizontal Electric Dipole at a Height h Above a PMC Ground Plane Obtained Using HFSS and the Derived Analytical Expression of (2.14).

From Fig. 2.3 and 2.5, the directivity of electric dipole positioned horizontally at small distance ($<0.25\lambda$) above a PEC is larger than that of the dipole when placed above a PMC. Thus, the PEC is a better choice for a ground plane when a higher directivity is desired. However, since the radiated field and reflected field are out of phase in the PEC case, the radiation efficiency and the reflection loss are very significant as h approaches zero [21]. In contrast, the PMC ground plane provides a

better radiation efficiency with smaller directivity as h approaches zero. Since PMCs do not exist in nature, HISs are used to mimic PMCs and to obtain good radiation. An analogy that can be used to visualize the behavior of the electric dipole above a PEC ground plane is when a laser is attached to a lossy narrow beam lens, where the laser represents the dipole and the narrow beam lens resembles the PEC. The integration of the laser and the lens gives a narrow beam (high directivity); however, no beam comes out of the lens due to the presence of loss in the lens as shown in Fig. 2.6. In Chapter 5, we will show how the proposed ground plane will achieve a high directivity comparable to a PEC ground plane.

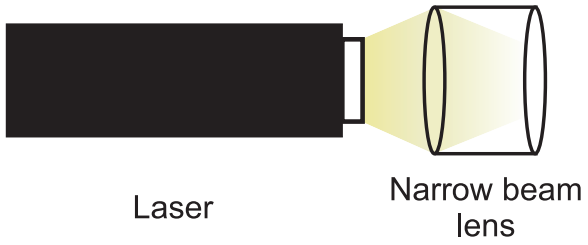

Figure 2.6: The Analogy of Laser and a Narrow Beam Lens Integration for Higher Directivity.

2.2 Magnetic Radiating Element

The configuration of a horizontal magnetic dipole above PMC and PEC is shown in Fig. 2.7. In this section, the magnetic dipole will be analyzed when positioned above PMC and PEC ground planes.

2.2.1 PMC Ground Plane

Based on image theory, the image of a magnetic dipole placed horizontally above a PMC ground plane is 180^o out of phase of the actual magnetic dipole (Fig. 2.8). As a consequence, as h decreases, the magnetic radiating element will possess poor radi-

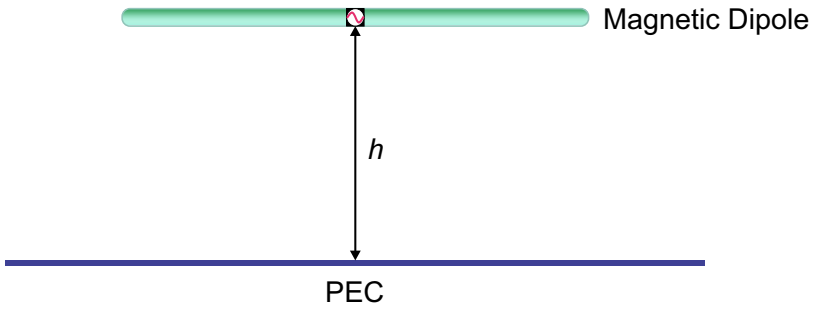

(a)

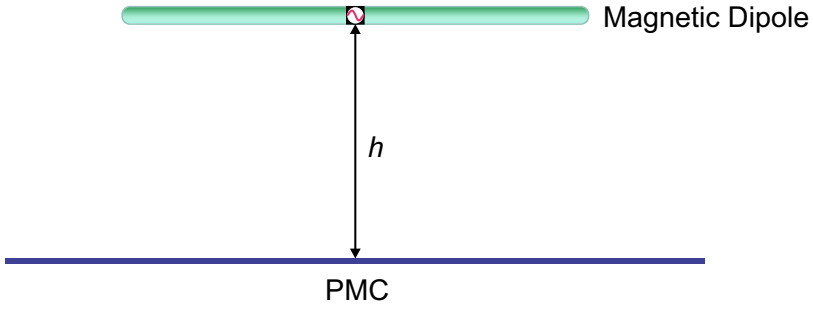

(b)

Figure 2.7: (a) Horizontal Magnetic Dipole Above PEC. (b) Horizontal Magnetic Dipole Above PMC.

ation efficiency and a high mismatch loss. The far-field model for a magnetic dipole above a PMC is derived based on the configurations shown in Fig. 2.7. Following the same steps as for the electric radiating element, the far-zone electric field components for a magnetic dipole above a PMC can be written as

$$E^d = (\hat{\boldsymbol{a}}_\phi \cos\theta \sin\phi - \hat{\boldsymbol{a}}_\theta \cos\phi) j \frac{k\, I_m\, l}{4\pi r}\, e^{-jkr} \tag{2.15}$$

$$E^r = (-\hat{\boldsymbol{a}}_\phi \cos\theta \sin\phi + \hat{\boldsymbol{a}}_\theta \cos\phi) j \frac{k\, I_m\, l}{4\pi r}\, e^{-jkr} \tag{2.16}$$

and the total radiated field is expressed as

$$E = (\hat{\boldsymbol{a}}_\phi \cos\theta \sin\phi - \hat{\boldsymbol{a}}_\theta \cos\phi) j \frac{k\, I_m\, l}{4\pi r}\, e^{-jkr} [2j \sin(kh\cos\theta)] \tag{2.17}$$

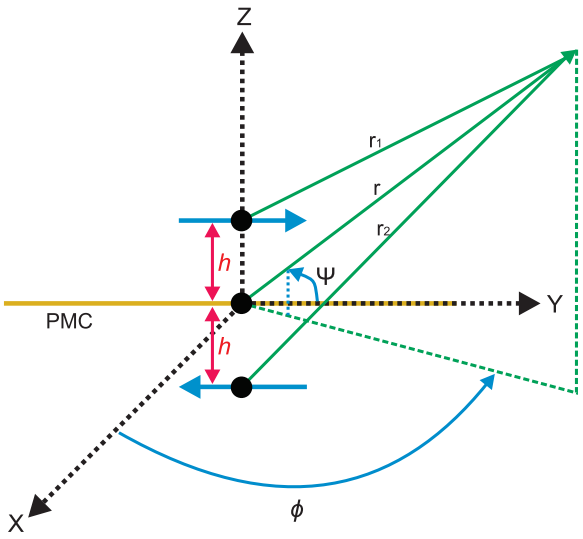

Figure 2.8: Horizontal Magnetic Dipole Above PMC Ground Plane.

Using (2.17), the radiated power and the radiation intensity can be written, respectively, as

$$P_{rad} = \frac{k^2\, I_m^2\, l^2}{8\eta\pi}\left(\frac{2}{3} - \frac{\cos(2\,k\,h)}{(2\,k\,h)^2} - \frac{\sin(2\,k\,h)}{2\,k\,h} + \frac{\sin(2\,k\,h)}{(2\,k\,h)^3}\right) \tag{2.18}$$

$$U = \frac{k^2\, I_m^2\, l^2}{8\eta\pi^2}(1 - \sin^2\theta\, \sin^2\phi)(\sin^2(kh\cos\theta)) \tag{2.19}$$

From (2.19), the maximum radiation (when $h \leq 0.25\lambda$) occurs at θ=0. Thus, the maximum radiation intensity can be written as

$$U_{max} = \frac{k^2\, I_m^2\, l^2}{8\eta\pi^2}[\sin^2(kh)] \tag{2.20}$$

By using (2.18) and (2.20), the maximum directivity, when $h \leq 0.25\lambda$, can be expressed as

$$D_o = \frac{4\,\sin^2(k\,h)}{\left[\frac{2}{3} - \frac{\cos(2\,k\,h)}{(2\,k\,h)^2} - \frac{\sin(2\,k\,h)}{2\,k\,h} + \frac{\sin(2\,k\,h)}{(2\,k\,h)^3}\right]} \tag{2.21}$$

To confirm (2.21), a simulation is performed using HFSS. However, in order to simulate a magnetic dipole in HFSS, the magnetic dipole has to be excited with magnetic

current. To the author's knowledge, there is no possible way to excite magnetic current in HFSS. Therefore, an infinitesimal electrical horizontal loop was simulated instead as, according to duality theorem, it is equivalent to an infinitesimal horizontal magnetic dipole [34]. The simulation was modeled as shown in Fig. 2.9. The directivity at $\theta = 0$ is plotted in Fig. 2.10 using HFSS and compared with the directivity obtained using (2.21). Good agreement is indicated between the two set of data.

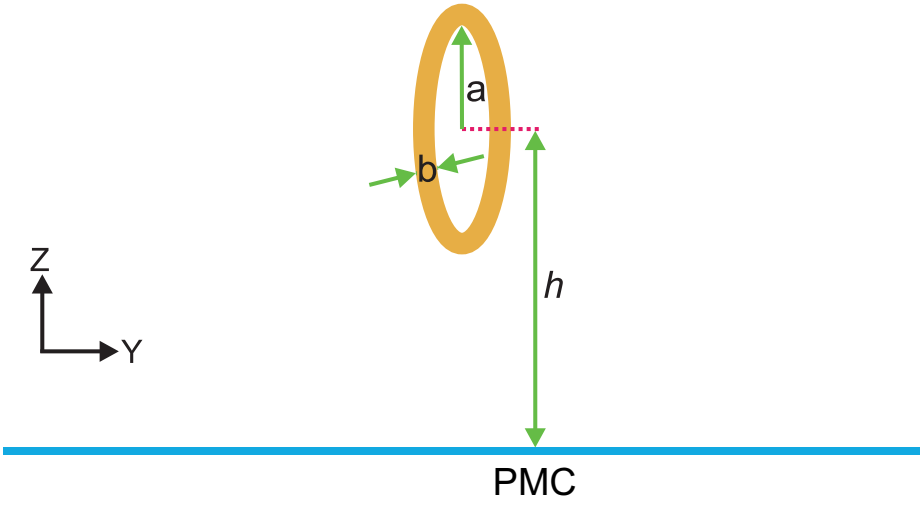

Figure 2.9: Equivalent Horizontal Magnetic Dipole Above a PMC Ground Plane.

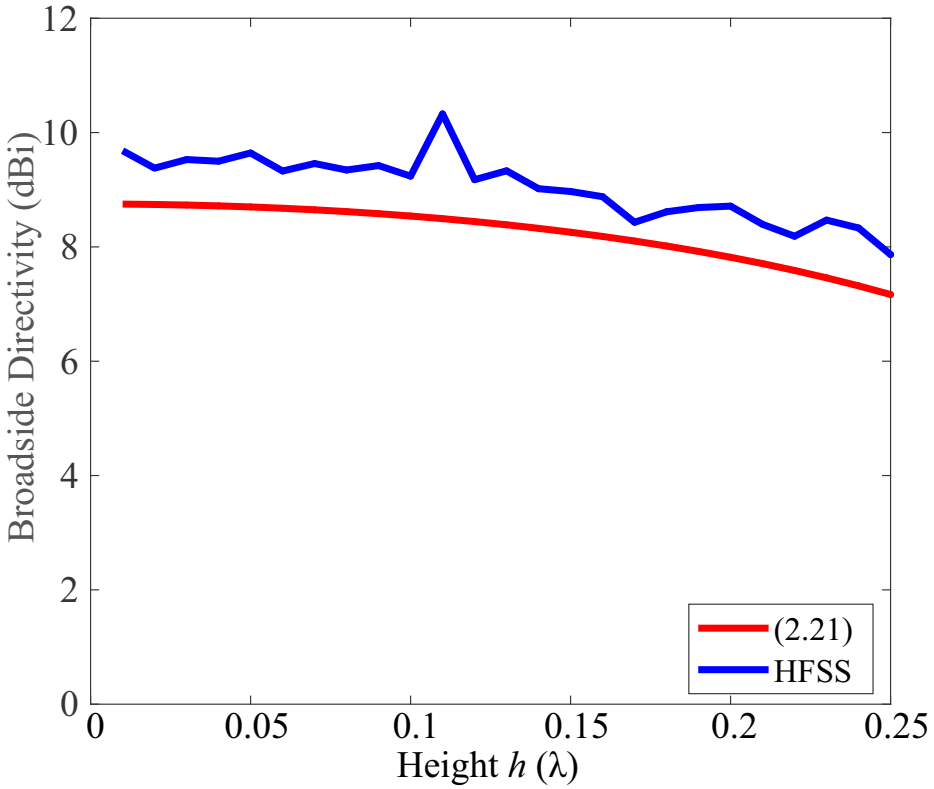

Figure 2.10: Comparison Between Directivity of a Horizontal Magnetic Dipole at a Height h Above a PMC Ground Plane Obtained Using HFSS and the Derived Analytical Expression of (2.21).

2.2.2 PEC Ground Plane

When a magnetic dipole is placed parallel to a PEC ground plane, the image is in-phase with the actual radiating element. Thus, the PEC in this configuration possesses a reflection coefficient with unity magnitude and a phase of zero, as shown in Fig. 2.11. The radiated and reflected fields can be written, respectively, as

$$E^d = j\frac{k\,I_m\,l}{4\pi r}\,\left(-\hat{\boldsymbol{a}}_\theta\cos\phi + \hat{\boldsymbol{a}}_\phi\cos\theta sin\phi\right)e^{-jkr} \tag{2.22}$$

$$E^r = j\frac{k\,I_m\,l}{4\pi r}\,\left(-\hat{\boldsymbol{a}}_\theta\cos\phi + \hat{\boldsymbol{a}}_\phi\cos\theta sin\phi\right)e^{-jkr} \tag{2.23}$$

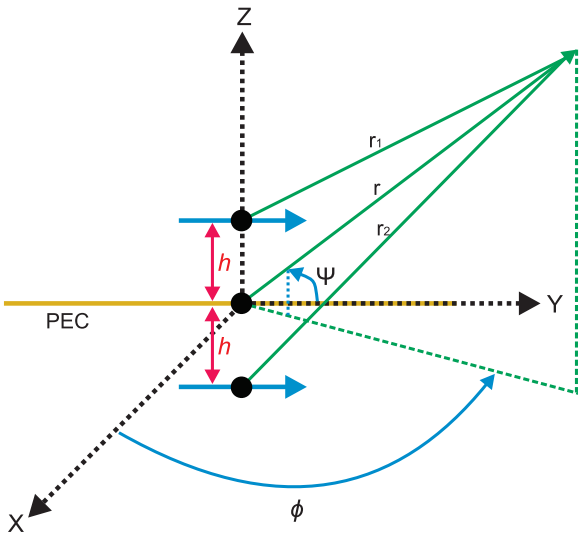

Figure 2.11: Horizontal Magnetic Dipole Above PEC Ground Plane.

while the total radiated field is expressed as

$$E_\theta = -j\frac{k\,I_m\,l}{4\pi\,r}\cos\phi\,e^{-jkr}[2\cos(kh\cos\theta)] \tag{2.24}$$

Using (2.24), the radiated power and radiation intensity can be written as

$$P_{rad} = \frac{k^2\,I_m^2\,l^2}{8\eta\pi}\left(\frac{2}{3} + \frac{\cos(2\,k\,h)}{(2\,k\,h)^2} + \frac{\sin(2\,k\,h)}{2\,k\,h} - \frac{\sin(2\,k\,h)}{(2\,k\,h)^3}\right) \tag{2.25}$$

$$U = \frac{k^2\,I_m^2\,l^2}{8\eta\pi^2}\left(1 - \sin^2\theta\,\sin^2\phi\right)[\cos^2(kh\cos\theta)] \tag{2.26}$$

The maximum radiation intensity occurs along $\theta = 0$ and can be reduced to

$$U_{max} = \frac{k^2\,I_m^2\,l^2}{8\eta\pi^2}[\cos^2(kh)] \tag{2.27}$$

From (2.25), (2.27), and the definition of (2.7), the maximum directivity can be expressed as

$$D_o = \frac{4\,\cos^2(k\,h)}{\left[\frac{2}{3} + \frac{\cos(2\,k\,h)}{(2\,k\,h)^2} + \frac{\sin(2\,k\,h)}{2\,k\,h} - \frac{\sin(2\,k\,h)}{(2\,k\,h)^3}\right]} \tag{2.28}$$

To validate the directivity of (2.28), a full-wave simulation, similar to the model shown in Fig. 2.9 with a PEC boundary condition assigned to the ground plane, was performed using HFSS. The directivity in the broadside direction ($\theta = 0$) was obtained and plotted in Fig. 2.12; a good agreement is indicated between the full-wave simulation and the derived analytical expression of (2.28).

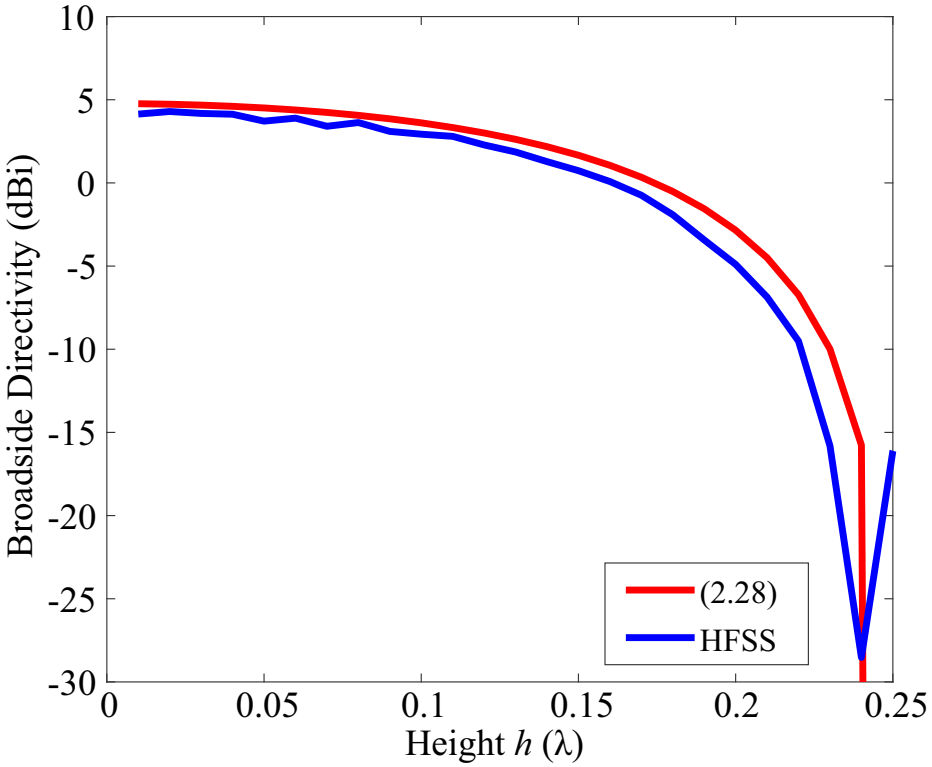

Figure 2.12: Comparison Between the Directivity of a Horizontal Magnetic Dipole at a Height h Above a PEC Ground Plane Obtained Using HFSS and the Derived Analytical Expression of (2.28).

From Fig. 2.10 and Fig. 2.12, it can be concluded that a horizontal magnetic dipole above a PMC ground plane produces a higher directivity than a PEC ground plane (when $h \leq 0.25\lambda$). Nevertheless, the total radiation efficiency is low in the PMC case, and it gets worse as h approaches zero since the image is out of phase with the actual magnetic dipole.

2.3 Physical Explanation

The higher directivity observed for a horizontal electrical dipole above a PEC and for a horizontal magnetic dipole above a PMC can be explained by investigating the field distribution over the ground planes. This concept is similar to an aperture antenna, where the maximum directivity is given by [32]

$$D_o = \epsilon_{ap} A_p \left(\frac{4\pi}{\lambda^2} \right) \tag{2.29}$$

where ϵ_{ap} is the aperture efficiency, and A_p is the physical area of the aperture. For a rectangular aperture, which represents the PEC and PMC ground planes, the A_p is equal to the area of the ground planes. The aperture efficiency depends on the field distribution over the aperture. When the field distribution is uniform (Fig. 2.13a), the aperture efficiency is unity and the highest directivity is achieved. However, the aperture efficiency decreases when the field is non-uniformly distributed over the aperture. For instance, when the TE_{10}-mode distribution is excited over the aperture, as shown in Fig. 2.13b, the aperture efficiency is reduced to 0.81 and a lower directivity is obtained [32].

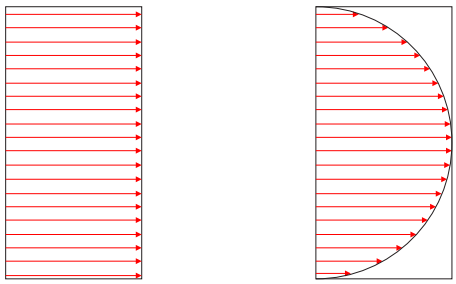

(a) (b)

Figure 2.13: Field Distribution (a) Uniform Distribution. (b) TE_{10}-mode Distribution.

By applying the aperture concept to the PEC and PMC ground planes, a uniform field distribution over the ground plane is observed when:

1) a horizontal electrical dipole positioned above a PEC,

2) a magnetic horizontal dipole positioned above a PMC.

These are illustrated in Figs. 2.14a and 2.15a, respectively. Thus, a higher directivity should be expected since the aperture efficiency is almost unity. As the field is non-uniformly distributed over the ground plane (Figs. 2.14b and 2.15b), the aperture efficiency is reduced, which leads to a lower directivity.

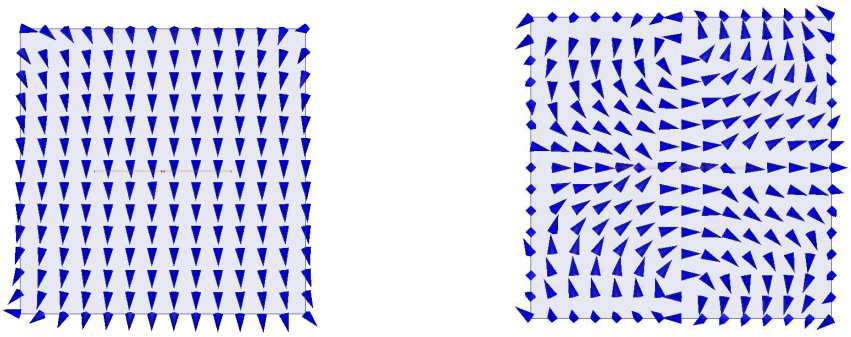

(a) (b)

Figure 2.14: Field Distribution for an Electrical Dipole Above (a) PEC. (b) PMC.

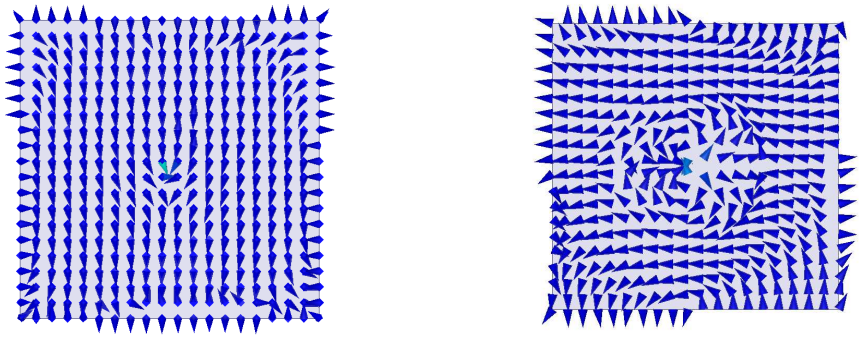

(a) (b)

Figure 2.15: Field Distribution for a Magnetic Dipole Above (a) PMC. (b) PEC.

Chapter 3

REFLECTION BEHAVIOR OF ENGINEERED SURFACES

The previous chapter discussed the radiation performance of a radiating element when positioned near PEC and PMC ground planes. The fixed reflection phases that PEC and PMC possess inspire researchers to explore the possibility of altering the inherent reflection behavior of these surface. The advantages of changing the reflection phase of a surface are, to name a few, controlling the scattered field, enabling radiating elements to be positioned very close to the surface, and modifying surface wave propagation [7]. Various methods of altering the reflection behavior have been investigated, and they will be discussed in this chapter.

3.1 Corrugated PEC Plate

A classical approach to modify the reflection behavior of a PEC plate is realized by changing the geometry of the structure. This can be attained by implementing corrugations on the surface [6]. A corrugated surface is realized by creating ridges (corrugations) of width w, thickness t, and depth d, as shown in Fig. 3.1. The modified surface possesses a high impedance when the polarization of the electric field is perpendicular to the corrugation, and a low impedance when the electric field is parallel to the grooves [6].

The surface impedance when the electric field is perpendicular to the corrugation can be approximated by using the impedance of a shorted transmission line [6].

$$Z_{corg} = \eta_o \left(\frac{w}{p}\right) \tan\left(\beta_o d\right) \tag{3.1}$$

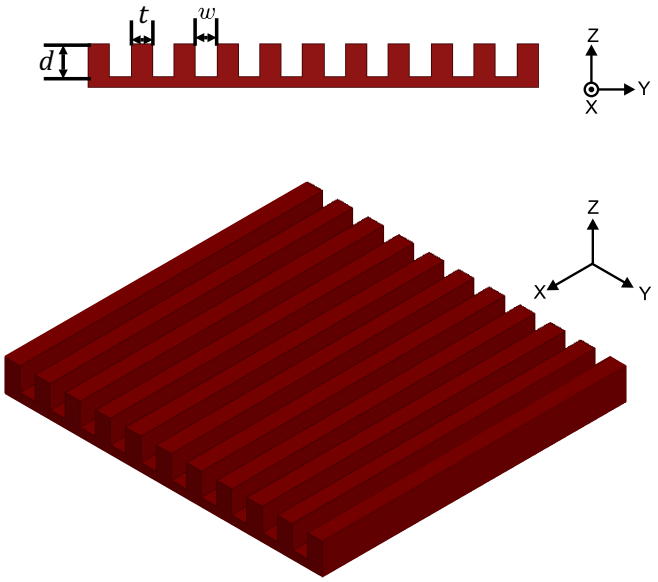

Figure 3.1: Geometry of a Corrugated Surface.

where w is the width of the ridges, p is the periodicity of the groove or $(p = t+w)$, and d is the depth of the groove. This equation gives excellent approximation when the width of the groove is $(w \leq \lambda/10)$, and the the thickness of teeth is $(t \leq \lambda/100)$ [6]. By using (3.1), the reflection coefficient can be calculated by

$$\Gamma = \frac{Z_{corg} - Z_o}{Z_{corg} + Z_o} \tag{3.2}$$

where $(Z_o = 120\pi)$ is the free-space impedance.

On the other hand, when the electric field is parallel to the grooves, the surface impedance is very low (near zero), similar to a PEC sheet. Therefore, the reflection phase for parallel polarization is about 180°.

To demonstrate the validity of (3.2), the reflection phase of different corrugated PEC is simulated utilizing full-wave simulation (HFSS), and the results are compared to those obtained with (3.2). For the full-wave simulation, a plane wave is illuminated normally to the surface with electric field polarized perpendicular to the corrugation. Floquet port is used to illuminate the corrugated PEC unit cell. Furthermore, the

corrugated PEC is simulated by modeling a single unit cell and applying the master and slave boundaries conditions, as demonstrated in Fig. 3.2. The linked boundary conditions, master and slave boundaries, are implemented on the walls to enforce the periodicity of the structure.

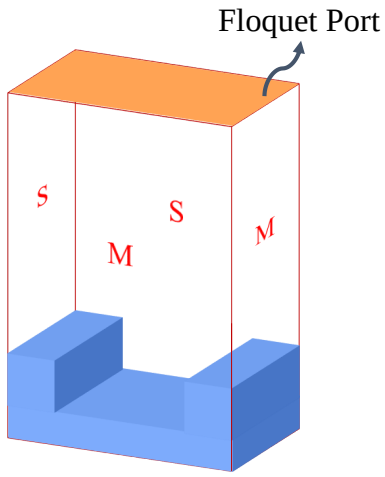

Figure 3.2: HFSS Simulation Setup for Corrugated PEC.

The reflection phases for different corrugated PEC dimensions are plotted in Fig. 3.3. As observed, the first case ($w = \lambda/10$, $d = \lambda/4$, and $t = \lambda/100$) and the second case ($w = \lambda/5$, $d = \lambda/4$, and $t = \lambda/20$) indicate an excellent agreement between the analytical and simulated results. However, when the thickness of the groove (t) gets larger than $\lambda/20$, as demonstrated for cases 3 and 4, the analytical results deviate from the simulated one.

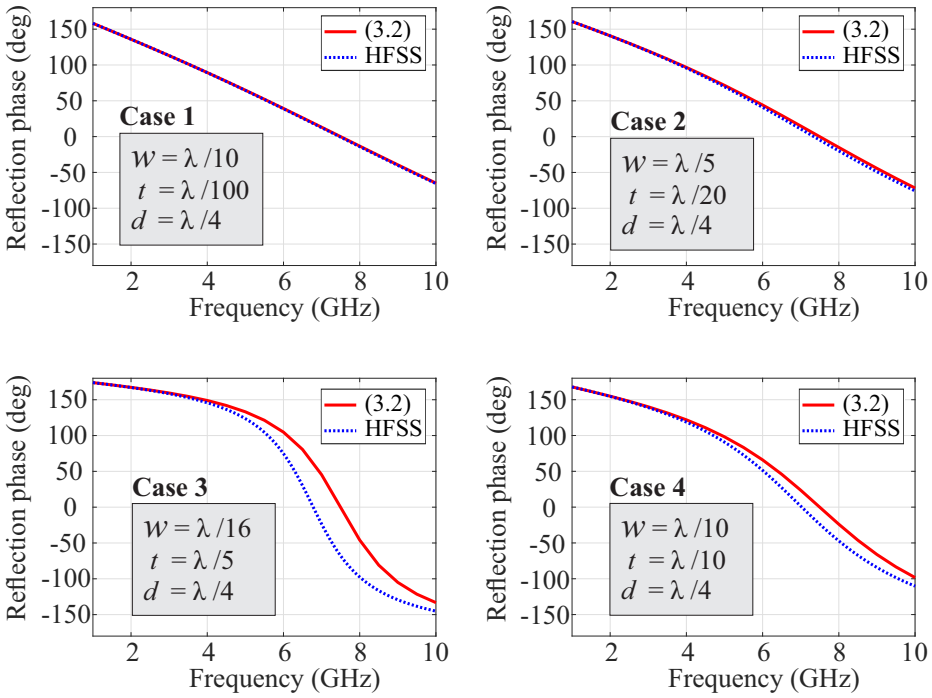

Figure 3.3: Reflection Phase Comparison for Different Corrugated PEC Dimensions.

3.2 Dielectric Covered PEC

An alternative approach to modify the reflection behavior of a PEC is to coat it with a dielectric material. The material composition and thickness of the dielectric can be adjusted to control the reflection phase. To develop an analytical model for calculating the reflection phase, we need to find the surface impedance at the top face ($\mathrm{Z} = -h^{+}$) of the grounded dielectric, as illustrated in Fig. 3.4. To simplify the analysis, the dielectric is considered to be infinite along the $x-$ and $y-$axes, while it is finite along the $z-$axis with a thickness of h. The surface impedance can be defined using a transmission line model [6]:

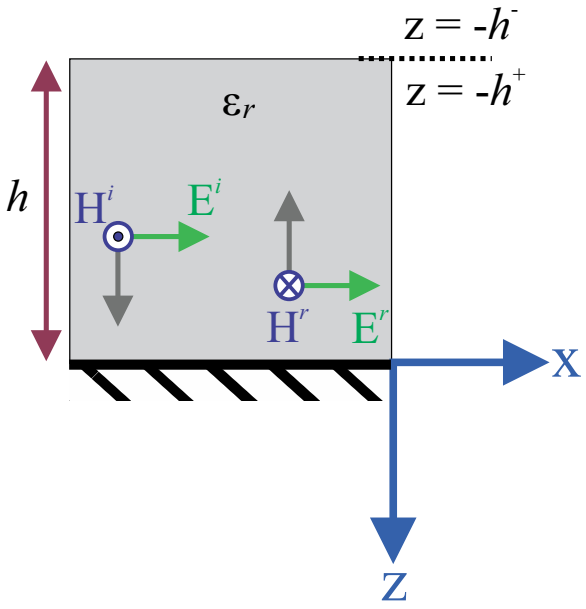

Figure 3.4: Grounded Dielectric Geometry.

$$\Gamma_{in}(\mathrm{z}=0) = -1 \tag{3.3}$$

$$\Gamma_{in}(\mathrm{z}=-h^{+}) = \left.\frac{E^r}{E^i}\right|_{\mathrm{z}=-h^{+}} = \left.\frac{\Gamma_{in}(\mathrm{z}=0)\,E_o e^{+j\beta z}}{E_o e^{-j\beta z}}\right|_{\mathrm{z}=-h^{+}} \tag{3.4}$$

$$= \Gamma_{in}(\mathrm{z}=0)\,e^{-j2\beta_d h} = -1\,e^{-j2\beta_d h}$$

$$Z_{in}(\mathrm{z}=-h^{+}) = \eta_d\,\frac{1+\Gamma_{in}(\mathrm{z}=-h^{+})}{1-\Gamma_{in}(\mathrm{z}=-h^{+})} = \eta_d\,\frac{1-e^{-j2\beta_d h}}{1+e^{-j2\beta_d h}} \tag{3.5}$$

$$\Gamma_{in}(\mathrm{z}=-h^{-}) = \frac{Z_{in}(\mathrm{z}=-h^{+})-\eta_o}{Z_{in}(\mathrm{z}=-h^{+})+\eta_o} \tag{3.6}$$

where $\left(\eta_d = \sqrt{\frac{\mu_o}{\varepsilon_o\varepsilon_r}}\right)$ is intrinsic impedance of the dielectric, β_d is the dielectric phase constant, and h is the thickness of the dielectric.

An alternative approach to determine the surface impedance at the top face of the grounded dielectric is by considering the impedance of a shorted transmission line [6]:

$$Z_{in}(\mathrm{Z}=-h^{+}) = j\left(\frac{\beta_d}{\omega\varepsilon_o\varepsilon_r}\right)\tan\left(\beta_d h\right) \tag{3.7}$$

Both equations (3.5) and (3.7) are identical, and they lead to the same results. To validate the accuracy of (3.6), different dielectric materials covering a PEC have been

simulated in HFSS (Fig. 3.5), and the reflection phases obtained analytically and numerically are plotted in Fig. 3.6. Similar to the corrugated PEC, master and slave boundary conditions are applied on the walls of the air box to enforce the infinity of the simulated unit cell. Furthermore, Floquet port is used to illuminate the unit cell; the port is deembedded to the top face of the dielectric to calculate the reflection phase at the dielectric-air interface. The thickness of the dielectric (h) is held constant, while the dielectric constant (ε_r) is varied for each case. For all considered cases, excellent agreement is observed between the simulated and calculated data.

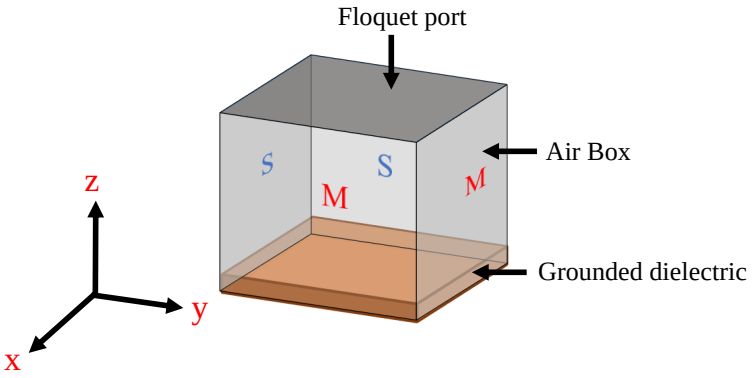

Figure 3.5: HFSS Setup to Calculate the Reflection Phase of a Grounded Dielectric.

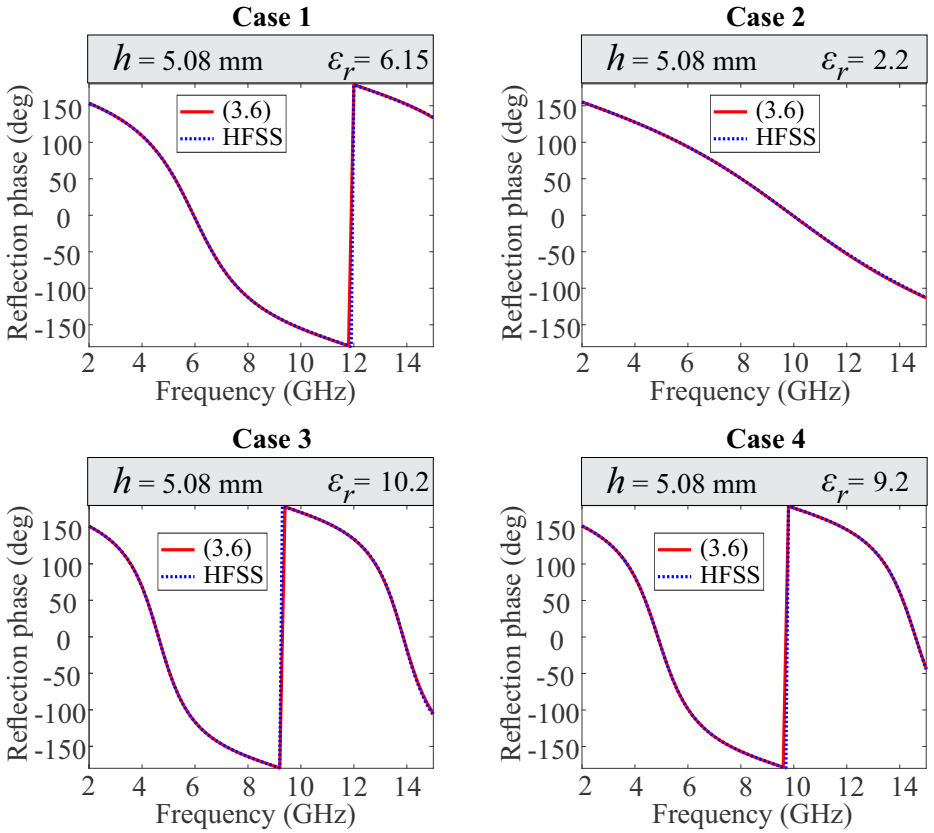

Figure 3.6: Reflection Phase Comparison for Different Dielectric Materials Covering a PEC Plate.

3.3 Mushroom-Like Surface

Another approach to alter the surface impedance is to use HIS surfaces, which are realized by placing metallic patches on a dielectric covered ground plane in a periodic arrangement. Although various shapes and geometries have been proposed, rectangular and circular patches geometries are examined in this chapter. Mushroom-like surfaces are two-dimensional surfaces where metallic patches are printed in a periodic arrangement on a grounded dielectric slab. The metallic patches are connected to the ground plane by vias. The structure shown in Fig. 3.7 consists of 7 by 7 unit cells. Each unit cell consists of a patch of width w, gap width g, and substrate thickness

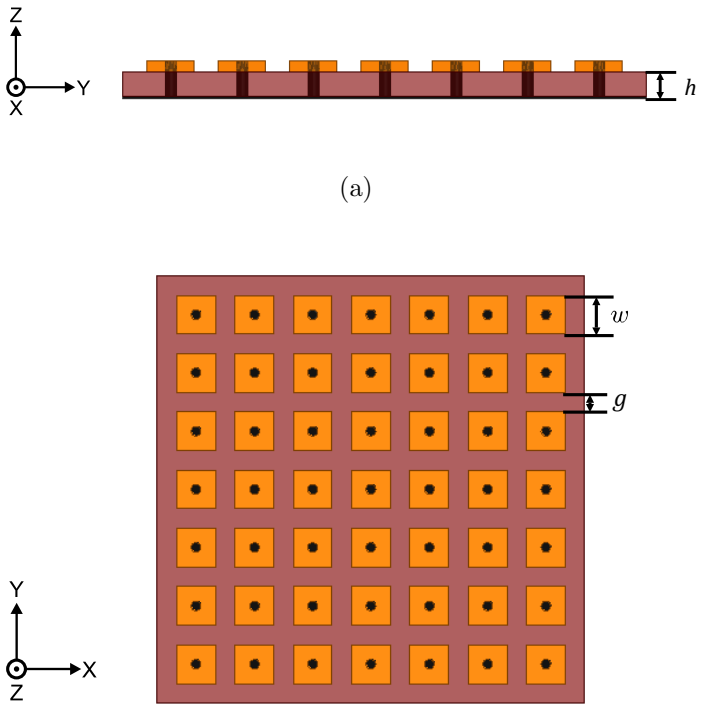

Figure 3.7: Geometry of a Mushroom-Like Surface (a) Side View. (b) Top View.

h. When the periodicity is less than a wavelength, the behavior of this structure can be represented by using an LC equivalent circuit. While the capacitance is primarily realized by the gap between two adjacent patches, the inductance is introduced by the current path that circulates between the patches through the vias. The capacitance and the inductance of a mushroom-like unit cell can be written as [1]

$$C = \frac{w\epsilon_o(1+\epsilon_r)}{\pi}\cosh^{-1}\left(\frac{w+g}{g}\right) \tag{3.8}$$

$$L = \mu h \tag{3.9}$$

Based on the equivalent parallel LC circuit, the surface impedance Z and the reflection phase of a mushroom unit cell can be expressed as

$$Z = \frac{j\omega L}{1 - \omega^2 LC} \tag{3.10}$$

$$\Gamma = \frac{Z - \eta_o}{Z + \eta_o} \tag{3.11}$$

The validity of the analytical model can be verified by comparing the results to those obtained with full-wave commercial software. The reflection phase of mushroom structures is verified by modeling a single unit cell of the structure (based on *the Floquet Theorem*), and establishing a FEM model. The mushroom unit cell is simulated in Ansys HFSS by applying the boundary conditions on the four sides of a rectangular waveguide to model an infinite surface, as shown in Fig. 3.8. To obtain the reflection

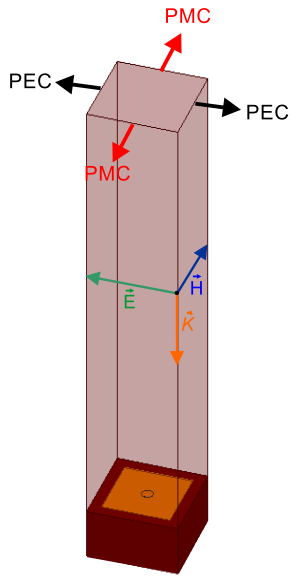

Figure 3.8: Appropriate Boundary Conditions for Simulating Unit Cells.

phase of the surface, plane waves at normal incidence are launched to illuminate the unit cell and the phase is plotted as shown in Fig. 3.9.

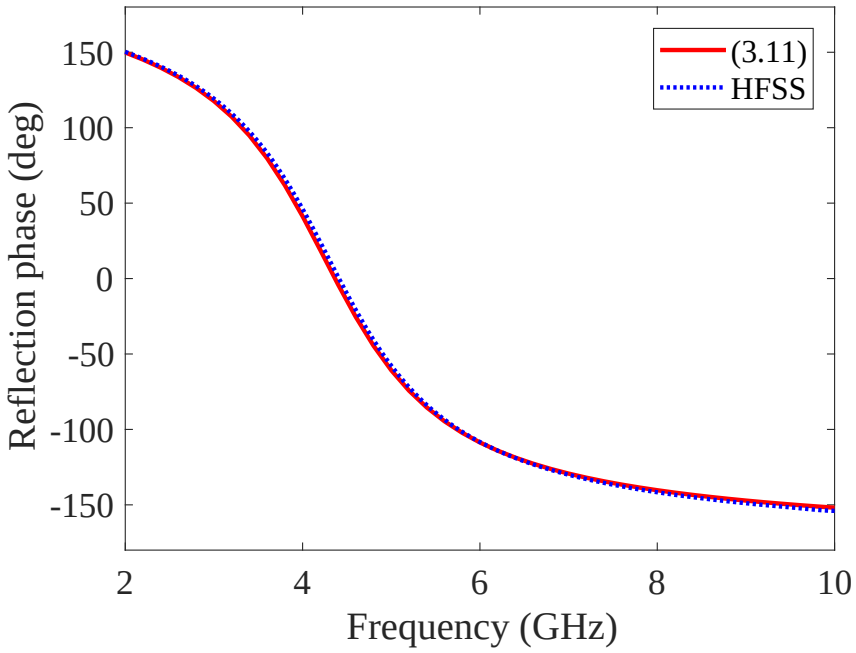

Figure 3.9: Reflection Phase of a Unit Cell.

The phase of Fig. 3.9 is for a unit cell printed on Rogers RT/Duroid-5880 substrate with $w = 8$ mm (0.314 in), $g = 1$ mm (0.039 in), and $h = 5.08$ mm (0.2 in). The unit cell behaves as a PMC (reflection phase = 0°) at 4.4 GHz, which is referred to as the *resonant frequency*. While the unit cell surface exhibits an inductive reactance below the resonant frequency, it possesses a capacitive reactance above the resonant frequency. The distribution of the reflection phase from +180 to -180 establishes the mushroom structures as suitable ground planes for low profile antennas. Furthermore, excellent agreement is observed between the analytical and numerical data.

3.4 Circularly Symmetric Surface

After the mushroom-like surfaces were introduced in the literature, various geometries and shapes that behave like HISs have been proposed. Recently, a circularly symmetric structure has been studied and reported as a superior ground plane for

curvilinear radiating elements [15]. In this section, circular HIS structures are reviewed and simulated using HFSS. The simulation arrangement for such geometry differs from the mushroom unit cell, and it will be detailed in this section.

Circular HIS structures behave similarly to mushroom structures when the surface is illuminated by electromagnetic plane waves. The phase of the reflected field varies from $+180^o$ to -180^o. However, a *unit ring*, instead of the unit cell, simulation is performed to obtain the reflection phase of the structure. The reason is that circular structures are infinite along the radial direction and finite along the angular dimension [16]. Fig. 3.10 illustrates the geometry of a circular HIS.

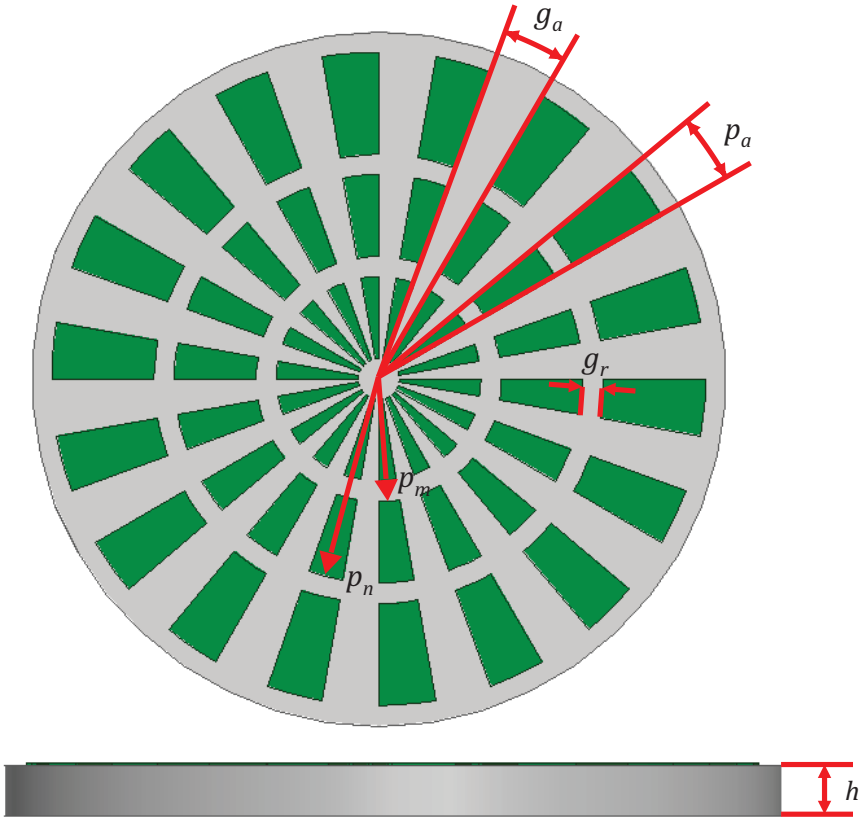

Figure 3.10: Geometry of a Circular HIS.

The reflection phase of a circular HIS structure can be obtained by applying PMC boundary conditions to the inner and outer surfaces of a coaxial waveguide, as shown in Fig. 3.11. Cylindrical TEM^z waves at normal incidence are then launched to illuminate the surface, thus allowing for the reflection phase to be captured.

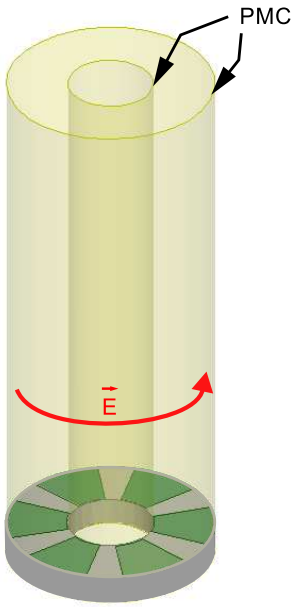

Figure 3.11: Unit Ring of a Circular HIS.

A simulation has been performed with Ansys HFSS to obtain the phase diagram of a circular HIS. The refection phase illustrated in Fig. 3.12 is for a unit ring with a patch angle of $p_a = 40^o$, a gap angle of $g_a = 20^o$, and a radial gap of $g_r = 0.2$ mm (0.007 in). The patches are printed on a Rogers RT/Duroid-5880 substrate of thickness (h) 5.08 mm (0.2 in). As illustrated in Fig. 3.12, the unit ring resonates (possesses zero reflection phase) at 4.5 GHz. The resonance can be shifted by changing any of the parameters (p_a, g_a, h, and g_r). Similar to mushroom surfaces, an analytical quasi-static model [15] can be used to determine the resonant frequency, capacitance, inductance, and the surface impedance of the circular unit ring. The capacitance

is due the fringing effect between the two adjacent patches, while the inductance is attributed to the grounded substrate. The capacitance and the inductance can be represented by [15]

$$C = \frac{p_a \epsilon_o (1+\epsilon_r)}{\pi} \cosh^{-1}\left(\frac{p_a + g_a}{g_a}\right)\left[p_n \ln\frac{p_n}{p_m} - p_n + p_m\right] \tag{3.12}$$

$$L = \mu h \tag{3.13}$$

Once the capacitance and the inductance are found, (3.10) and (3.11) can be used to find the surface impedance and the reflection coefficient.

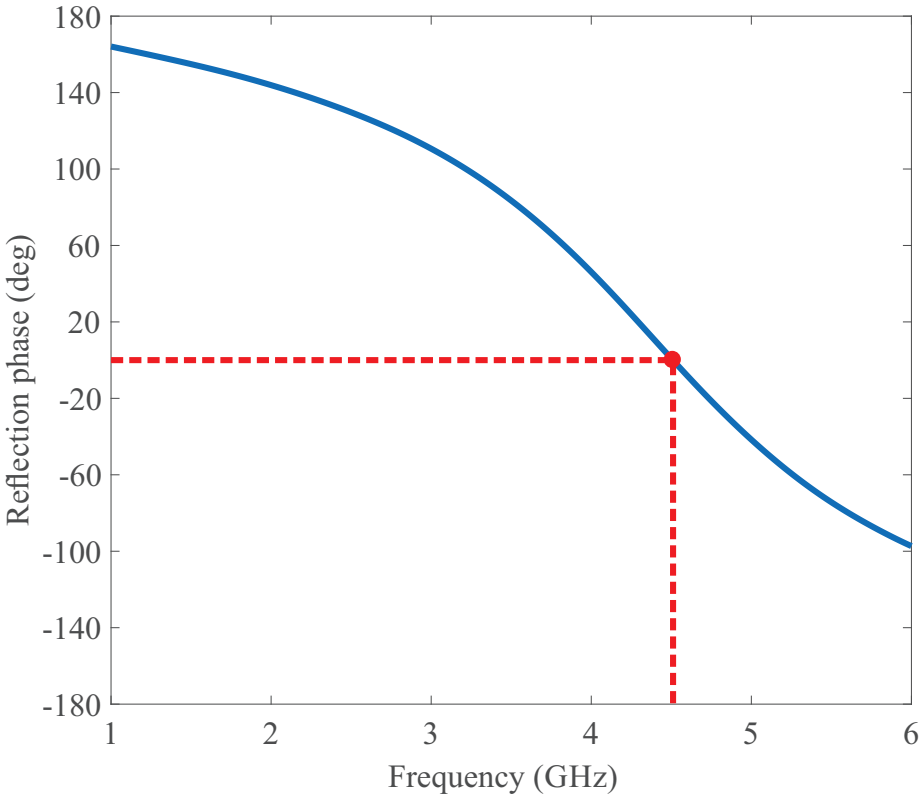

Figure 3.12: Reflection Phase of a Circular HIS Unit.

Chapter 4

DISPERSION AND MATERIAL CHARACTERIZATION

Modifying the surface characteristics have found many attractive engineering applications. Such a modification alters both the surface reflection and dispersion behavior of the structure. PEC and PMC ground planes have fixed surface impedances, which are zero and infinity, respectively. For some applications, altering the surface impedance is required to achieve a specific behavior over a certain frequency range. Slow wave antennas, leaky wave antennas, and choke ring antennas are some of the common antenna applications that depend on altering the surface impedance.

In the first section of this chapter, various methods of modifying the surface impedance are outlined. In addition, the dispersion behavior is analytically obtained and compared with HFSS to verify the analytical solution. In the second part, it is demonstrated how the dispersion diagram can be used to define possible resonances if these engineered surfaces are utilized as radiating elements.

4.1 Corrugated PEC

As discussed in Section 3.1, the modified surface possesses a high impedance when the polarization of the electric field is perpendicular to the corrugation, and a low impedance when the electric field is parallel to the grooves [6].

The dispersion behavior for the corrugated PEC can be obtained using the transverse resonance method (TRM), as illustrated in Fig. 4.1. The input impedance looking downward (Z_{in}^{-}) can be approximated as a shorted transmission line [32] with the assumption that only the TEM mode is being supported within the grooves. The input impedance looking upward (Z_{in}^{+}) is free space TM or TE wave impedance. In

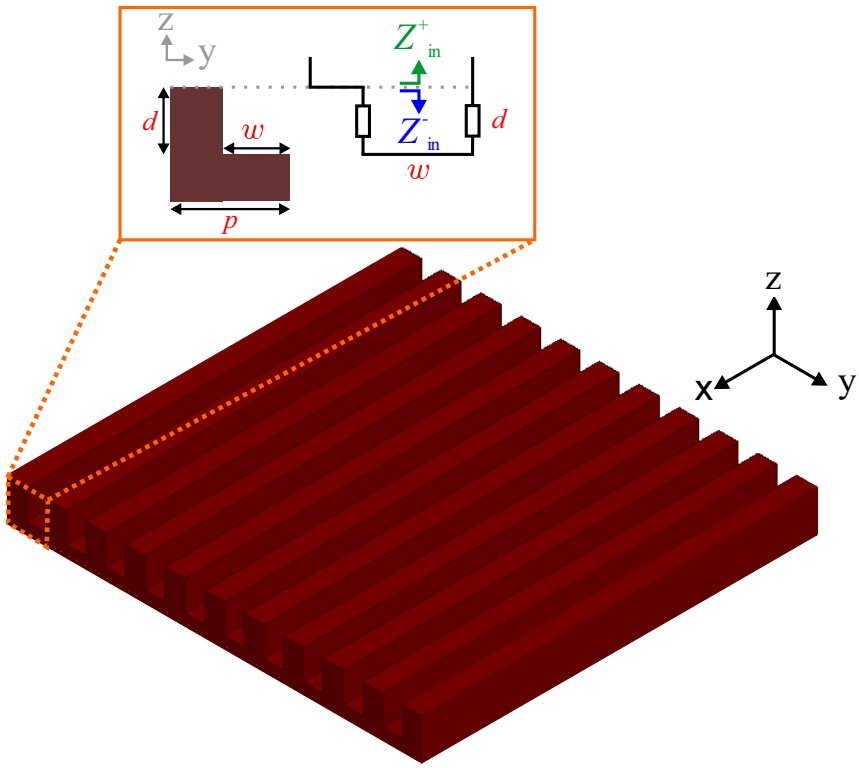

Figure 4.1: Geometry of a Corrugated Surface, with Its Equivalent Transmission Line Model.

this section, only the dispersion of the fundamental mode (TM) is considered. Therefore, the dispersion equation for corrugated PEC can be written as [32]

$$Z_{in}^{+} = -Z_{in}^{-} \tag{4.1}$$

$$\frac{\beta_{zo}}{\omega_o \varepsilon_o} = j\left(\frac{w}{p}\right)\eta_o \tan(\beta_o d) \tag{4.2}$$

$$\frac{\sqrt{\beta_o^2 - \beta_{yo}^2}}{\omega_o \varepsilon_o} = j\left(\frac{w}{p}\right)\eta_o \tan(\beta_o d) \tag{4.3}$$

Equation (4.3) provides high accuracy when $w < \lambda_o/10$ [32]. To demonstrate the accuracy of (4.3), the dispersion of corrugated PEC is calculated in HFSS utilizing the Eigenmode solver. A single period of the corrugated PEC is modeled with master and slave boundary conditions assigned to each sidewalls as depicted in Fig. 4.2. In addition, a Perfect Matching Layer (PML) boundary is placed at the top face of the

model to reduce the reflection effect and truncate the computational domain. The dispersion diagram is solved in HFSS and analytically for a corrugated metal with $w = 2$ mm, $d = 2.9$ mm, and $p = 3$ mm. An excellent agreement is observed between the simulated and analytical results, as illustrated in Fig. 4.3.

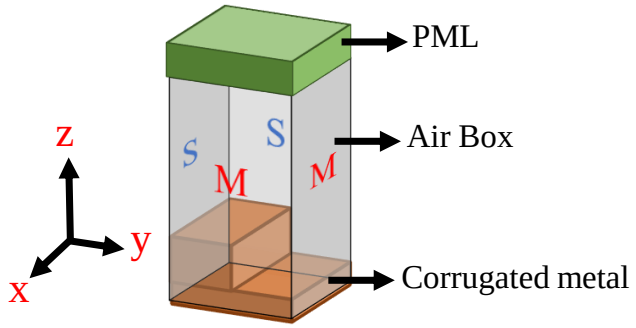

Figure 4.2: Corrugated Surface Setup to Calculate the Dispersion in HFSS. The Letters M and S Printed on the Wall Represent the Assigned Master and Slave Boundary Conditions.

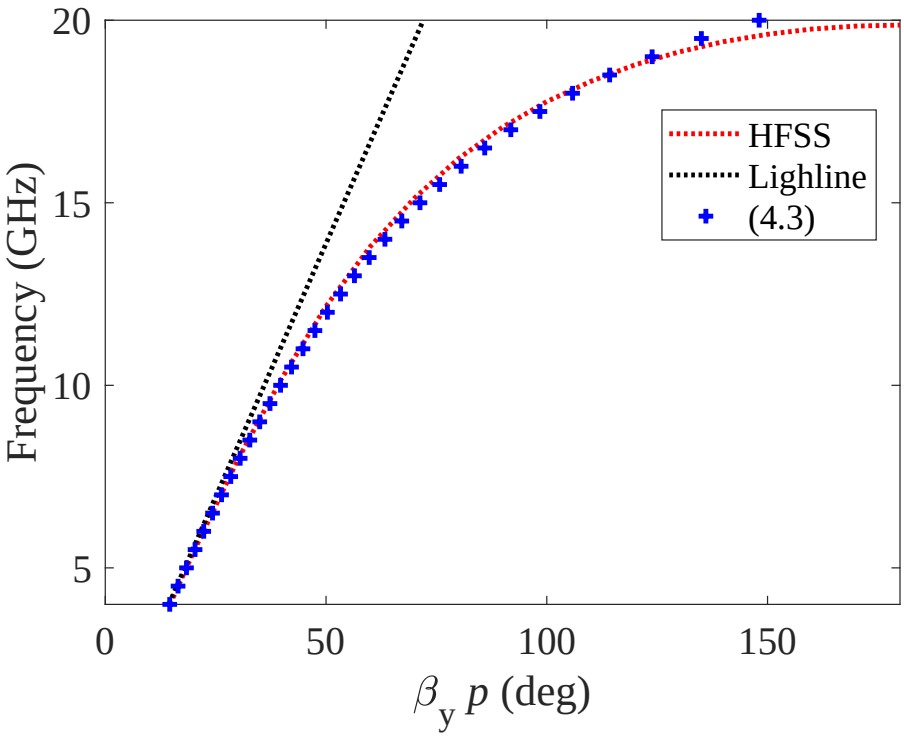

Figure 4.3: Analytical and Simulation Comparison of the Calculated Dispersion Diagram of a Corrugated PEC.

For some applications, e.g. leaky wave antennas, acquiring the surface impedance in the propagation direction is an essential task to control the radiation beam. Therefore, the TM impedance of the corrugated metal can be calculated by

$$Z_{TM} = Z_o \sqrt{1 - \left(\frac{\beta_y}{\beta_o}\right)^2} \tag{4.4}$$

where β_y is the phase in the y-direction, as represented in Fig. 4.3, and $\beta_o = \omega\sqrt{\mu_o \varepsilon_o}$.

4.2 Dielectric Covered Flat PEC

An alternative approach to modify the surface impedance of a metallic plate is to coat it with a dielectric material. The thickness and the dielectric properties of the dielectric define the TM and TE mode behaviors. Since only the dominant mode

is considered in this section, the following analysis is only focused on the TM mode. The dispersion diagram for a grounded dielectric can be calculated utilizing the TRM (Transverse Resonance Method), as depicted in Fig. 4.4. To simplify the analysis, we assume the ground plane is infinite lying on the $xy-$plane, and there is no field variations in the $x-$direction, and the wave traveling in the $y-$direction.

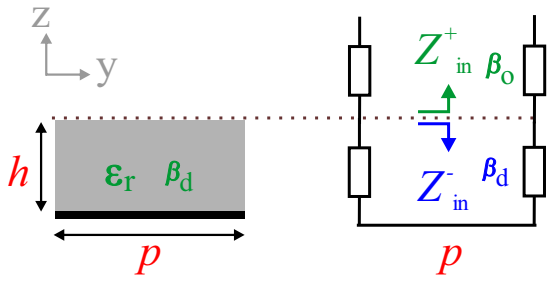

Figure 4.4: Geometry of a Grounded Dielectric, with Its Equivalent Transmission Line Model.

The input impedance looking downward (Z_{in}^{-}) can be approximated as TM impedance shorted at the end. On the other hand, the input impedance looking upward (Z_{in}^{+}) is the TM impedance in the free space. The dispersion for grounded dielectric can be obtained as [6]

$$Z_{in}^{+} = -Z_{in}^{-} \tag{4.5}$$

$$\frac{\beta_{zo}}{\omega\varepsilon_o} = -j\left(\frac{\beta_{zd}}{\omega\varepsilon_d}\right)\tan(h\,\beta_{zd}) \tag{4.6}$$

$$\frac{\sqrt{\beta_o^2-\beta_y^2}}{\omega\varepsilon_o} = -j\,\frac{\sqrt{\beta_d^2-\beta_y^2}}{\omega\varepsilon_d}\tan(h\sqrt{\beta_d^2-\beta_y^2}) \tag{4.7}$$

where h is the thickness of the substrate, β_o and β_d are the phase constants in free space and the dielectric, respectively. Similar to the corrugated PEC, the dispersion diagram for a grounded dielectric is obtained exploiting HFSS to compare with (4.7). Figure 4.5 displays the modeled grounded dielectric with master and slave boundaries assigned to the walls.

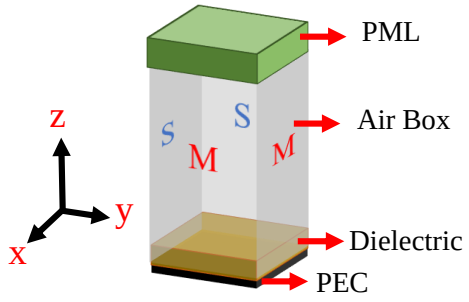

Figure 4.5: HFSS Setup for Calculating the Dispersion Diagram. The Master (M) and Slave (S) Boundary Conditions are Assigned to the Walls.

Two dielectric materials are considered in this analysis, and both have the same thickness ($h = 5.08$ mm). The first dielectric is Rogers RT/Duroid 5880 ($\varepsilon_r = 2.2$), and the second dielectric is Rogers RT/duroid 6010 ($\varepsilon_r = 10.2$). An excellent agreement is observed between (4.7) and the simulated results for both dielectric materials, as displayed in Fig. 4.6. Similar to the corrugated PEC, the TM surface impedance in the $y-$direction can be calculated utilizing (4.4)

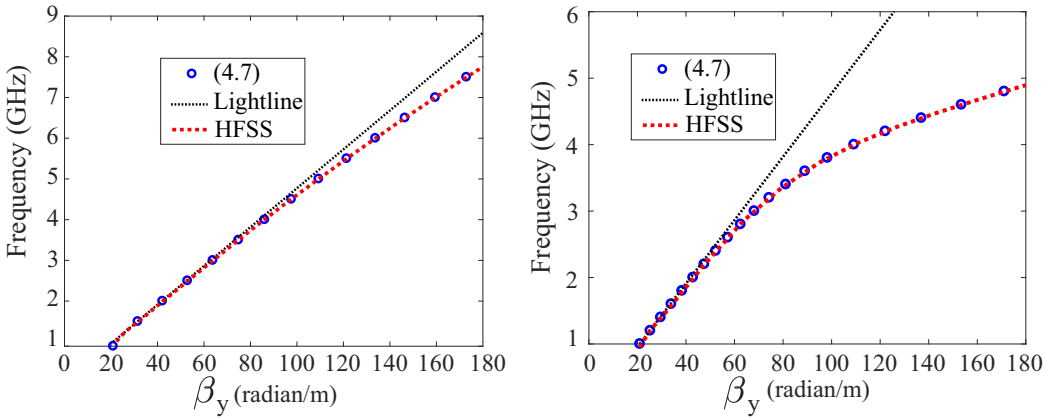

Figure 4.6: Dispersion Diagram for a Dielectric Covered PEC. Left: Rogers RT/Duroid 5880 ($\varepsilon_r = 2.2$). Right: Rogers RT/duroid 6010 ($\varepsilon_r = 10.2$).

4.3 Multi-Dielectric Covered Flat PEC

The propagation in the grounded dielectric can be further altered by having different dielectric materials side by side, as depicted in Fig. 4.7. To simplify the analysis, let us assume that there are two side-by-side grounded dielectrics which have the same thickness (h), they are infinite in the x-direction ($\beta_x = 0$), and the wave traveling in y-direction. Dielectric 1 and 2 are finite along the y-axis, and their lengths are p_1 and p_2, respectively. The dispersion equation for a single dielectric (4.7) has to be

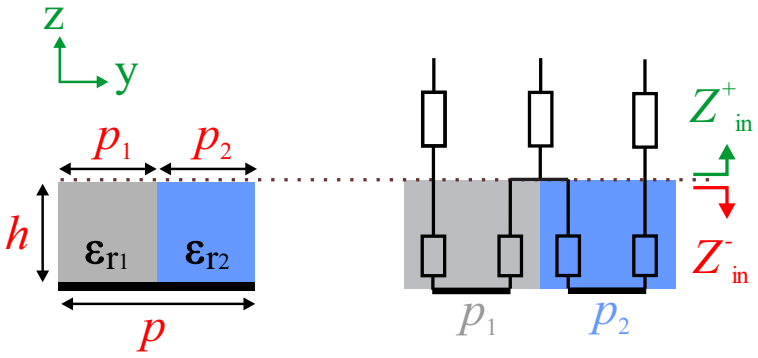

Figure 4.7: Geometry of Multiple Dielectric Materials Covering a Flat PEC, and Its Equivalent Transmission Line Model.

modified to include the effect of the second dielectric. Only the right hand side of (4.7) needs to be altered as the impedance looking downward (Z^+_{in}) is the sum of the impedances contributed by the two dielectric materials. Therefore,

$$Z^+_{in} = -Z^-_{in} \tag{4.8}$$

$$\frac{\beta_{zo}}{\omega\varepsilon_o} = -\left(\frac{p_1}{p}\right) Z_{dielectric_1} - \left(\frac{p_2}{p}\right) Z_{dielectric_2} \tag{4.9}$$

$$Z_{dielectric_1} = j\left(\frac{\beta_{zd1}}{\omega\varepsilon_{d1}}\right) \tan\left(h\,\beta_{zd1}\right) \tag{4.10}$$

$$Z_{dielectric_2} = j\left(\frac{\beta_{zd2}}{\omega\varepsilon_{d2}}\right) \tan\left(h\,\beta_{zd2}\right) \tag{4.11}$$

$$\beta_{zo} = \sqrt{\beta_o^2 - \beta_{yo}^2} \tag{4.12}$$

$$\beta_{zd1} = \sqrt{\beta_{d1}^2 - \beta_{yd1}^2} \tag{4.13}$$

$$\beta_{zd2} = \sqrt{\beta_{d2}^2 - \beta_{yd2}^2} \tag{4.14}$$

Based on the phase matching conditions, the phase constant at the air and dielectric interfaces has to be the same. Thus,

$$\beta_{yd1} = \beta_{yo} = \beta_{yd2} = \beta_y \tag{4.15}$$

Therefore, (4.9) can be expressed as [35]

$$\frac{\sqrt{\beta_o^2 - \beta_y^2}}{\omega\varepsilon_o} = \psi_1 + \psi_2 \tag{4.16}$$

$$\psi_1 = -j \left(\frac{p_1}{p}\right) \frac{\sqrt{\beta_{d1}^2 - \beta_y^2}}{\omega\varepsilon_{d1}} \tan\left(h\sqrt{\beta_{d1}^2 - \beta_y^2}\right)$$

$$\psi_2 = -j \left(\frac{p_2}{p}\right) \frac{\sqrt{\beta_{d2}^2 - \beta_y^2}}{\omega\varepsilon_{d2}} \tan\left(h\sqrt{\beta_{d2}^2 - \beta_y^2}\right)$$

Equation (4.16) can be generalized to N dielectric materials with different thicknesses, and can be expressed as

$$\frac{\sqrt{\beta_o^2 - \beta_y^2}}{\omega\varepsilon_o} = \sum_{n=1}^{N} -j \left(\frac{p_n}{p}\right) \frac{\sqrt{\beta_{dn}^2 - \beta_y^2}}{\omega\varepsilon_{dn}} \tan\left(h_n\sqrt{\beta_{dn}^2 - \beta_y^2}\right) \tag{4.17}$$

where N is the number of dielectric materials placed next to each other, and h_n is the thickness of the nth material. Equation (4.17) can be also used for a corrugated grounded dielectric, as illustrated in Fig. 4.8.

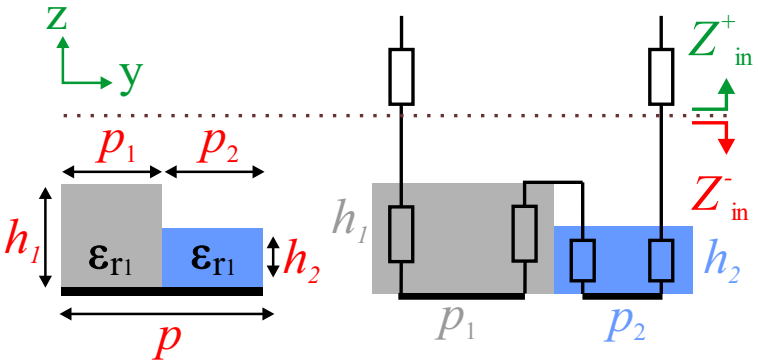

Figure 4.8: Geometry of a Corrugated Dielectric on a Flat PEC, with Its Equivalent Transmission Line Model.

To verify the validity of (4.17), two structures are modeled by HFSS and the dispersion is obtained for multiple lengths for the two structures. The two structures considered are:

1. Two side-by-side dielectric materials (Rogers RT/Duroid 5880 ($\varepsilon_r = 2.2$) and Rogers RT/duroid 6006 ($\varepsilon_r = 6.15$)) covering a flat PEC are considered. The thickness of both dielectrics (h) is 5.08 mm. The structure is similar to Fig. 4.7 with a period of ($p = p_1 + p_2$). The lengths of the first dielectric (Rogers RT/Duroid 5880) and the second dielectric (Rogers RT/duroid 6006) are p_1 and p_2, respectively. The dispersion is performed for different lengths of the two dielectrics, as illustrated in Fig. 4.9.

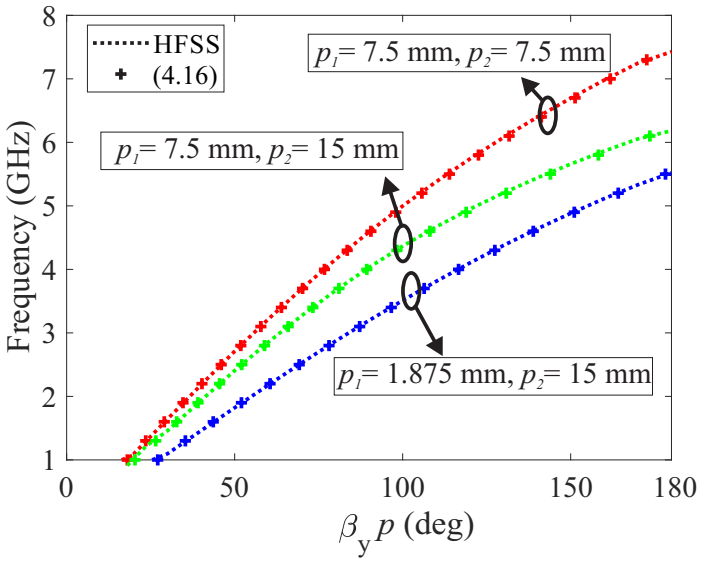

Figure 4.9: Dispersion of Two Side-by-Side Dielectric Materials Covering a PEC with Different Lengths for the Two Substrates.

2. Corrugated grounded dielectric (Rogers RT/Duroid 5880) with thicknesses (h_1) of 5.08 mm and (h_2) of 2.08 mm.

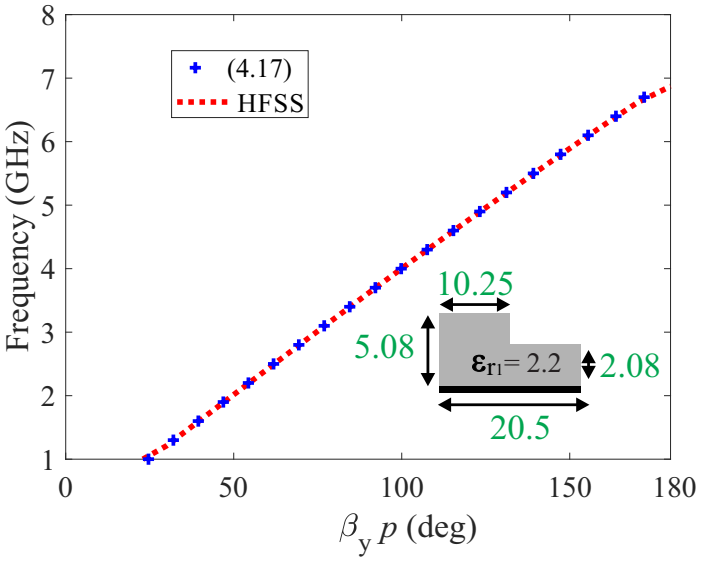

Figure 4.10: Dispersion of a Corrugated Dielectric (Rogers RT/Duroid 5880) Covering a PEC.

The simulated and the analytical (4.17) results for the two structures are compared in Figs. 4.9 and 4.10, respectively. Excellent agreements between the simulated and the analytical results are observed for the two structures. To find the surface impedance of the corrugated dielectric or the multi-dielectric covered PEC, (4.4) can be used to find the TM impedance in the $y-$direction.

4.4 Metasurface

Another approach to alter the surface impedance is to use metasurfaces, which are realized by placing metallic patches on a dielectric covered ground plane in a periodic arrangement. Although various shapes and geometries have been proposed, only square and annular sector patches are examined in this chapter.

4.4.1 Square Metasurface

The dispersion of a square patch metasurface can be calculated using the transverse resonance method, as illustrated in Fig. 4.11. Due to the loading of the metallic patch to the grounded dielectric, the impedance looking downward (Z_{in}^{-}) needs to be modified to include the grid impedance (Z_g). The grid impedance is parallel to the impedance of the grounded dielectric; therefore, it is most convince to use the admittance instead of the impedance [36].

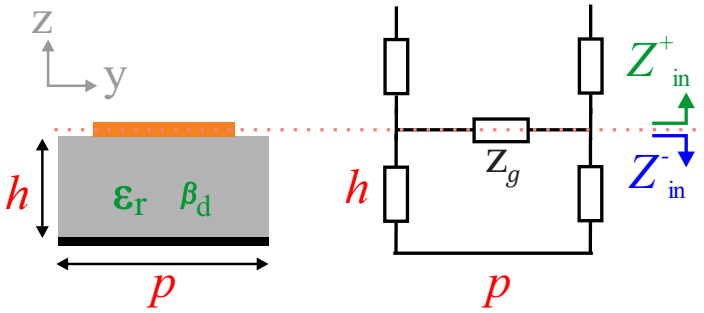

Figure 4.11: Transverse Resonance Method for a Metasurface Unit Cell.

$$Y_{in}^{+} = -Y_{in}^{-} \tag{4.18}$$

$$\frac{1}{Z_{in}^{+}} = -\frac{1}{Z_{in}^{-}} \tag{4.19}$$

$$\frac{Z_{in}^{+} + Z_{in}^{-}}{Z_{in}^{+} Z_{in}^{-}} = 0 \tag{4.20}$$

To satisfy (4.20), $Z_{in}^{+} + Z_{in}^{-} = 0$. Hence, (4.20) reduces to

$$Z_{in}^{+} = -Z_{in}^{-} \tag{4.21}$$

$$Z_{in}^{+} = -(Z_g + Z_s) \tag{4.22}$$

$$\frac{\beta_{zo}}{\omega\varepsilon_o} = -\frac{\psi_1}{\psi_2} \tag{4.23}$$

$$\begin{aligned}
\psi_1 &= j\omega\mu \frac{\tan(\beta_{zd}h)}{\beta_{zd}} \left(\frac{\beta_{zd}}{\beta_d}\right) \\
\psi_2 &= 1 - 2k_{eff}\,\alpha \frac{\tan(\beta_{zd}h)}{\beta_{zd}} \left(\frac{\beta_{zd}}{\beta_d}\right) \\
k_{eff} &= \beta_o \sqrt{\varepsilon_{eff}} \\
\varepsilon_{eff} &= \frac{\varepsilon_r + 1}{2} \\
\alpha &= \frac{p\,k_{eff}}{\pi} \ln\left(\frac{1}{\sin\frac{\pi\,g}{2\,p}}\right)
\end{aligned}$$

where p is the period of the metasurface, g is the gap between the metallic patches, $\beta_o = \omega\sqrt{\mu\varepsilon_o}$, and $\beta_d = \beta_o\sqrt{\varepsilon_r}$. According to the phase matching conditions, along the air-grid interface, β_{yd} must be equal to β_{yo}. Thus,

$$\beta_{zd} = \sqrt{\beta_d^2 - \beta_{yd}^2} = \sqrt{\beta_d^2 - \beta_y^2} \tag{4.24}$$

$$\beta_{zo} = \sqrt{\beta_o^2 - \beta_{yo}^2} = \sqrt{\beta_o^2 - \beta_y^2} \tag{4.25}$$

By substituting (4.24) and (4.25) into (4.23), the dispersion of the metasurface structure can be obtained. To verify the solution of (4.23), the dispersion for a metasurface structure is calculated exploiting full-wave simulation software. The metasurface unit cell is modeled in HFSS, and the appropriate boundary conditions are applied, as illustrated in Fig. 4.12.

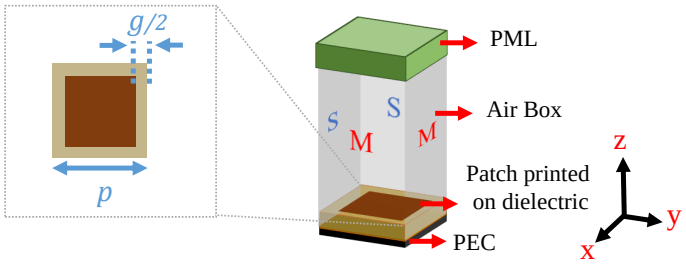

Figure 4.12: HFSS Setup to Extract the Dispersion of a Square Metasurface.

The simulated metasurface has a period $p = 20.5$ mm and a gap $g = 4.5$ mm. The metallic patch is printed on Rogers RT/Duroid 5880 ($\varepsilon_r = 2.2$) with thickness $h = 5.08$ mm. The simulated and analytical results are plotted in Fig. 4.13. An excellent agreement is observed at lower frequencies, but the discrepancy increases at higher frequency.

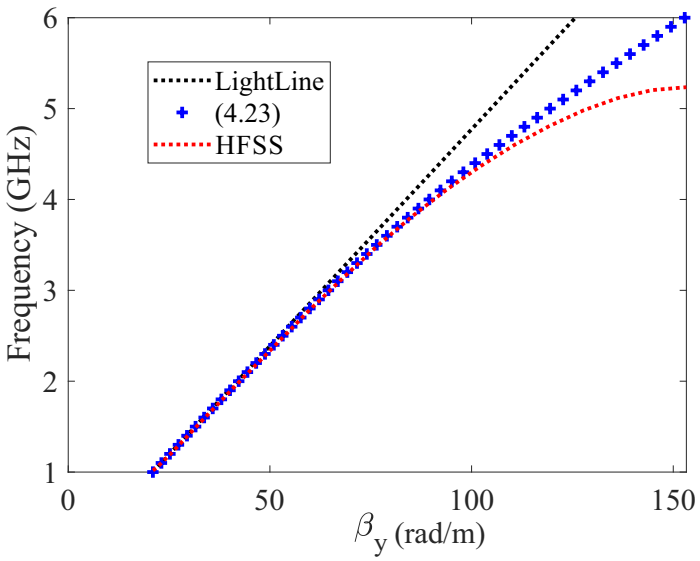

Figure 4.13: Analytical and Simulated Comparison of Dispersion Diagrams of a Square Metasurface.

4.4.2 *Annular Sector Patch Metasurface*

Another popular metasurface geometry is the annular sector metallic patch printed on a circular trapezoid grounded dielectric, as displayed in Fig. 4.14. The annular sector unit is suitable for curvilinear radiating elements [15].

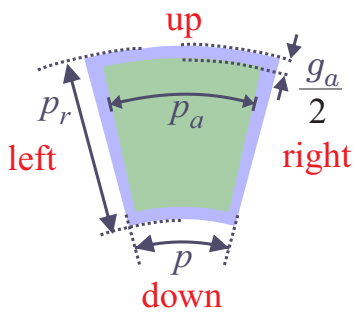

Figure 4.14: Layout of an Annular Sector Metasurface Unit Cell.

The dispersion of an annular sector cannot be obtained directly in HFSS, as the master-slave boundaries cannot be applied to neither the non-parallel side-walls (right and left walls as shown in red in Fig. 4.14), nor to the dissimilar lengths of the opposite walls (up and down walls). To establish an approximate model to calculate the dispersion of the annular sector, the effect of the transverse width (y-axis) for a rectangular unit cell is analyzed as the wave propagates along the longitudinal direction (x-axis). Various shapes of the metallic patches are considered, namely, trapezoid (T), square (S), and rectangular (R), as depicted in Fig. 4.15. For the different metallic shapes, the dispersion along the x-direction is obtained, and the results are plotted in Fig. 4.15.

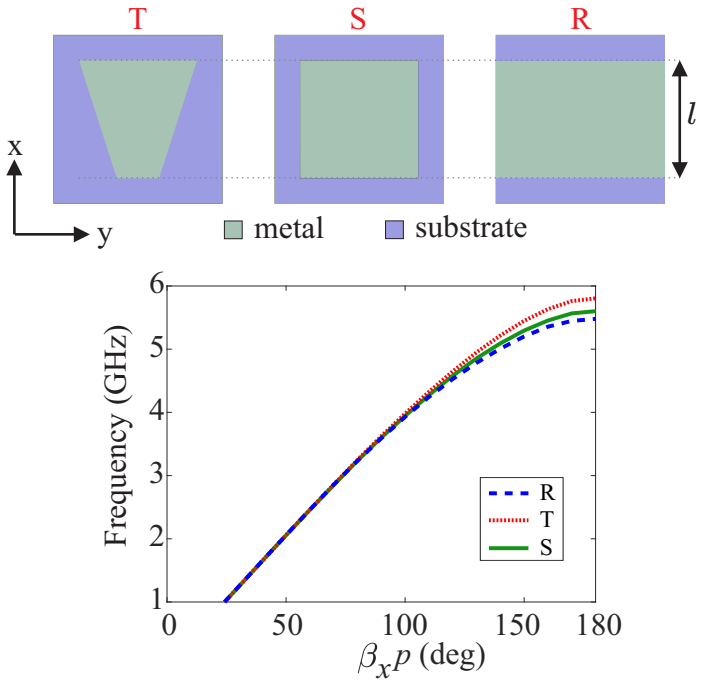

Figure 4.15: Dispersion of Different Shapes of Patches Loaded on a Rounded Dielectric.

As observed, varying the transverse width has insignificant impact on the dispersion; therefore, the dispersion for the annular sector can be approximately acquired by finding the dispersion of an equivalent model that has the same length and gap along the propagation direction. For example, for an annular sector patch with a period $p_r = 23.7$ mm and a gap $g_a = 1.77$ mm, the approximate dispersion can be found by modeling a rectangular metasurface with the same period (p_r) and same gap (g_a), as displayed in Fig. 4.16.

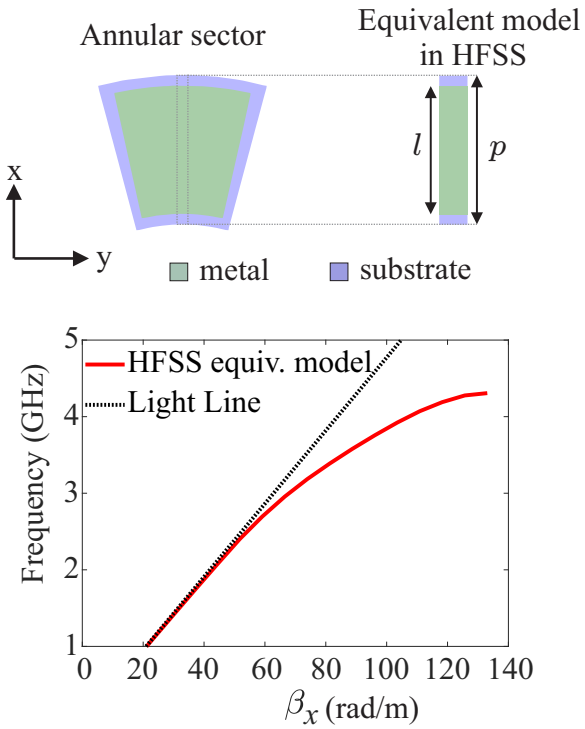

Figure 4.16: Approximate Dispersion of the Annular Sector Metasurface.

4.5 Extracting Resonances From Dispersion Diagrams

In the previous sections, the dispersion diagrams for multiple structures are calculated; however, it has not been demonstrated how useful these plots are when the aforementioned surfaces are used as radiating elements. For simple structures (e.g. square patch antenna) the possible resonances can be determined from the cavity model analysis. Nevertheless, the cavity model for modified surfaces (e.g. corrugated plate) is cumbersome as the resonances depend on multiple parameters. Alternatively, the dispersion diagram can be used instead to find the possible resonances for most complicated periodic surfaces. To demonstrate the validity of this approach, the resonances of a rectangular patch will be extracted from the dispersion diagram, and it will be compared to those obtained by the cavity model.

4.5.1 Rectangular Patch Dispersion and Resonances

The cavity model treats the patch antenna as a parallel plate waveguide with magnetic walls along the perimeter of the substrate. The TM mode resonances for a rectangular patch printed on non-magnetic dielectric material is determined based on the cavity model as [32]

$$f_{rmnp} = \frac{1}{2\pi\sqrt{\mu_o\,\varepsilon_d}}\,\beta_d \tag{4.26}$$

$$= \frac{1}{2\pi\sqrt{\mu_o\,\varepsilon_d}}\,\sqrt{\beta_x^2+\beta_y^2+\beta_z^2} \tag{4.27}$$

where the directional wavenumbers are defined as

$$\begin{aligned} \beta_x\, l &= m\pi \qquad m = 0,1,2,... \\ \beta_y\, w &= n\pi \qquad n = 0,1,2,... \\ \beta_z\, h &= p\pi \qquad p = 0,1,2,... \end{aligned} \tag{4.28}$$

if $l > w > h$, the dominant resonance occurs when $\beta_x\, l = \pi$, and it is defined as TM^z_{100}. This resonance is contributed by the length of the patch, which is along the x-axis. Similarly, the resonance along the y-axis (TM^z_{010}) occurs when $\beta_y\, w = \pi$. Therefore, the dispersion diagram can be exploited to find the resonances along the $x-$ and $y-$axes. For clarification purposes, a rectangular patch with a length of 25 mm and a width of 10 mm is considered. The patch is printed on Rogers RT/Duroid 5880 with a thickness of 5.08 mm. The resonances along the x- and y-axes (TM^z_{100} and TM^z_{010}) based on the cavity model (4.27) are 4 and 10 GHz, respectively. The same resonances are obtained using the dispersion diagram of a parallel plate filled with Rogers RT/Duroid 5880 dielectric, as depicted in Fig. 4.17.

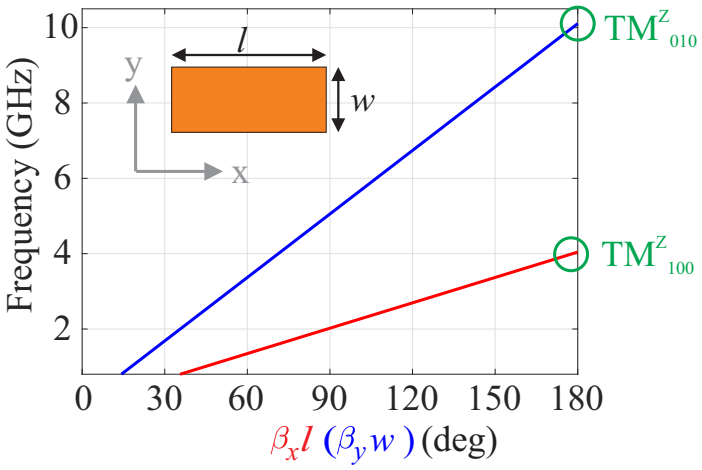

Figure 4.17: Dispersion of a Parallel Plate Filled with Rogers RT/Duroid 5880 Dielectric.

4.5.2 Metasurface Resonances

The resonances of a metasurface, similar to the patch antenna, can be extracted from the dispersion diagram by defining the frequency at which the electrical length is 180°. The dispersion diagram for a metasurface is usually calculated for a single period; however, for practical applications, multiple numbers of periods are deployed. As the number of periods increases, the dominant resonance shifts to a lower frequency, and higher order resonances begin to appear within the frequency range of the dispersion diagram. To better illustrate this point, consider the patch antenna discussed in the previous section, with a length 25 mm and a width of 10 mm, whose TM^z_{100} resonance is 4 GHz. Now if the length is doubled (l = 50 mm), TM^z_{100} will shift toward a lower frequency (2 GHz) and the 4 GHz will be at higher-order resonance, namely TM^z_{200}. Similarly, if we increase the periodicity of the metasurface, the dominant resonance for a single period becomes a higher order resonance, and the new dominant resonance shifts to a lower frequency. Figure 4.18 sheds insight on this concept exploiting the electrical length, and it displays how this can be applied

to both patch and metasurface structures. The dispersion diagram for a single period can be extended to account for multiple periodicities by multiplying the phase delay by the number of the periodicity.

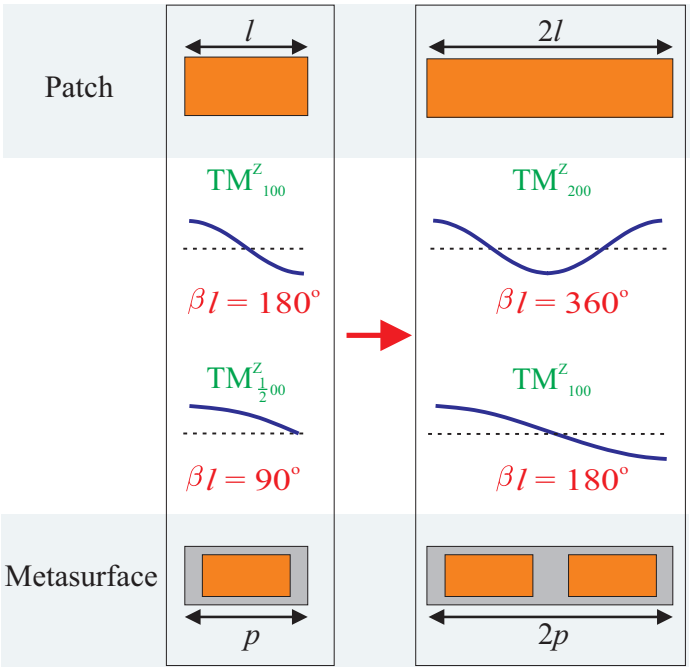

Figure 4.18: The Impact of Doubling the Electrical Length on the Possible Resonances.

With the modified dispersion diagram, all possible resonances can be easily extracted using

$$\beta_{(x,y)}\, P_{(x,y)}\, N_{(x,y)} = m\pi \qquad m = 1, 2, 3, .. \tag{4.29}$$

where β is the longitudinal wavenumber, P is the periodicity of the metasurface, and N is the number of periods. Equation (4.29) can be applied to find the resonances along the x and y directions. The dispersion diagram for the metasurface illustrated in Fig. 4.13 is re-calculated again for 2 and 3 periods in addition to the single period. A full-wave simulator (HFSS) is used to obtain the dispersion for multiple periodicities and to compare the results to (4.29). The eigenmode solver in HFSS repeats

a symmetrical dispersion behavior after it reaches the 180° phase delay; therefore, HFSS curves can only show up to 180° (or multiples of it) phase delay, as depicted in Fig. 4.19. As observed in Fig. 4.19, when the number of periods is multiplied by the dispersion curve of a single period, as stated in (4.29), the full dispersion behavior can be captured where the phase delay can exceed 180°; hence, all possible resonances, including higher order resonances, can be easily extracted. As demonstrated in the figure, these resonances shift as the number of the periodicity changes. In addition to this method of extracting the resonances, there is another approach, which will be discussed in Chapter 6.

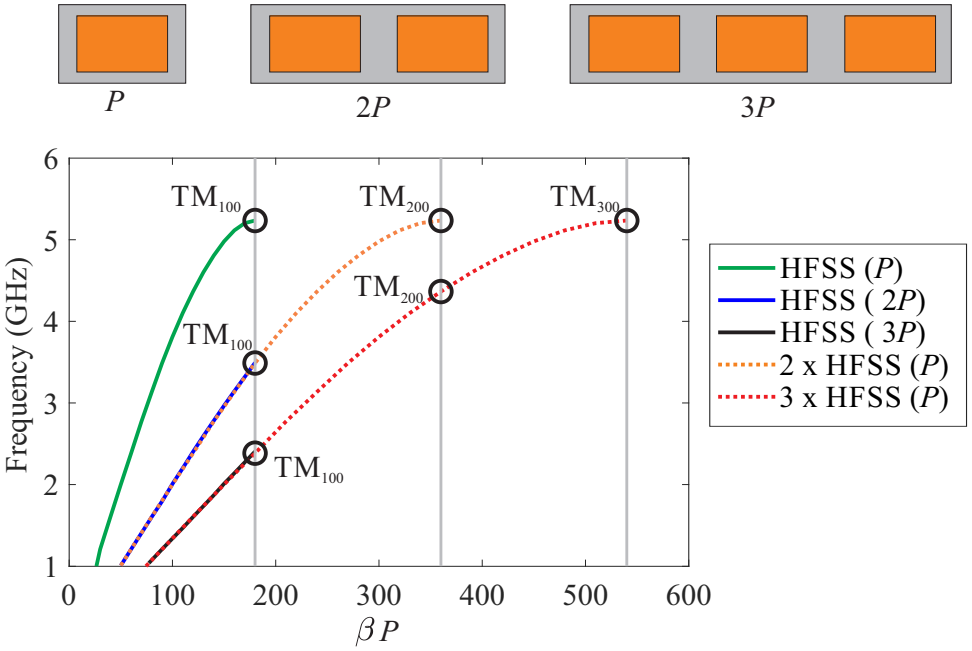

Figure 4.19: Dispersion of Multiple Periods of Rectangular Metasurfaces.

Chapter 5

HYBRID CIRCULAR GROUND PLANES FOR HIGH REALIZED GAIN LOW-PROFILE LOOP ANTENNAS

5.1 Introduction

Dipole and monopole antennas are the most classic radiating elements that have been thoroughly analyzed [32]. If these radiating elements are placed in free space, they have a low directivity due to their omnidirectional characteristic. For example, small electric dipoles and loop antennas have a free-space directivity of 1.761 dB [32]. The continuous search for highly directive radiating elements has led to the introduction of different methods to improve the directivity. One solution is to design array antennas; however, this approach requires the use of multiple elements, which need a complex feeding network. Another solution is to place the radiating element above a ground plane. In this case, the ground plane behaves like a reflector, which can improve the directivity. For example, a directivity of 8 dB was observed for a 0.48λ long dipole positioned 0.02λ above a rectangular HIS [33]. Another example, a loop antenna with a circumference of 1.88λ (at 3 GHz) placed 0.01λ above an annular sector HIS resulted in a directivity of 8.5 dB [15].

In this section, a circular loop element is embedded within annular hybrid HIS rings. The dispersion diagram and the reflection phase are utilized to analyze the HIS and determine the resonances. A printed loop antenna is used, instead of a wire type, due to its conformability to the ground plane and ease of fabrication. To establish the proposed ground plane, the performance of the printed loop antenna positioned above a grounded dielectric and above a HIS are first investigated. Later, the effective

area of the proposed design is further improved by deploying another annular ring to form the hybrid ground plane. To validate the simulated data, a prototype was fabricated and measured. An excellent agreement is observed between the two data.

5.2 Loop Antenna on Grounded Dielectric

For this study, a circular-geometry ground plane is considered as it is better suited for curvilinear radiating elements than an otherwise comparable rectangular ground plane. The loop element is designed to have a circumference of 1.3λ at 3 GHz. The loop size is determined based so the loop element, with nonuniform current distribution, attains maximum broadside directivity around the selected length [32]. As the circumference approaches λ, the current distribution along the loop's circumference is non-uniform, and it can be represented by a Fourier series [32]

$$I(\phi) = I_o + 2\sum_{n=1}^{M} I_n \cos(n\phi) \tag{5.1}$$

To have unidirectional radiation without disturbing the height profile, the loop is printed on a grounded Rogers RT/Duroid-5880 substrate (shown in Fig. 5.1). The substrate has a thickness of $h = 5.08$ mm (0.2 in) with a relative permittivity $\varepsilon_r = 2.2$. The diameter of the substrate is $D_s = 134$ mm (5.27 in). The detailed dimensions of the loop are summarized in Table 5.1. The loop is excited with a 50-Ω coaxial probe in one arm, and the other arm is shorted to the metallic ground using a via.

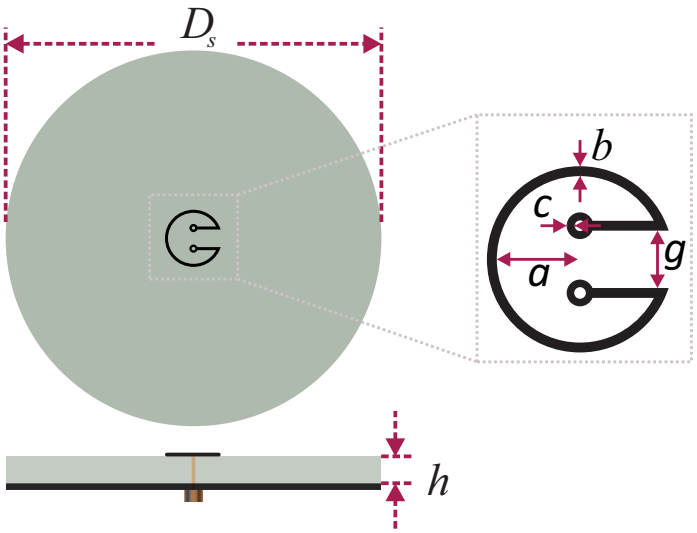

Figure 5.1: A Loop Antenna Printed on a Grounded Dielectric.

Table 5.1: Dimensions of the Loop Antenna

Parameter	**Value**
a	9.1 mm (0.36 in)
b	1.08 mm (0.04 in)
g	6.27 mm (0.25 in)
c	0.87 mm (0.03 in)

To capture the current along the circumference of the loop, a full wave simulation (HFSS) is performed and the attained distribution at 3 GHz along the ϕ direction is illustrated in Fig. 5.2. As observed, the current has a Fourier cosine distribution along the loop arm. The obtained current distribution as represented by (5.1) can be expressed as:

$$I(\phi) = 0.183 + 0.76\cos(-0.824\phi) - 0.752\cos(0.928\phi - 0.383) \tag{5.2}$$

where ϕ is the angle along the loop circumference, as illustrated in the inset of Fig. 5.2. As observed in Fig. 5.2, the expression of (5.2) indicates an excellent agreement with the extracted current values.

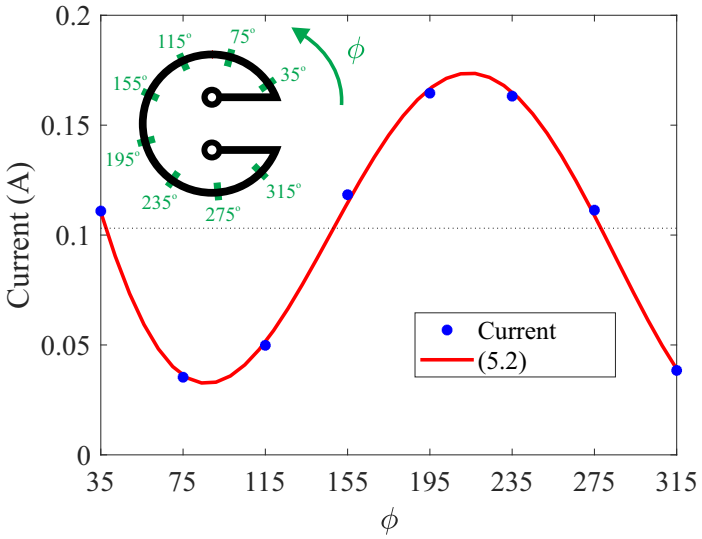

Figure 5.2: Current Distribution Along the Circumference of the Printed Loop.

To highlight the performance of the loop above a grounded dielectric, the broadside directivity and return loss are simulated over a range of frequencies and plotted in Figs. 5.3 and 5.4, respectively. As expected, a maximum directivity of 8.3 dB is observed at 3 GHZ since the circumference length is around 1.3λ; however, at that frequency, the mismatch loss is very high. Thus, basically no power is radiated, which is similar to an electric dipole positioned very closely above a PEC ground plane discussed in Chapter 2. The close proximity of the PEC shorts out the loop and results in a very low input resistance [$\mathrm{Re}(Z_{in}) = 2\Omega$] with a high capacitive reactance [$\mathrm{Im}(Z_{in}) = -68\Omega$].

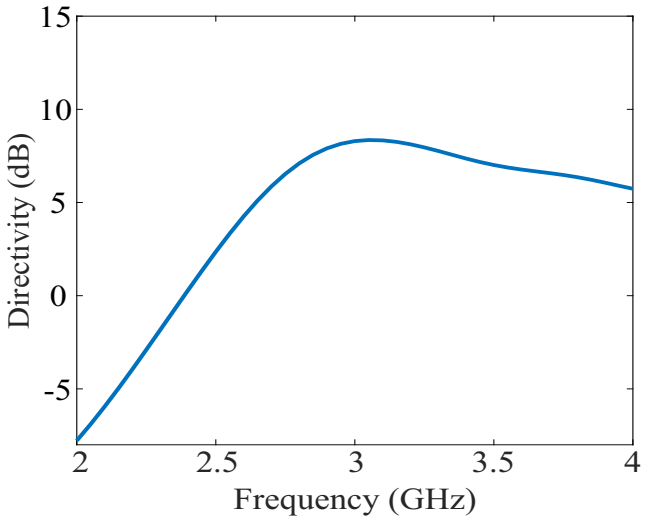

Figure 5.3: Simulated Broadside Directivity of the Loop Antenna Above a Grounded Dielectric.

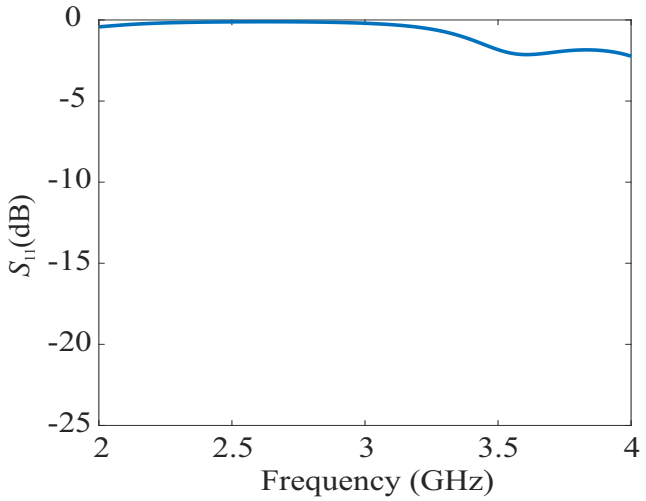

Figure 5.4: Simulated S_{11} of the Loop Antenna Placed Above a Grounded Dielectric.

5.3 Loop Antenna Loaded with Annular Sector HIS

The high mismatch loss observed for the loop antenna printed on a grounded dielectric can be reduced by introducing a structure that alters the ground plane influence. Due to the curvilinear shape of the loop element, periodic annular sectors

are considered to surround the loop. The contribution of the annular sector first is investigated exploiting the dispersion diagram. By examining the current distribution along the loop (see Fig. 5.2), it is observed that the current is maximum at $\phi = 75°$ and 235° with a phase difference of 180° between the two maxima. Consequently, if a periodic patch with a length of 0.25λ (or 90° electrical length) is populated around the loop, then the overall structure will resonate. This is analogous to a bowtie dipole with two 0.25λ arms in each side, as depicted in Fig. 5.5.

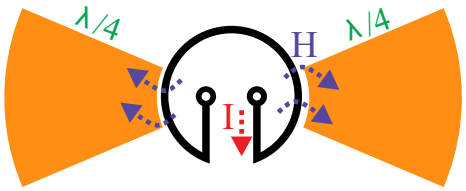

Figure 5.5: Loop Element Surrounded by Annular Sector at Each Side.

The selected annular periodic patches are similar to the circularly symmetric surface (shown in Fig. 3.11), except that one ring is used (instead of multiple rings) to obtain the required electrical length, as shown in Fig. 5.6. The substrate dielectric is Rogers RT/Duroid-5880 with a thickness $h = 5.08$ mm. The HIS section is designed on a substrate with a diameter of $d_s = 134$ mm (5.27 in), which is the same diameter used for the loop antenna positioned above a grounded dielectric discussed in the previous section. The patch angle (P_a) for all patches is 50^o, and the gap angle (g_a) between the patches is 10^o. It was noticed that the patch angle (P_a) has a pronounced impact on the input impedance; hence, it was optimized to have an input impedance of about 50Ω around the resonant frequency. The detailed dimensions of the HIS are summarized in Table 5.2.

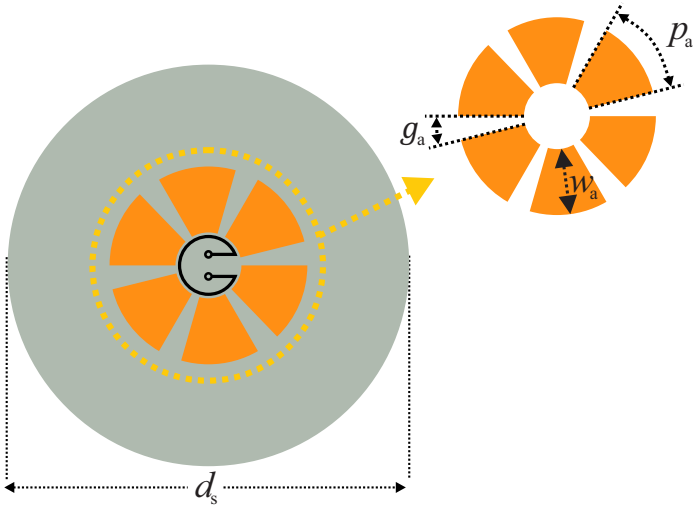

Figure 5.6: Geometry of the Loop Along with HIS Section Positioned on the Top Surface of the Grounded Dielectric.

Table 5.2: Dimensions of the Circular HIS

Parameter	**Value**
p_a	50^o
g_a	10^o
d_s	134 mm (5.27 in)
w_s	22 mm (0.86 in)

To identify the required dimension of the annular sector that possesses 90 ° electrical length at 3 GHz, the calculation of the dispersion diagram is considered. The dispersion diagram is obtained using HFSS, which was detailed in Chapter 4. The equivalent model of the annular sector has a period $p = 24$ mm, with a length $l = 22$ mm. The dispersion diagram for the equivalent model is plotted in Fig. 5.7. As displayed in the figure, the selected length meets the required electrical length at 3 GHz.

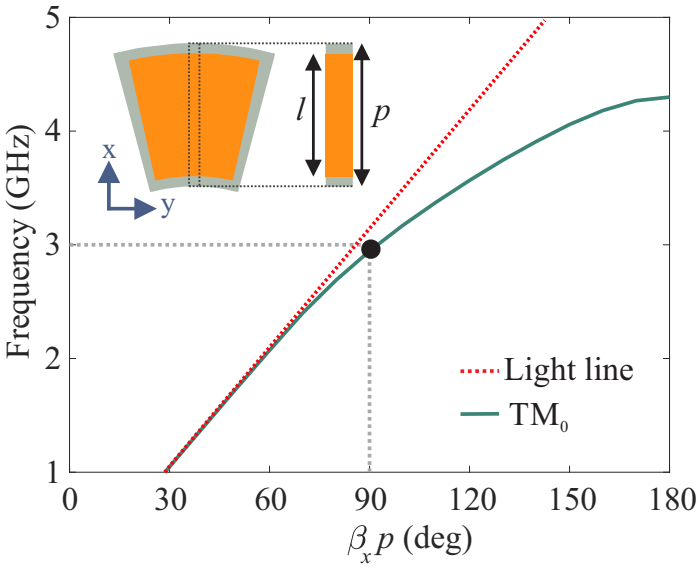

Figure 5.7: Dispersion Diagram for Annular Sector.

To demonstrate the effect of the periodic patches on the loop performance, the reflection coefficient of the loop in the vicinity of the periodic annular sectors is plotted in Fig. 5.8. As observed, the loop antenna resonates at 3 GHz with a return loss of 16 dB. In addition, the simulated broadside directivities versus frequency for a loop above a grounded dielectric and surrounded by HIS are plotted in Fig. 5.9. The directivity at 3 GHz is improved up to 9 dB, which is 0.5 dB higher compared to the loop antenna above the grounded dielectric.

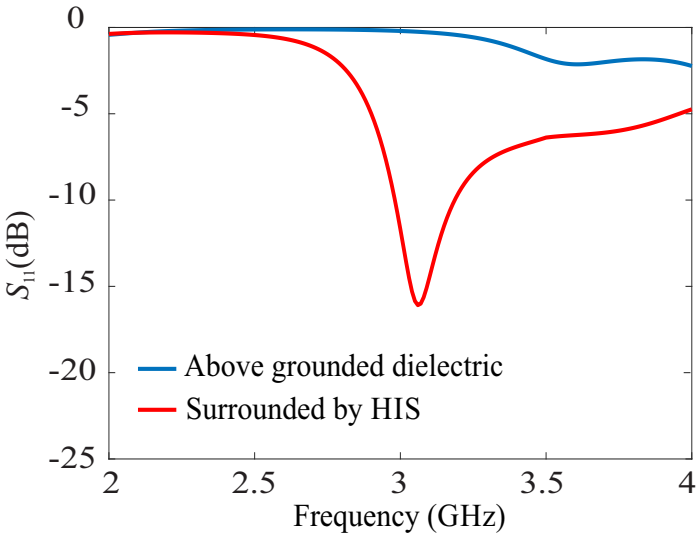

Figure 5.8: Simulated S_{11} of the Loop in the Vicinity of the HIS and Grounded Dielectric.

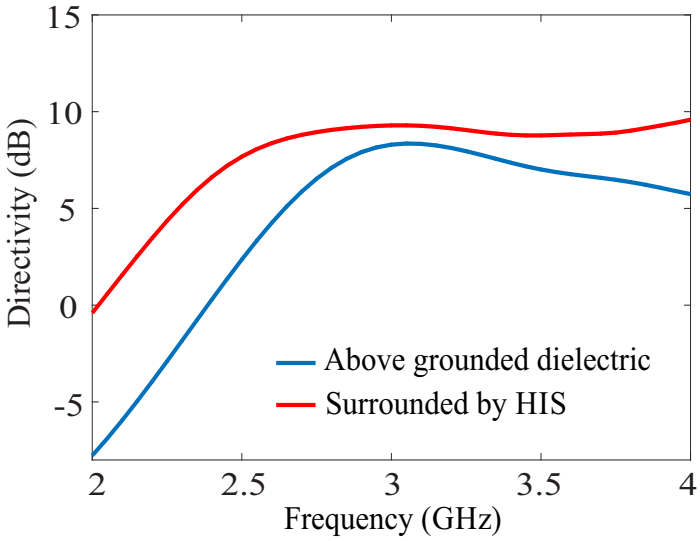

Figure 5.9: Simulated Broadside Directivity of the Loop Surrounded by Periodic Annular Patches and Above Grounded Dielectric.

To shed some light on the resonance mechanism when the annular sectors are introduced, the magnitude and the phase of the electric field inside the substrate is extracted at 3 GHz, and it is plotted in Fig. 5.10. As observed, the magnitude

distribution is diametrically symmetric with a 180° phase difference between the two sides. Consequently, a resonance is more likely to exist since the field distribution confirms the 0.25λ length in each arm surrounding the loop.

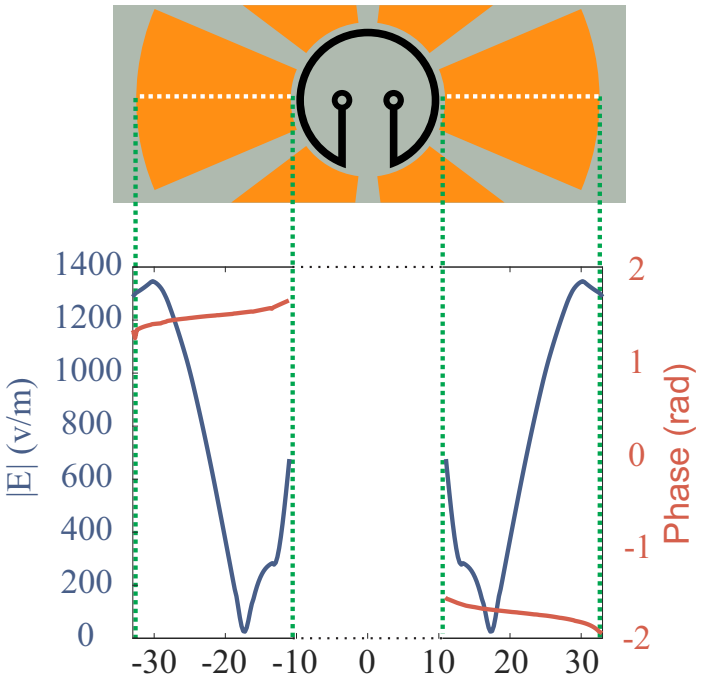

Figure 5.10: The Magnitude and Phase of the E-Field Inside the Substrate.

Besides the dispersion diagram approach, the contribution of the periodic annular sectors can also be described utilizing the reflection phase behavior. The periodic annular sectors (known also Circular High Impedance Surface (CHIS)) reflection phase can be calculated by modeling a single unit cell and applying perfect electric and magnetic boundary conditions (PEC and PMC), as illustrated in Fig. 5.11. This simulation arrangement is different from the one detailed in Chapter 3; however, both setups give same results. As observed in Fig. 5.12, the zero reflection phase for the designed unit cell occurs around 3.1 GHz. Therefore, the placement of the loop in close proximity to the CHIS will mimic the PMC reflection behavior and enhance the radiation and the impedance of the loop.

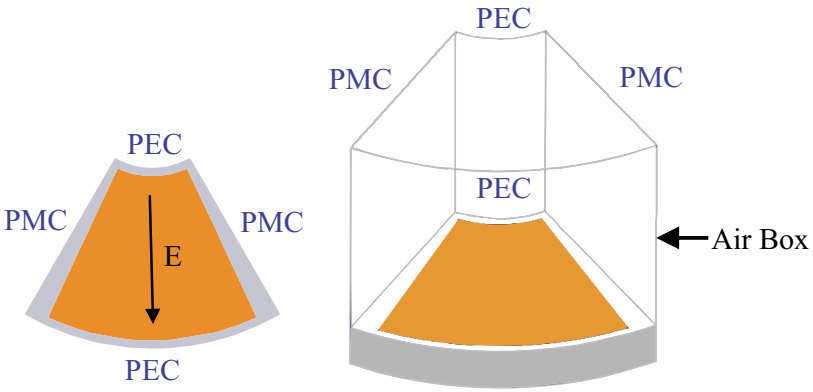

Figure 5.11: HFSS Setup to Calculate the Reflection Phase of Annular Sector Unit Cell.

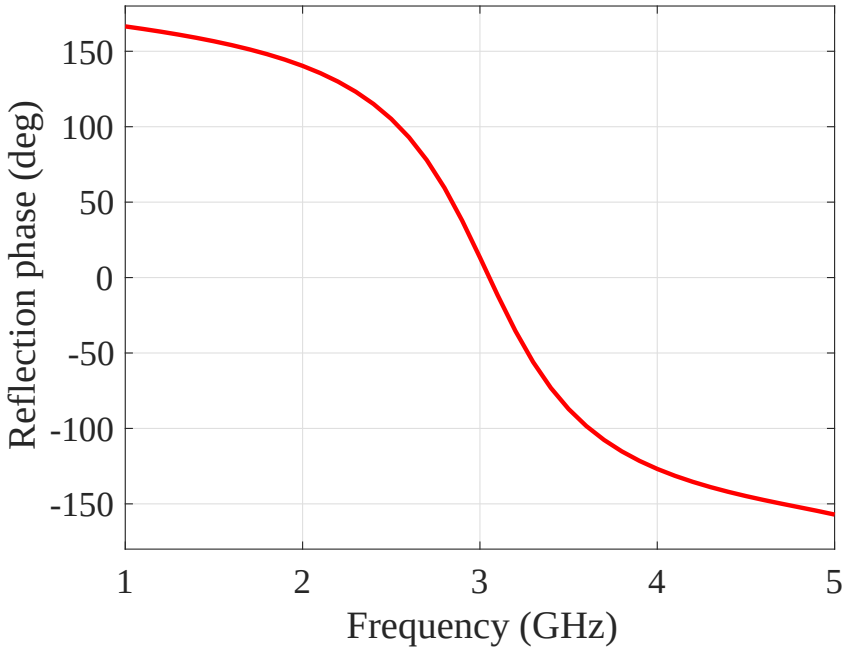

Figure 5.12: The Simulated Reflection Phase for Annular Sector Unit Cell.

5.4 Loop Antenna Above the Proposed Hybrid Ground Plane

The directivity of the previous design can be improved if the effective area increases, as in the case for the PEC ground plane discussed in Chapter 2. To elucidate more on the effective area, the directivity as a function of a dipole's length is examined [32] and plotted in Fig. 5.13. As demonstrated, the directivity increases with the dipole length, and it reaches its maximum value of 5.16 dB when the length is around 1.25λ. Therefore, if the electrical length of the periodic annular sector is extended slightly to 0.625λ on each side of the loop, then a further enhancement of the directivity is expected.

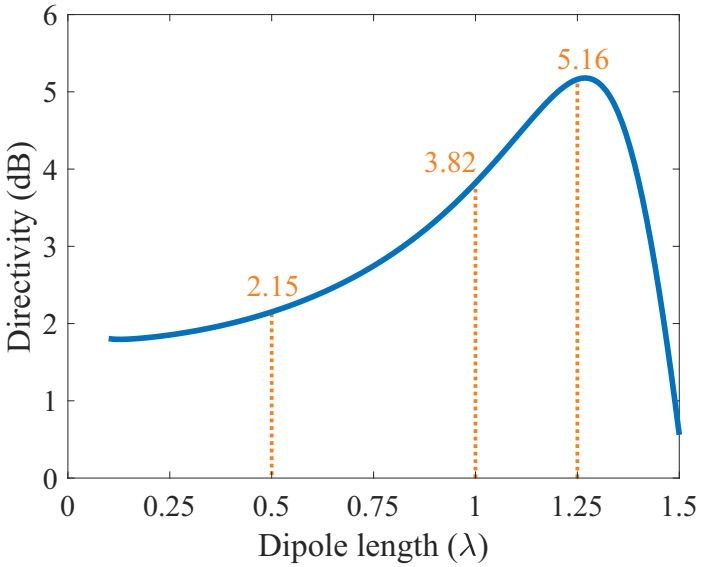

Figure 5.13: The Maximum Directivity of a Dipole as a Function of Length.

Now, to increase the electrical length of the periodic patches to an overall 360° (180° in each side), a straight forward solution is to implement another annular sector ring with same width ($w_b = w_a$) as the first annular sector (see Fig. 5.14). However, to achieve the maximum directivity, the width of the second ring has to be somewhat larger. Additionally, unlike the angle of first annular sector (p_a), it was observed that

the patch angle for the second ring (p_b) does not influence the input impedance when its electrical length (w_b) is slightly larger or equal to 90°. To illustrate this point, consider the geometry of Fig. 5.14, when two annular rings are deployed around the loop. The detailed dimensions of the proposed ground plane are summarized in Table 5.3. The angular period of the second ring ($g_b + p_b$) in the ϕ-direction is 60°. Consequently, if the angle of the annular patch $p_b = 60°$, the second ring will form a solid annular ring instead of annular sectors. With that in mind, the influence of the annular patch angle (p_b) on the input impedance and directivity is examined.

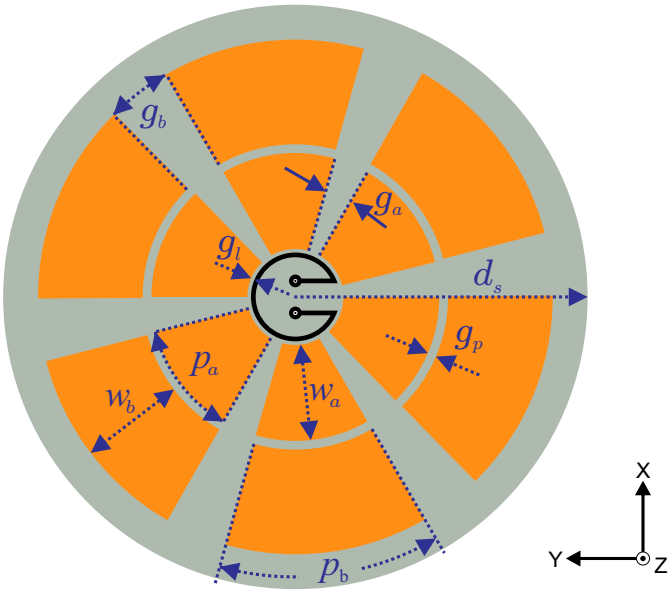

Figure 5.14: The Proposed Ground Plane with a Printed Loop Placed in the Middle.

Table 5.3: Dimensions of the Proposed Ground Plane.

Parameter	**Value**
d_s	67 mm
p_a	50^o
g_a	10^o
w_a	22 mm
g_l	1.8 mm
g_p	2 mm
w_b	24 mm

The input impedance and the broadside directivity are plotted in Fig. 5.15. As illustrated, a slight enhancement in the broadside directivity is observed; however, the input impedance is almost constant. Consequently, a solid annular ring is considered for the second ring, and the structure is deemed as a *hybrid* ground plane.

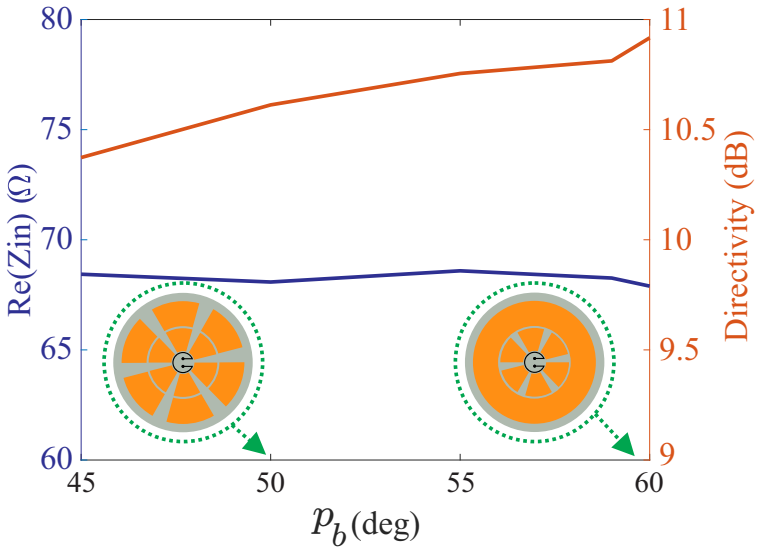

Figure 5.15: The Input Impedance and the Broadside Directivity as a Function of p_b.

Figure 5.16 displays the simulated reflection coefficient of the printed loop positioned above: a grounded dielectric, an annular sector HIS, and the hybrid ground plane. The -10 dB impedance bandwidth of the loop in the vicinity of the HIS is 2.89–3.10 GHz, which leads to a fractional bandwidth of 7%. However, when the loop positioned around the proposed hybrid ground plane, the -10 dB bandwidth falls within 2.83 and 3.22 GHz, which enhances the fractional bandwidth up to 13%. Thus, the presence of the hybrid rings does not degrade the matching bandwidth, but it rather improves the fractional bandwidth. The simulated broadside directivity of the loop element above: a grounded dielectric, an HIS, and the proposed hybrid ground plane is plotted in Fig. 5.17. The presence of the solid ring around the HIS section contributes to an increase of the directivity of the loop over the frequency range of 2.54 – 3.32 GHz, which is within the range of the matching bandwidth. At the resonant frequency (3 GHz), the directivity of the loop antenna in the vicinity of the hybrid ground plane is increased up to 11 dB, which is 3 dB higher than the directivity of the same loop when positioned above the grounded dielectric.

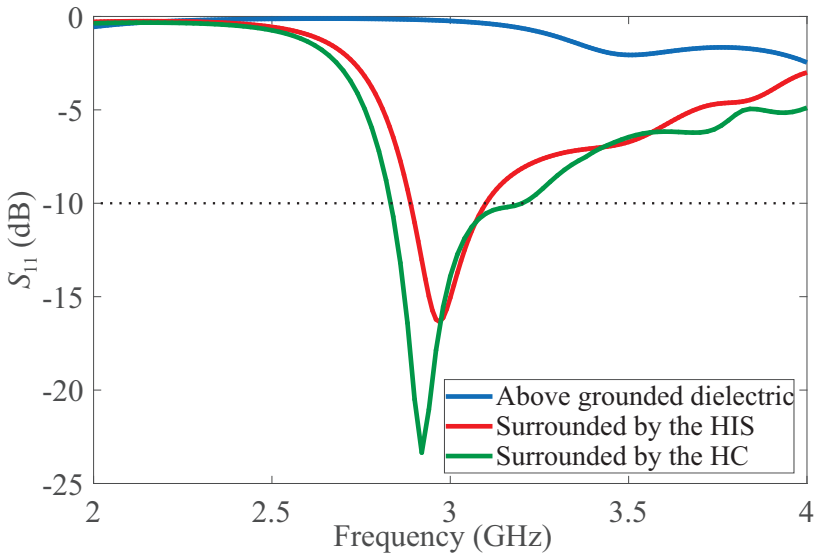

Figure 5.16: Simulated Reflection Coefficient of the Loop Antenna Above the Three Different Ground Planes.

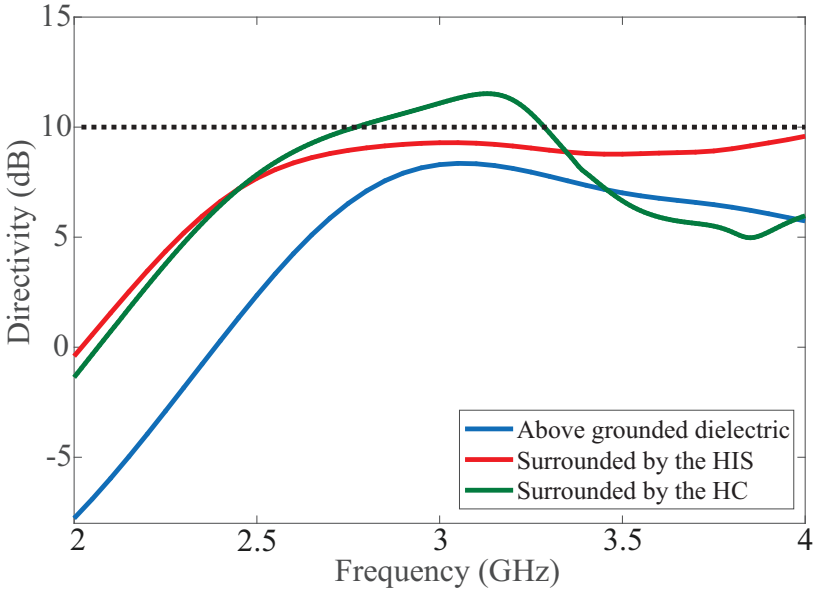

Figure 5.17: Simulated Broadside Directivity of the Loop Antenna Above the Three Different Ground Planes.

5.5 Fabrication and Measurements

To experimentally verify the proposed design, a prototype was fabricated; the configuration is shown in Fig. 5.18. As illustrated, the structure was realized exploiting two metallic layers. The top layer was devoted for the loop and the hybrid rings, while the bottom layer was used to attach the SMA connector and used as a common ground plane. A photograph of the prototype antenna is shown in Fig. 5.19. The inner conductor of the coaxial cable was soldered to one arm of the printed loop, and the outer connector of the cable was soldered to the ground plane of the substrate.

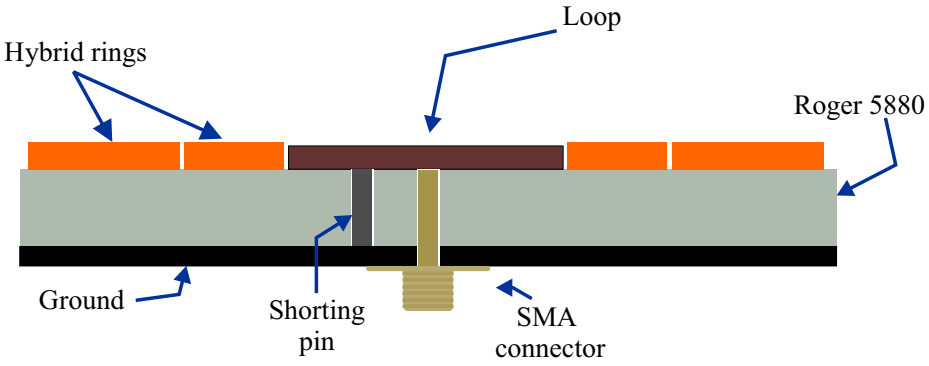

Figure 5.18: Sectional View of the Proposed Antenna.

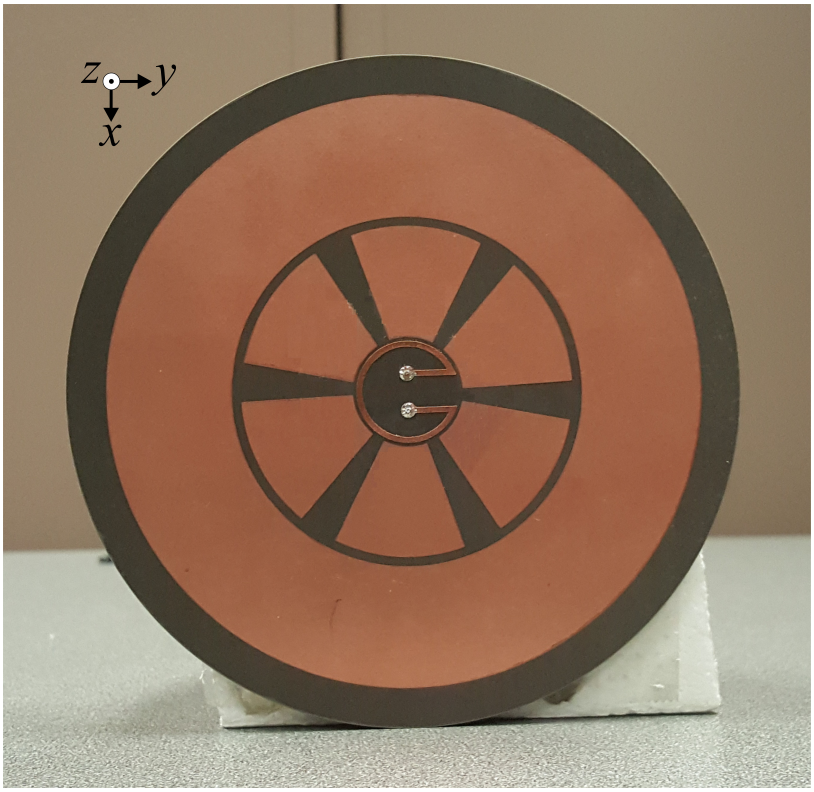

Figure 5.19: A Photograph of the Fabricated Antenna.

The reflection coefficient was measured using a Hewlett Packard 8510C network analyzer at the Arizona State University (ASU) anechoic chamber facility, as illustrated in Fig. 5.20a. Also, the gain in the broadside direction and the radiation pattern were measured, as shown in Fig. 5.20b.

(a) (b)

Figure 5.20: (a) Return Loss Measurement Setup. (b) Radiation Pattern Measurement Setup.

The measured and simulated reflection coefficients, realized gain, and radiation pattern are shown in Fig. 5.21, Fig. 5.22, and Fig. 5.23, respectively. A reflection coefficient of 24 dB at 2.9 GHz with a 13% fractional bandwidth is observed. Furthermore, a 10.5 dB stable gain is realized over the matching bandwidth. The radiation pattern at 3 GHz, shown in Fig. 5.23, is nearly symmetric with a half-power beamwidth of 65^o. An excellent agreement between the simulated and the measured results was obtained.

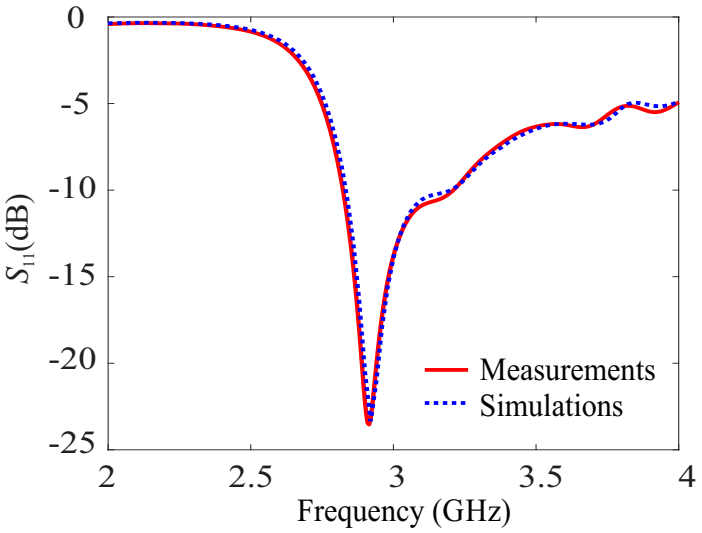

Figure 5.21: Comparison of the Measured and the Simulated Reflection Coefficients.

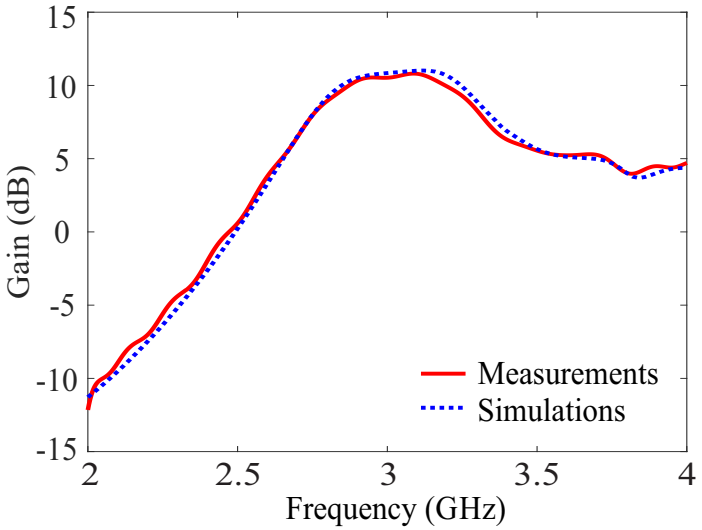

Figure 5.22: Comparison of the Measured and the Simulated Broadside Realized Gain.

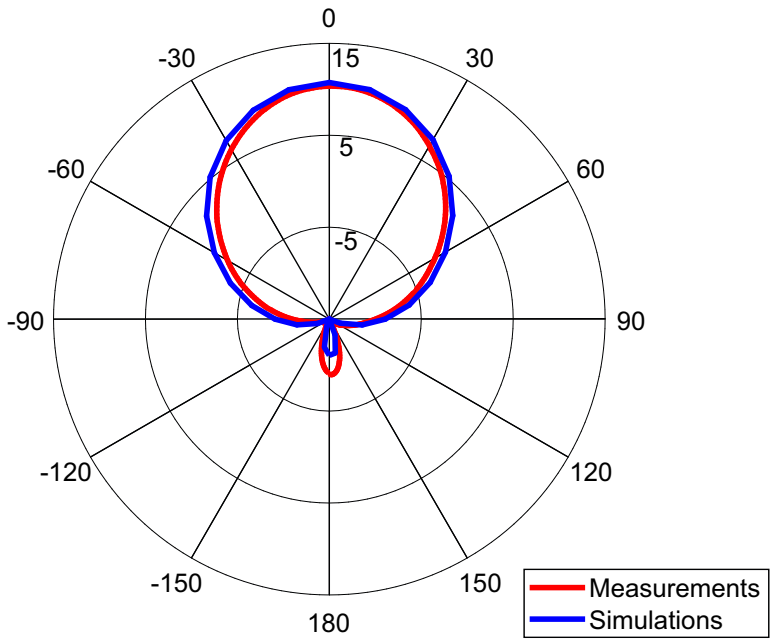

Figure 5.23: Comparison of the Measured and the Simulated Amplitude Radiation Patterns at 3 GHz.

Chapter 6

PERFORMANCE ENHANCEMENT OF SQUARE-RING ANTENNAS EXPLOITING SURFACE-WAVE METASURFACES

6.1 Introduction

Printed antennas have received great interest among a wide variety of portable communication systems, due to their distinctive features of low-profile, low cost, and ease of fabrication. Square and circular patch antennas are the most common printed antennas, and their characteristics have been thoughtfully documented [32], [37]. Square-ring antennas are similar to square patches except that the central metallic section is removed. As a consequence of this perturbation, the input resistance increases and the resonance shifts to a lower frequency, compared to their square patch counterparts [38].

Most printed antennas are known for their limited matching bandwidth (fractional bandwidth). Loading and stacking techniques have been reported to alleviate the narrow matching bandwidth of ring antennas [38], [39]. However, such approaches increase the height profile (in case of stacked technique) or they just lead to a small bandwidth improvement (2% improvement in the loading approach). Consequently, metasurfaces have been utilized in the vicinity of printed antennas to enhance the matching performance [15], [29].

The loading of the periodic metallic patches to dielectric covered ground plane alters favorably the characteristic of the ground plane, and it ameliorates the matching bandwidth of adjacent radiating elements. The frequency, where the reflected field at surface of periodic patches undergoes zero degree shift, is termed as High Impedance

Surface (HIS) resonance [7]. In addition to the HIS resonance, the recurring patches modify the characteristics of the surface waves and can further widen the bandwidth [27, 28].

In this chapter, the radiation performance of a square-ring antenna, in the vicinity of a metasurface, is considered and investigated. Due to the finite physical size of the metasurface, surface wave resonances are excited to broaden the matching bandwidth of the adjacent radiating element. Most reported surface wave designs have been devoted to radiating elements above or below square metasurfaces. Unlike square-patch metasurfaces, rectangular patches are considered in this design as they can provide independent control over the propagation of surface waves along the principal planes. To devise an efficient design of launching surface waves with broadside radiation, various configurations (radiating element within, above, and below metasurfaces) are discussed in Section 6.3, and the radiation characteristics are investigated. Among the different designs, a radiating element embedded within metasurfaces provides a superior performance compared to the other two configurations. To validate the proposed design, a prototype was fabricated and measured; an excellent agreement was achieved between simulated and measured data.

6.2 Surface Waves and HIS Resonances

Recurring rectangular patches are placed on a grounded dielectric to model the metasurface (MS) structure. Three unit cell layouts are investigated and labeled as A, B, and C, and are displayed in Fig. 6.1a. While the three unit cells have the same patch size and periodicity (p_x and p_y), they differ with respect to the superstrate layer. Units A and B have a metallic patch either on the top or bottom layer of the superstrate, while the superstrate layer is omitted in unit C, and the patch is printed on the top layer of the substrate. The substrate and superstrate are modeled

on Rogers RT/Duroid-5880 dielectric ($\varepsilon_r = 2.2,\ \tan\delta = 0.0009$) with thickness of h_1 = 5.08 mm, and h_2 = 1 mm. The details of the other parameters are specified in the caption of Fig. 6.1.

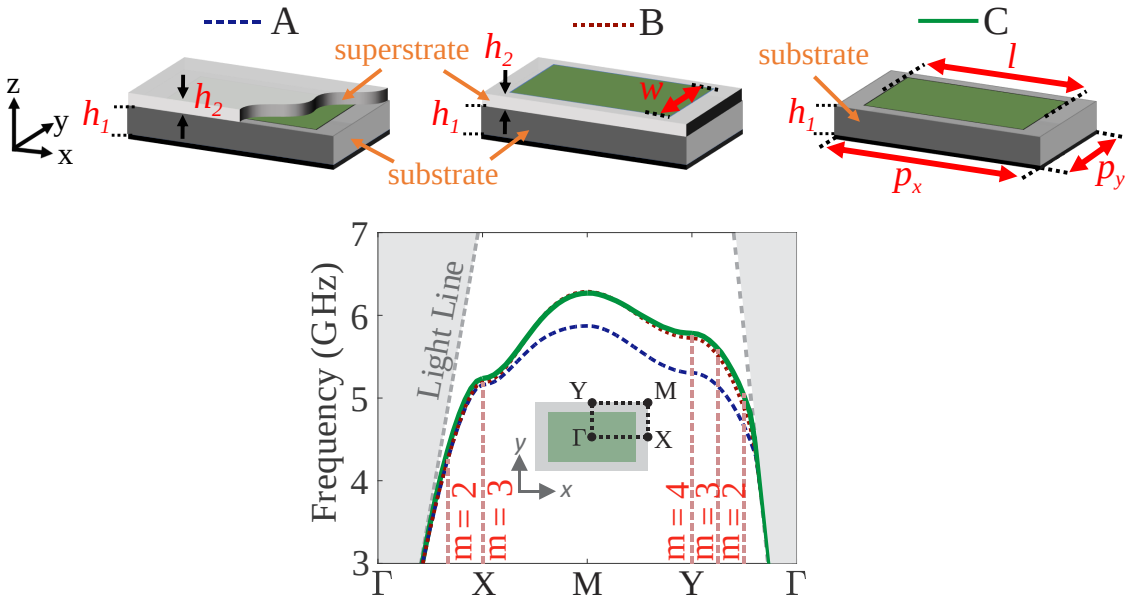

(a) Dispersion diagram

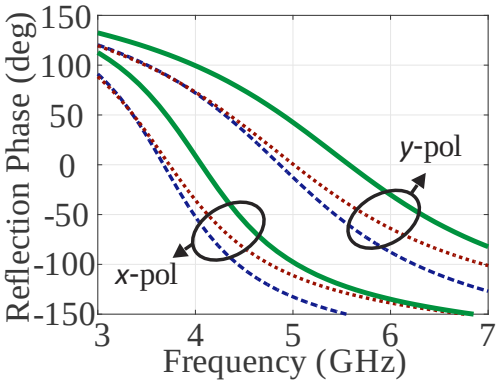

(b) Reflection phase

Figure 6.1: (a) Dispersion Diagram and (b) Reflection Phase of Various Unit Layouts. The Design Parameters (in mm): $h_1 = 5.08$, $h_2 = 1$, $p_x = 20.5$, $p_y = 12.5$, $l = 16$, $w = 9$.

To analyze the three unit cells, a full-wave solver (HFSS) is used to obtain the reflection behavior and the dispersion diagram, as depicted in Fig. 6.1. The reflection phase for normal illumination is extracted at the top face of each unit cell exploiting a Floquet port. The dispersion diagram, on the other hand, is obtained utilizing the eigenmode solver in HFSS after applying the master-slave boundary conditions. Only the dominant mode (TM mode) is considered in the dispersion analysis as TE does not support slow-wave propagation in the frequency range of interest. The first observation is that all unit cells have a similar dispersion behavior as the surface waves travel along the x-direction ($\Gamma \rightarrow$ X). However, unit A exhibits a different behavior as the wave propagates in the transverse direction ($\Gamma \rightarrow$ Y). The observed discrepancy can be attributed to the different field confinements, which is analogous to the effective dielectric constant in strip and microstrip lines. A very slight dispersion deviation is found between units B and C due to the superstrate thickness being small. When the metasurface structure is truncated, slow wave resonances can be excited; these resonances vary with the size of the MS, and they can be determined by [27]

$$\beta_{SW_{(x,\,y)}} L_{(x,\,y)} = m\pi \quad m = 1, 2, ... \tag{6.1}$$

$$L_{(x,\,y)} = P_{(x,\,y)}\, N_{(x,\,y)} \tag{6.2}$$

where $\beta_{SW_{(x,\,y)}}$ is the propagation constant of the surface wave, $P_{(x,\,y)}$ represents the cell periodicity, and $N_{(x,\,y)}$ is the number of unit cells along x- or y-directions. By drawing a vertical line representing the solution of (6.1) on the dispersion diagram, the resonances of the surface waves along x- and y-directions can be extracted by the intersection between the TM mode curve and the vertical line. Since a square-ring antenna is utilized to operate in the dominant mode (TM_{11}^{x}), TM surface waves are more likely to be excited as slow-wave propagation is supported around the ring

element's resonance. The solution of (6.1) for a 3 x 4 MS structure, where $N_x = 3$ and $N_y = 4$, is shown in Fig. 6.1a. Next to each vertical line, the value of m in (6.1) is labeled. Only $m \geq 2$ are considered as they are located in the slow-waves region, which can be efficiently excited. For all unit cell layouts, the resonances of surface waves along the x-direction (f_{SW-x}) and y-direction (f_{SW-y}) are tabulated in Table 6.1; in addition to the surface-wave resonances, the HIS resonances (f_{HIS-x}, f_{HIS-y}) along x and y axes are also listed. The HIS resonances represent the in-phase reflection, zero-degree reflection phase, of the different unit layouts, as displayed in Fig. 6.1b. The f_{HIS-x} should be in the proximity of the ring-antenna resonance (TM_{11}^{x}) to surpass the radiating element resonance [1].

Table 6.1: Surface Wave and HIS Resonances

Unit Cell	**A**	**B**	**C**
f_{SW-x} (GHz)	4.2, 5.1	4.2, 5.1	4.3, 5.2
f_{SW-y} (GHz)	4.6, 5.1, 5.3	4.8, 5.5, 5.7	5.0, 5.6, 5.8
f_{HIS-x} (GHz)	3.7	3.7	4.1
f_{HIS-y} (GHz)	4.8	5.0	5.5

6.3 Ring Antenna and Metasurfaces

Although multiple slow-wave resonances were defined in the previous section, they can be efficiently excited if a TM source is utilized. Hence, a square-ring antenna is a good candidate to excite additional surface-wave resonances, besides its dominant mode resonance. To investigate an efficient design for launching surface waves with a square-ring radiator, four configurations are considered, as illustrated in Fig. 6.2. Three of the illustrated configurations have a square ring (radiator) in the vicinity of

the MS; namely, radiator above MS (RAMS), radiator below MS (RBMS), and radiator within MS (RWMS). For the sake of visualization, a small portion of the RAMS and RBMS was removed in Fig. 6.2. The defined HIS and surface wave resonances for units A, B, and C correspond to RAMS, RBMS and RWMS, respectively. To highlight the effect of the HIS resonance and surface-wave excitation, a conventional radiator (CR) is considered in this analysis. The dimensions are listed in the caption of Fig. 6.2. In all four configurations, the ring antenna is fed with a 50-ohm coaxial probe along the x-axis to excite the TM_{11}^{x} mode [38]. The probe has a diameter $d_i = 1.27$ mm, and it is fed at $(f_x,\ f_y) = (9\text{ mm}, 0)$.

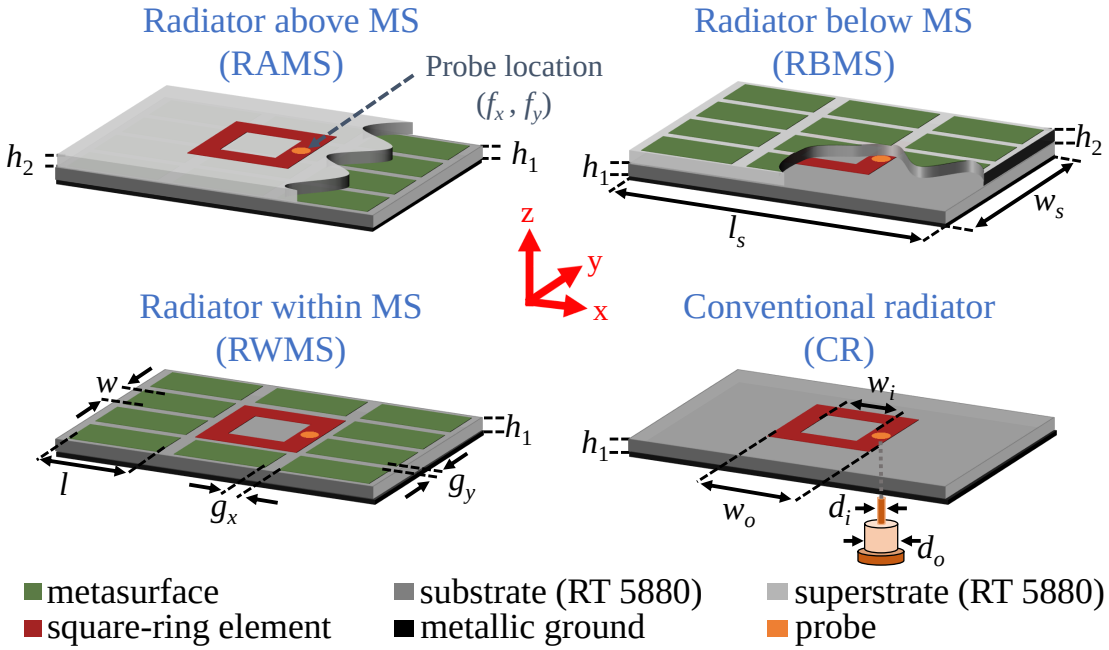

Figure 6.2: Different Configurations of the Ring Element in Vicinity of the MS. The Design Parameters are: $h_1 = 5.08$ mm, $h_2 = 1$ mm, $l = 16$ mm, $w = 9$ mm, $g_x = 4.5$ mm, $g_y = 3.5$ mm, $w_i = 11$ mm, $w_o = 20$ mm, $l_s = 61.5$ mm, $w_s = 50$ mm. The Coaxial Dielectric is Teflon ($\varepsilon_r = 2.08$) with a Diameter (d_o) of 4.1 mm.

The resonances of the radiator and the surface waves can be identified by examining the frequencies at which the real part of the input impedance attains its maximum value [27], as depicted in Fig. 6.3a. For the CR configuration, only one resonance exists at 3.6 GHz, which is referred to as radiator resonance (f_{rad}). The f_{rad} agrees with the calculated resonance of the ring antenna reported in [37]. When the MS is introduced, the f_{rad} shifts slightly to a lower frequency due the coupling between the radiator and the MS. In addition to f_{rad}, surface-wave resonances (f_{sw}s) begin to contribute for the RAMS, RBMS and RWMS. For the RAMS, the f_{sw}s are 4.3, 4.9, 5.1, and 5.5 GHz, which are found to be close to the extracted resonances of unit A along x and y directions.

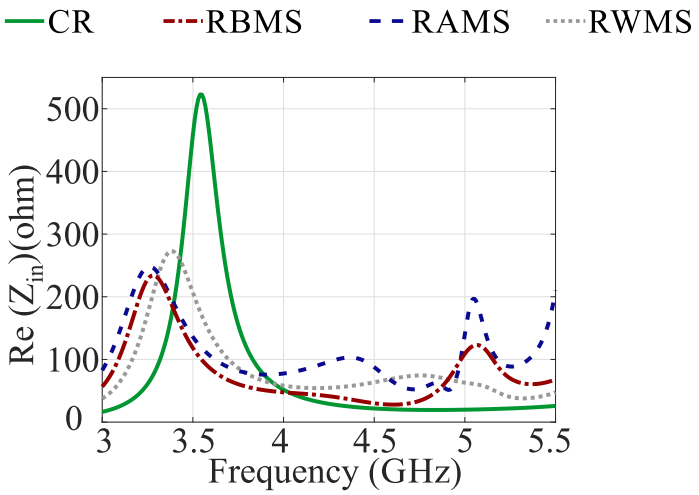

(a) Input Resistance

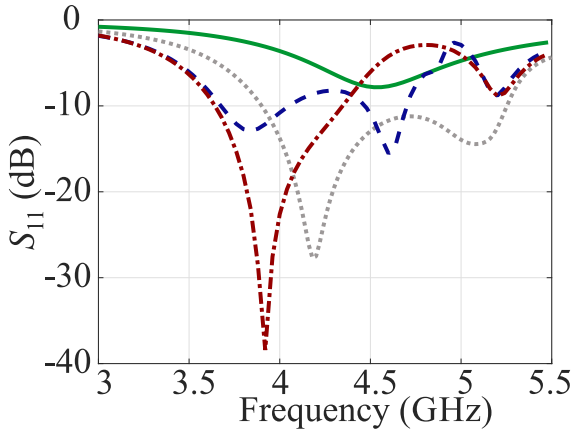

(b) Reflection Coefficient

Figure 6.3: (a) Real Part of Input Impedance, and (b) Reflection Coefficient for the Different Designs Illustrated in Fig.6.2.

For the RBMS design, resonances at 4.3 and 5.1 GHz are observed, and they relatively agree with the defined resonances along the x-axis of unit B. On the other hand, the f_{sw}s for the RWMS are excited at 4.6 and 5.1 GHz. The 4.6 GHz resonance deviates somewhat from the resonance of unit C (f_{SW-x}) listed in Table 1. This difference is attributed to the perturbation in the metasurface periodicity as a result of embedding the radiator.

To further investigate the performance of the different designs, the reflection coefficient (S_{11}) for a 50-ohm source are displayed in Fig. 6.3b. As seen, the conventional radiator (CR) has a single resonance at 4.6 GHz with poor matching. However, when the ring radiator is placed in close proximity to the MS, besides the excitation of surface-waves, the matching of radiator's resonance is improved with slight shift to a lower frequency. For the RBMS and RWMS configurations, the resonances of the radiator and the surface wave are closely-spaced, which results in fractional bandwidths ($S_{11} \leq -10\,\mathrm{dB}$) of 17%, and 31%, respectively. However, for the RAMS with a small matching bandwidth, the resonances are far apart. From the aforementioned results, the embedded square ring provides an exceptional matching bandwidth compared to the other designs.

To emphasize the impact of the excited surface waves on the radiation performance, the broadside realized gain, with all losses taken into accounts, is examined for the various structures and plotted in Fig. 6.4. At lower frequencies, the broadside realized gain is higher in the vicinity of the MS compared to the CR; however, for the RAMS and RBMS configurations, the realized gain begins to fluctuate as the frequency increases. The two designs follow similar broadside behavior due to the comparable excited surface waves, which was not evident in the result of the input impedance. The perceived unstable broadside radiation is owing to the excitation of the surface waves along both x and y directions, causing non-broadside radiation. To justify this observation, the realized gain pattern for the RAMS design at 4.9 GHz is inset in Fig. 6.4 a. As illustrated, non-broadside radiation is observed, and both components (θ and ϕ) constructively radiate at 60°. To further expand the analysis, the normalized magnitude of E_z, inside the substrate ($h_1/2$), at 4.9 GHz is investigated and plotted in Fig. 6.4b. The plotted field is calculated along the y-axis on a line, dotted white line in Fig. 6.4b, positioned at x = -8 mm from the

center of the ring. For RAMS and RBMS, the plotted field is maximum near the edges of the substrate resulting in destructive interference in the broadside direction. While for CR and RWMS, the field is maximum at the center, and it decays as it reaches the edge leading to a broadside radiation. Consequently, when the radiator is placed within the MS (RWMS), the realized gain is constantly maintained above 8 dBi from 3.8 to 5.2 GHz. This interesting radiation behavior, observed in RWMS, is due to the excitation of the radiator mode accompanied by a couple of surface waves along the x-direction. The implementation of rectangular-patches MS, along with the disturbance of periodicity, contribute to the outstanding matching and radiation performance observed for the RWMS.

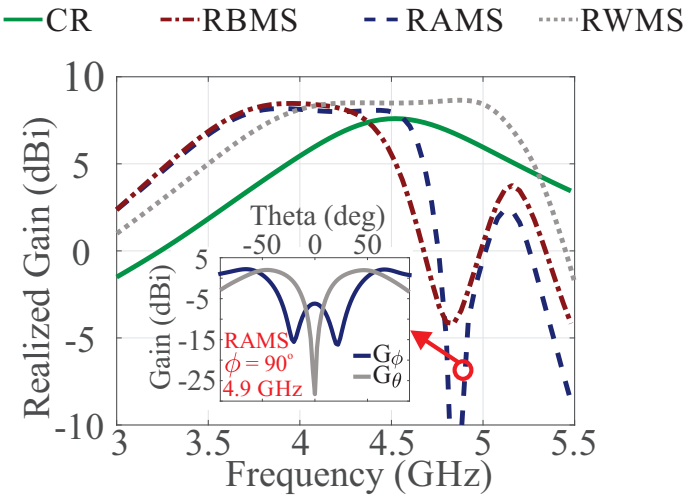

(a) Realized Gain

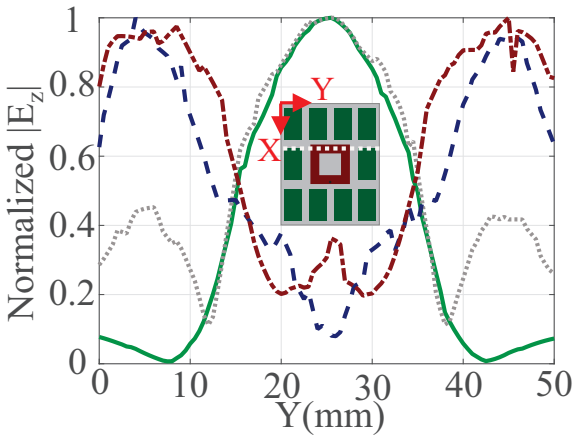

(b) Normalized Magnitude of E_z

Figure 6.4: (a) Broadside Realized Gain of the Various Configurations, with Inset Showing the Radiation Pattern for RAMS at 4.9 GHz. (b) Normalized Magnitude of E_z Inside the Substrate, with Inset Displaying the Position (Dotted White Line) of the Extracted Field.

6.4 Impact of Surface-Wave Resonances on Performance of RWMS

The RWMS design provides the most favorable performance compared to the other models; therefore, only the RWMS design is examined in this section. The length and width of the periodic patches are varied to demonstrate their impact on the excited surface-wave. The periodicity of the patches (p_x and p_y) is maintained fixed at 20.5 mm and 12.5 mm, respectively. Only one parameter is varied at a given time while all other parameters are held constant, as detailed in the caption of Fig. 6.2. As illustrated in Fig. 6.5, varying the length impacts both resonances; the radiator and surface waves.

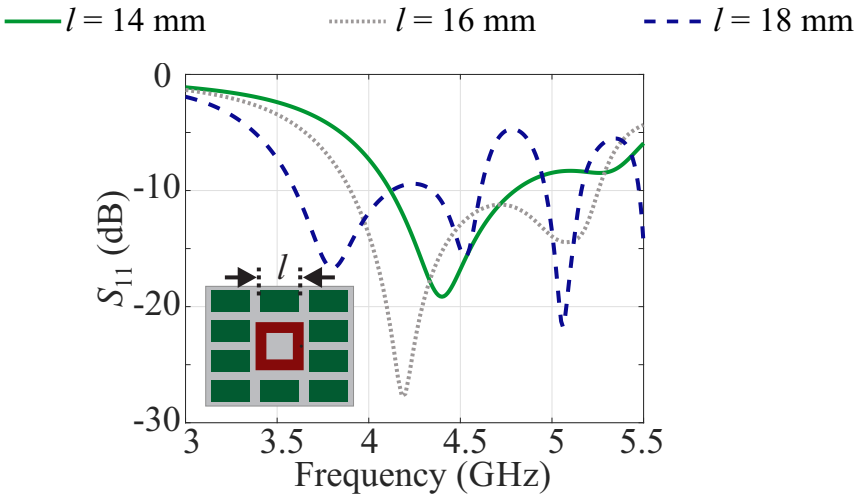

(a) Reflection coefficient

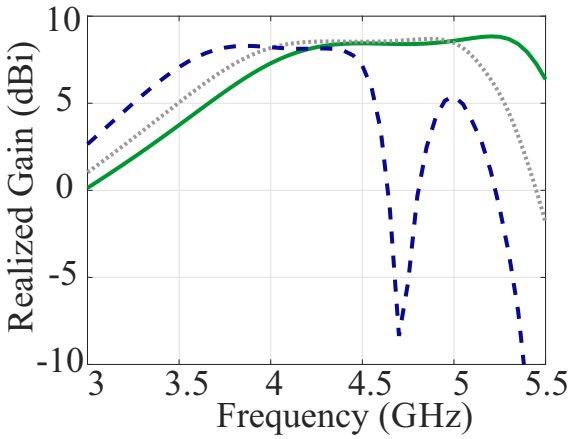

(b) Broadside realized gain

Figure 6.5: Impact of Varying the Length of the Periodic Patches on Reflection Coefficient (a) and Broadside Realized Gain (b).

The shift of the resonances is expected since the length (l) is along the direction of the excited surface waves (f_{SW-x}), and along the HIS resonances (f_{HIS-x}). An interesting phenomenon in the broadside realized gain is observed when $l = 18$ mm or ($2w$). It exhibits a similar radiation behavior as the RAMS and RBMS, which is depicted in Fig. 6.4; this is attributed in that they share similar dispersion behavior, which results in comparable resonances of the excited surface waves. The influence on

the performance by varying the width of the periodic patches (w) is also examined, as illustrated in Fig. 6.6. For the RWMS design, the width is along the transverse direction of the excited surface waves; therefore, altering the width has a negligible influence on the dispersion behavior along the direction of the excited surface waves [40]. Consequently, the width has small impact on the reflection coefficient and realized gain.

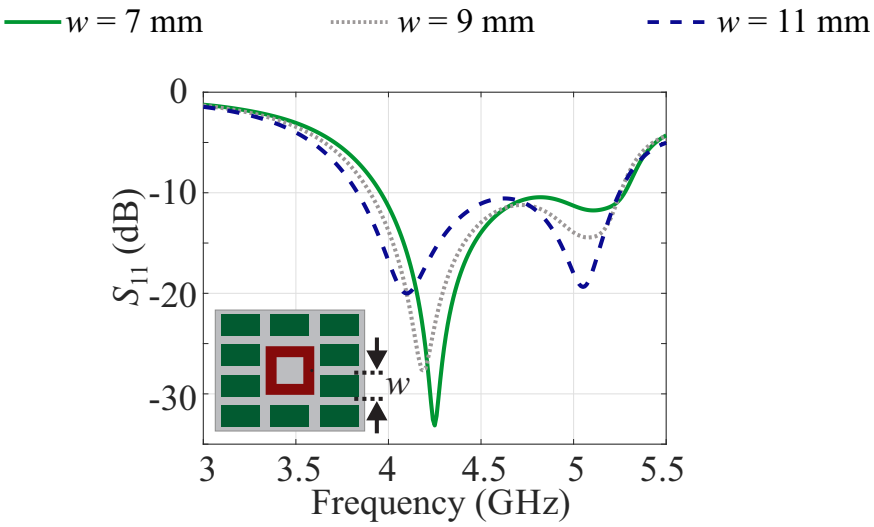

(a) Reflection Coefficient

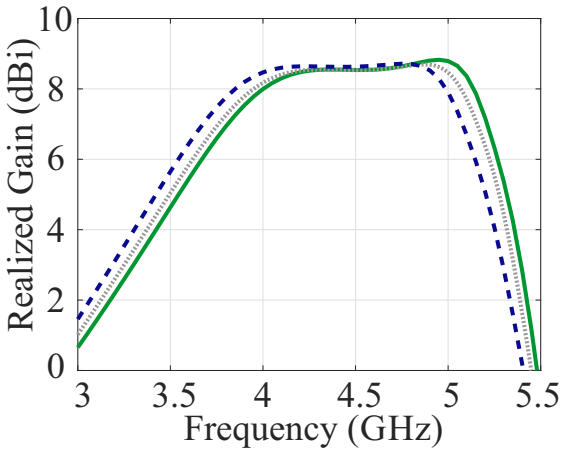

(b) Broadside Realized Gain

Figure 6.6: Impact of Sweeping the Width of the Periodic Patches on the Reflection Coefficient (a) and Broadside Realized Gain (b).

For surface-wave antennas, the size of the substrate impacts the radiation performance, as the surface waves diffract from the edges causing constructive/destructive interference [33]. Therefore, the influence of the substrate size is examined, as depicted in Fig. 6.7. As observed, the width of the substrate does not disturb the matching bandwidth, but it does increase the realized gain at higher frequencies.

However, the length of the substrate alters both the matching bandwidth and the realized gain. The change in resonance is owing to (6.1), as the resonances of surface wave strongly depends on the length of the cavity. By increasing the length of structures, the resonances shift to lower frequencies, and they move closer to each other [6]. A 3-dB gain enhancement is observed at 4.9 GHz when the size of the substrate is 75 x 75 mm. The gain increase is attributed to (in addition to the constructively enhanced diffracted surface waves) the superimposed surface wave resonances, as they are closely spaced when the cavity length increases [6].

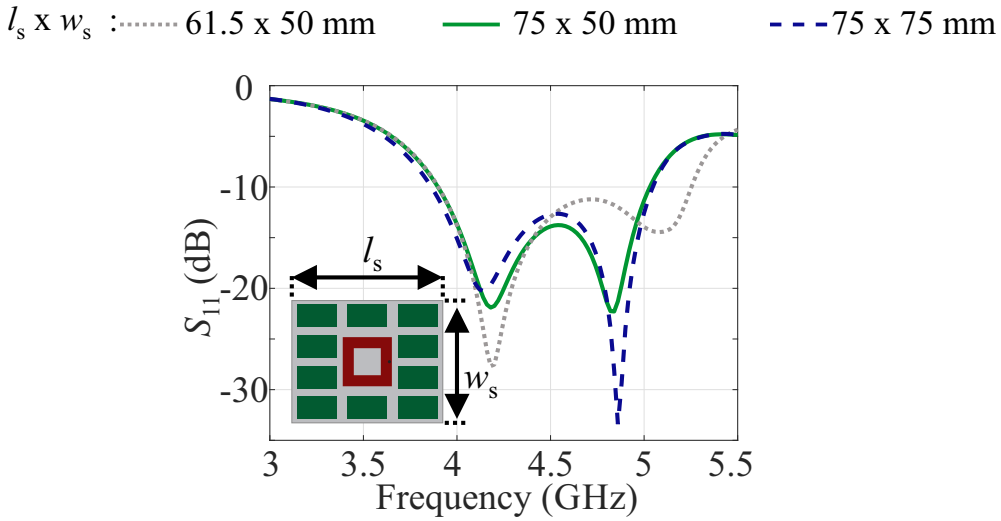

(a) Reflection Coefficient

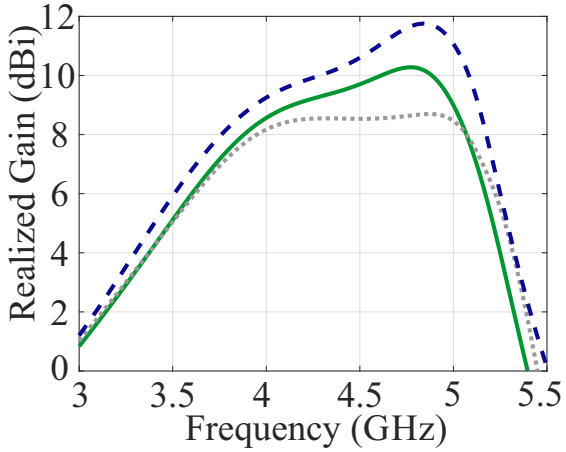

(b) Broadside Realized Gain

Figure 6.7: Impact of Varying the Substrate Size on Reflection Coefficient (a) and Broadside Realized Gain (b).

6.5 Fabrication and Measurements

To verify the simulated results related to the RWMS design, a prototype was fabricated and measured, as shown in Fig. 6.8. The substrate is Rogers RT/Duroid-5880 ($\varepsilon_r = 2.2$, $\tan\delta = 0.0009$) with thickness of 5.08 mm, and size of 75 x 75 mm.

The other parameters of the RWMS are specified in the caption of Fig. 6.2. A flange mount SMA connector was used to feed the antenna. The measured and simulated

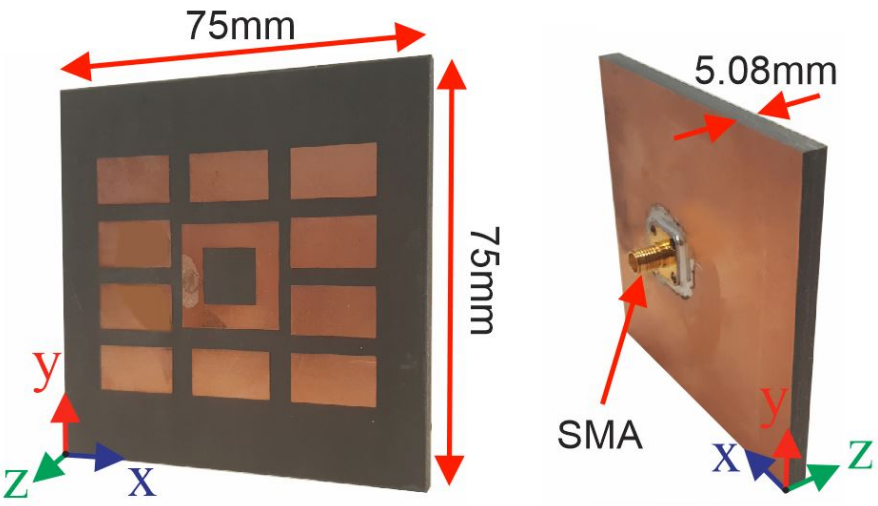

Figure 6.8: Different Views of the Fabricated Prototype of the RWMS Design.

results of reflection coefficient and broadside realized gain are displayed in Fig. 6.9. An excellent agreement is observed between the measured and simulated data. The fractional bandwidth ($S_{11} \leqslant -10$) is 27% from 3.8 to 5 GHz. The total radiation patterns at two different cuts ($\phi = 0^\circ$ and 90°) for 4 GHz and 5 GHz are illustrated in Fig. 6.10. Nearly symmetrical radiation patterns are viewed with excellent agreement between the simulated and measured data.

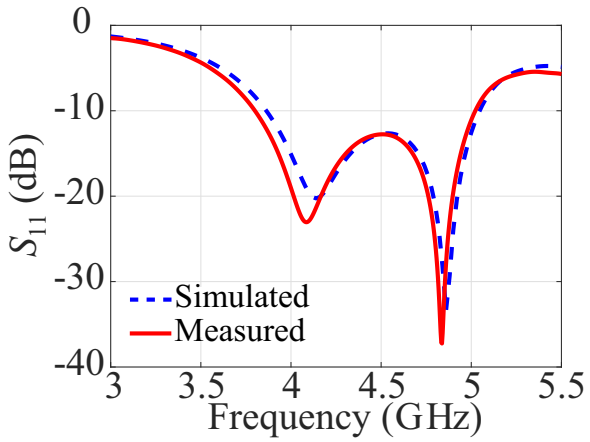

(a) Reflection Coefficient

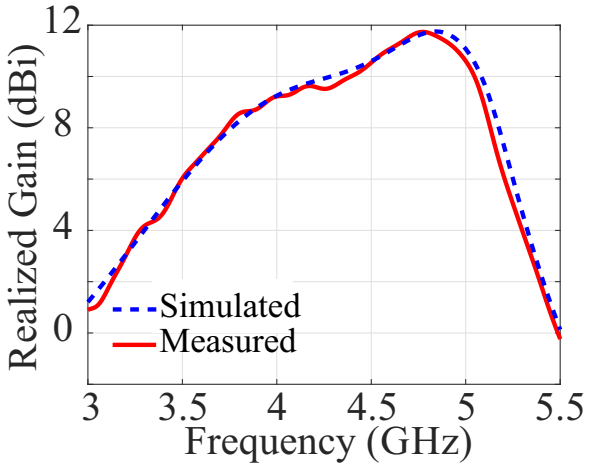

(b) Broadside Realized Gain

Figure 6.9: Comparison Between Simulated and Measured Data. (a) Reflection Coefficient. (b) Broadside Realized Gain ($\theta = 0°$, $\phi = 0°$).

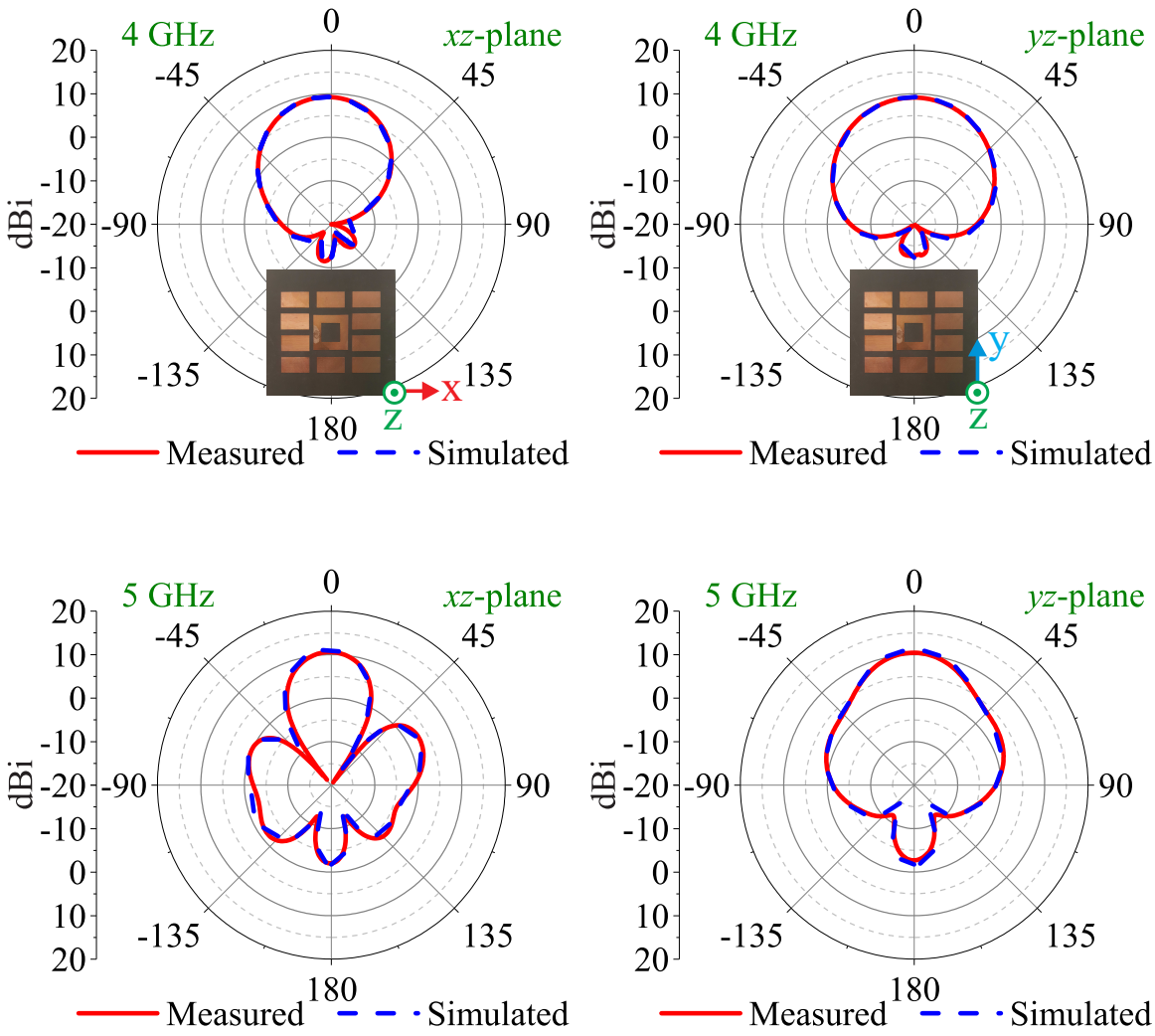

Figure 6.10: Comparison Between Simulated and Measured Radiation Patterns of the RWMS Design at Two Frequencies (4 and 5 GHz) at $xz-$ and $yz-$Planes.

Chapter 7

LINEAR AND CIRCULAR POLARIZED METASURFACES ANTENNA ARRAY UTILIZING SQUARE-RING ELEMENT

7.1 Introduction

Metasurfaces have advanced antenna technology and have promoted a variety of antenna features. One of the interesting metasurface features is the capability of supporting and guiding surface waves. The excitation of surface waves, if they are excited properly, enhances the overall antenna performance [26, 27]. Consequently, several printed antennas have been reported, and the influence of the surface waves excitation has been examined. Monopole-like radiation has been achieved using a circular patch in the vicinity of uniform square metasurfaces [28] and non-uniform metasurfaces [41]. Similarly, surface waves have been excited utilizing a square ring element surrounded by anisotropic metasurfaces yielding broadside radiation [30]. Another broadside radiation design has been realized by placing a diamond-shape patch element in the vicinity of square-patches metasurfaces [42].

To further promote the radiation performance, studies have expanded the analysis to include multiple radiators in the vicinity of metasurfaces to form what is referred to *array metasurface antennas* [42, 43]. The reported designs require a specific spacing between the metasurface supercell to maintain and realize the high broadside gain. This spacing degrades the aperture efficiency and reduces the maximum attained gain. *As it will be demonstrated in this chapter, the spacings between the metasurface supercell can be reduced without disturbing the functionality of the design.*

The aforementioned designs are linearly polarized, and they have a wide range of potential low-profile applications. The superiority of circular polarization over linear polarization inspired researchers to investigate the possibility of designing circularly polarized metasurface antennas. The advantages of circular polarization include alleviation of polarization mismatch losses and better stability for the received signal [6]. The circular polarization can be realized by placing a linear-to-circular metasurface superstrate above radiating elements [44]. This approach requires a certain spacing between the radiating element and the metasurface superstrate, which disturbs the overall height-profile. The second approach is to excite surface waves in two orthogonal planes that share the same magnitude and 90° phase difference [45–47]. A truncated square patch element positioned in close proximity to square-patch metasurfaces resulted in 7 dB peak gain, a fractional bandwidth of 45.6%, and 3-dB AR bandwidth of 23.4% [45]. Another design implemented planar slot to excite rectangular-patches metasurfaces and led to an average gain of 5.8 dB, an impedance bandwidth of 33.7%, and a 3-dB AR bandwidth of 16.5% [46]. The low peak gain observed in the above-mentioned designs is enhanced up to 12 dB by forming a 2x2 array of truncated patch elements positioned below square-patches metasurface [47]. This gain can be further promoted by exciting surface waves along with the active element's fundamental mode, which will be demonstrated in this work.

In this chapter, an array of multiple square ring elements embedded within a metasurface is presented. With different array configurations, linear and circular polarizations are proposed. For the linear polarization, a 1x4 square ring elements are printed on the same plane with periodic patches. With a spacing of $0.56\lambda_o$ between the elements, a high realized gain with high aperture efficiency is attained. For the circular polarization, a 2x2 structure is considered with a spacing of $0.85\lambda_o$ between the ring elements. After analyzing the port isolations between the ports, a simple

parallel feeding network is designed and incorporated with the structures. Due to the similar characteristic of the two arrays, only the 2x2 circular polarized structure is experimentally validated.

7.2 1x4 Linearly Polarized Metasurface Array

The array designs considered in this letter are based on the structure proposed in [4]. The radiator within the metasurface (RWMS) is extended in this study due to its wide matching bandwidth and stable unidirectional radiation. For brevity, this chapter does not cover the analysis and the design of RWMS; the interested readers can refer to [30] to develop an understanding of the RWMS design. A one-dimensional (1D) array is designed as illustrated in Fig. 7.1a. The array has four square-ring elements utilized to launch surface waves in addition to their resonances. The interelement spacing $s = 37.5$ mm, which is about $0.56\lambda_o$ at 4.5 GHz. The substrate is Rogers RT/Duroid-5880 ($\varepsilon_r = 2.2$, $\tan\delta = 0.0009$) with a thickness $h = 5.08$ mm. The ring elements and the metasurface patches are printed on the top face of a single substrate whose length $l_s = 191.5$ mm and width $w_s = 62$ mm. The remaining parameters are detailed in the caption of Fig. 7.1. Since the design relies on the excitation of surface waves, it is interesting to shed some light on the isolation between the ports. Therefore, the ring elements are individually fed with four coaxial probes, as presented in Fig. 7.1a. For optimum broadside radiation, all elements are excited with the same magnitude and phase.

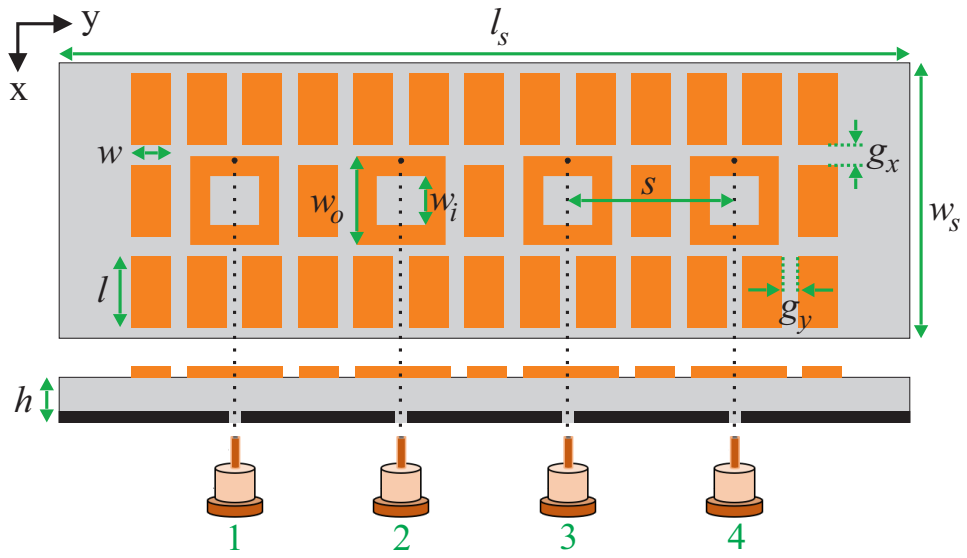

(a) RWMS with coaxial ports

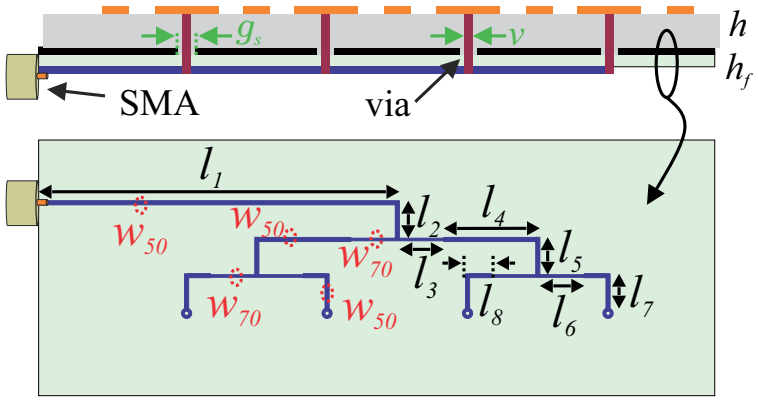

(b) RWMS with feed network

Figure 7.1: 1x4 Square Ring Elements Embedded Within Metasurface and Excited with (a) Four Coaxial Probes and (b) Feed Network. The RWMS Parameters are: w_i = 10 mm, w_o =20 mm, l = 16 mm, w= 9 mm, g_x = 4.5 mm, and g_y = 3.5 mm. The Feed Network Parameters are: l_1 = 96.3 mm, l_2 = 10 mm, l_3 = 11.85 mm, l_4 = 25.65 mm, l_5 = 10 mm, l_6 = 11.85 mm, l_7 = 9.29 mm, l_8 = 6.9 mm, g_s = 2.74 mm, v = 1.143 mm, w_{50}= 1.1 mm, and w_{70}= 0.7 mm.

The reflection coefficients and the mutual coupling between the coaxial ports are simulated and presented in Fig. 7.2. The -10 dB reflection coefficient for all ports (dotted red line) is about 28% from 3.9 – 5.2 GHz, which is the same bandwidth attained with a single RWMS [30]. The isolation between two adjacent elements (e.g. S_{12}) is low at lower frequencies and reaches up to -10 dB at 5.2 GHz. This is attributed to the surface waves along the y-axis, which begin to resonate above 5 GHz [30], and they disturb both the port isolation and the broadside radiation. The isolation can be improved by increasing the spacing between the square-ring elements; however, this approach will introduce undesired sidelobes. Once the port isolations are examined, a parallel feeding network, presented in Fig. 7.1b, is designed for practical implementation of the RWMS array. The feeding network is also designed on Rogers RT/Duroid-5880 substrate whose thickness $h_f = 0.38$ mm. The feed is stacked below the 1x4 array, and the outputs of the feed are coupled to the ring elements by means of plated through vias. The dimensions of the feed network are detailed in the caption of the figure. For comparison purposes, the S_{11} is investigated for the feed network when it is connected to:

- RWMS array.
- Conventional square element array (in the absence of metasurface).

As illustrated in Fig. 7.2, when the feed is connected to the RWMS array, the -10 dB fractional bandwidth is comparable to that obtained with coaxial ports; however, poor matching is attained when the feed is integrated with a conventional 1x4 square ring array.

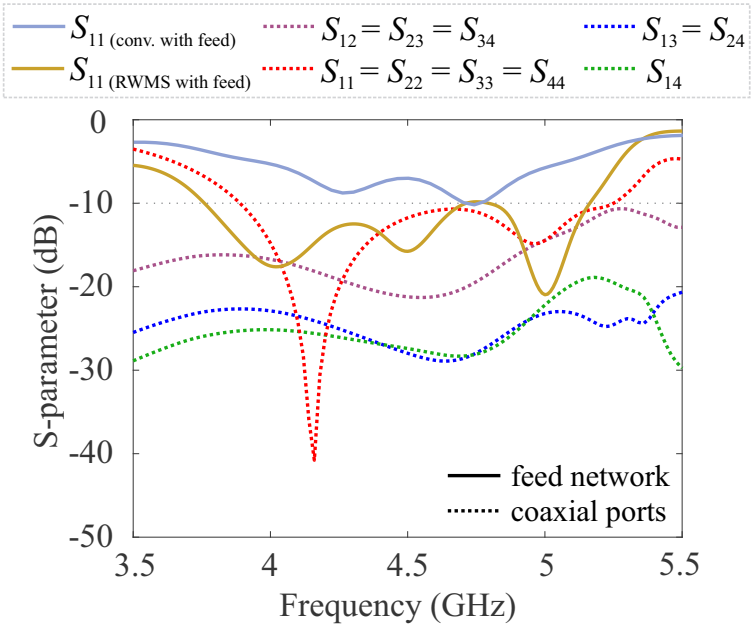

Figure 7.2: S-Parameters for the 1x4 RWMS Array.

To further examine the influence of coupling on the radiation behavior, the broadside realized gain is examined and plotted in Fig 7.3. At lower frequencies, the gain is the same when the RWMS is excited either by the feed network or the multiple coaxial probes; however, the two results begin to deviate slightly around 4.7 GHz, which is attributed to the more pronounced impact of coupling.

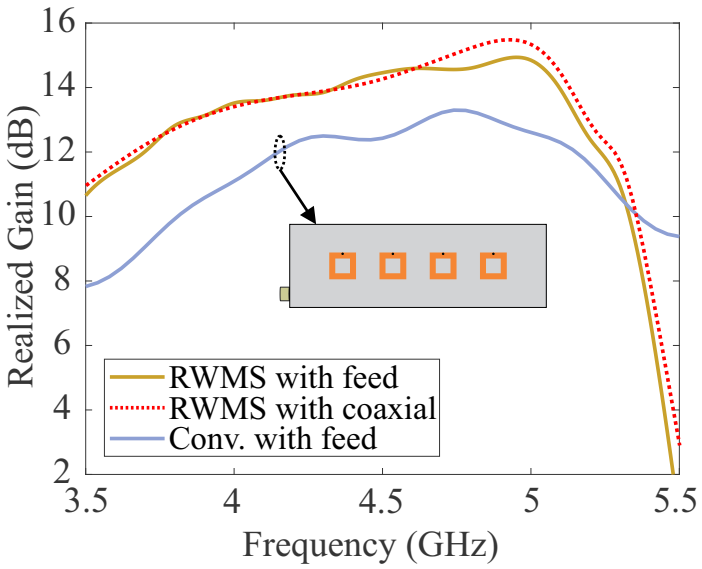

Figure 7.3: Broadside Realized Gain for the 1x4 RWMS Scheme.

The simulated realized gain, when the RWMS is excited with a feed network, ranges from 13.5 dB at 4 GHz and reaches up to 14.8 dB at 5 GHz. This observed high gain for the RWMS cannot be attained in the absence of metasurfaces, as displayed in Fig. 7.3. The aperture efficiency at 4.5 GHz is about 83% for the RWMS array, while it is only 52% for a conventional square ring array.

7.3 2x2 Circularly Polarized Metasurface Array

In addition to the linearly polarized RWMS structure, the RWMS design is extended to form a circularly polarized array. Since the RWMS is designed to excite surface waves on a single plane [30], circular polarization (CP) can be achieved by arranging orthogonal structures of RWMS fed with 90-degree phase difference. To achieve a gain comparable to the linear RWMS, a 2x2 RWMS scheme was designed, as displayed in Fig. 7.4a. The feed network parameters are: $l_1 = 50.875$ mm, $l_2 = 12$ mm, $l_3 = 20$ mm, $l_4 = 2.25$ mm, $l_5 = 7.2$ mm, $l_6 = 12$ mm, $l_7 = 37.87$ mm, $l_8 = 16.92$ mm, $l_9 = 0.69$ mm, $w_{50} = 1.1$ mm, $w_{35} = 1.9$ mm, $g_s = 2.74$ mm, $v = 1.143$

mm, $w_f = l_f = 6$ mm, $g_f = 2.45$ mm, $r_1 = 1.4$ mm, $r_2 = 6.5$ mm, and $t = 0.79$ mm.

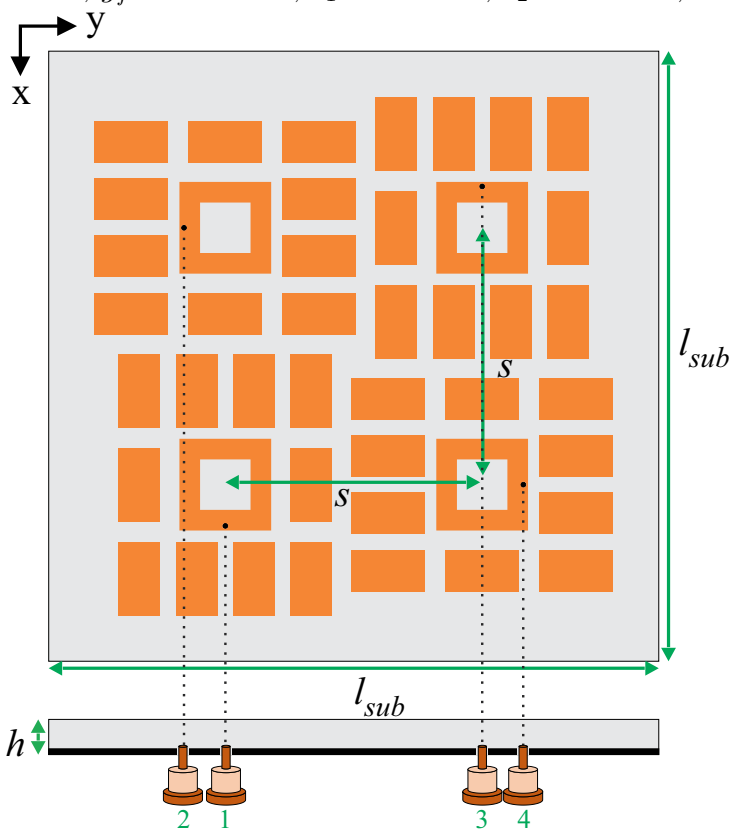

(a) Structure is fed with four coaxial ports

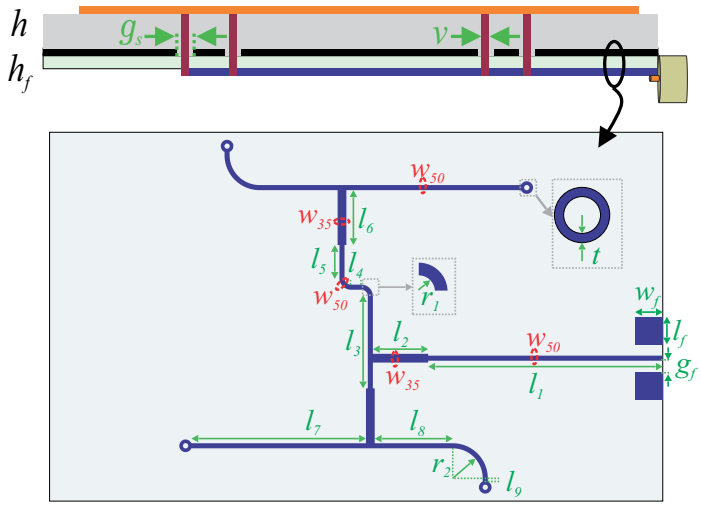

(b) Structure is fed with feed network

Figure 7.4: 2x2 Square Ring Elements Embedded Within Metasurface and Excited with (a) Four Coaxial Probes, and (b) Feed Network.

A square grounded dielectric is modeled with a thickness $h = 5.08$ mm, and a length $l_{sub} = 133$ mm. The spacing (s) along the $x-$ and $y-$ planes is 56 mm, which corresponds to $0.85\lambda_o$ at 4.5 GHz. The dielectric material, the dimensions of the ring elements, and the metasurface patches are identical to those given in the 1x4 array. Similar to the linear array, the coupling between the ring elements is investigated first by individually feeding the ring elements with four coaxial probes.

The simulated scattering parameters for the 2x2 circular polarized structure are depicted in Fig. 7.5. The -10 dB fractional bandwidth is slightly less than that for the 1x4 array, with a bandwidth of 25% from 3.9 to 5.0 GHz. The mutual coupling between vertically/horizontally adjacent ports and diagonally orientated ports is less than -20 dB, which is lower than those observed in the 1x4 linear array. This is attributed to the orthogonality of the excited surface waves, which agrees with the findings in [48]

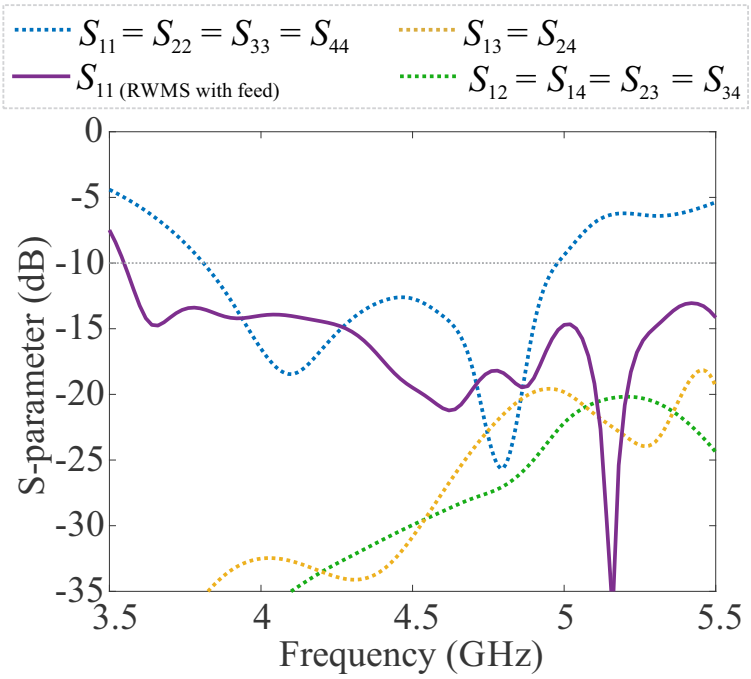

Figure 7.5: S-Parameters for the 2x2 RWMS Array.

Once the coupling was examined, a parallel feeding network was designed to excite all four ring elements with a single coaxial feed, as demonstrated in Fig. 7.4b. The feed was designed at the center frequency (4.5 GHz) to split the power equally among the four ring elements with 90° phase increment. The feed can dictate the sense of rotation of the CP (RHCP or LHCP) depending on the orientation of the phase increment (clockwise or counterclockwise); in this work, the feed was modeled to realize RHCP. The feed was designed on Rogers RT/Duroid-5880 substrate, which has a thickness (h_f) of 0.38 mm. Similar to the 1x4 linear array, the feeding substrate was stacked below the 2x2 circular array, and the outputs of the feed network are coupled to the ring elements using vias. The remaining dimensional parameters of the feeding network are detailed in the caption of Fig. 7.4. When the feed network excites the 2x2 RWMS, the -10 dB matching bandwidth is larger than that obtained with the four coaxial feeds. This is attributed to the parallel feed structures, which do not provide any isolation between the ports; therefore, any reflected power from any port can couple through to other ports resulting in small power return back to the feed.

To further analyze the performance of the 2x2 RWMS structure, the broadside realized gain and the axial ratio were examined. The simulated results for the two different feed approaches are presented in Fig. 7.6. When the structure is fed with individual probes, the realized gain is 13.5 dB at 4 GHz and reaches up to 15.8 dB at 4.8 GHz. Almost similar gain is attained when the feed network is utilized. However, there is a noticeable discrepancy in the axial ratio between the two feeding methods. For the individual feed approach, the broadside axial ratio (AR) is below 0.25 dB over the design frequency range; it is only below 3 dB over a more narrow frequency range (3.9 GHz to 5.1 GHz) when the structure is excited with the feed network. This can be explained by extracting the current that is delivered to each ring element.

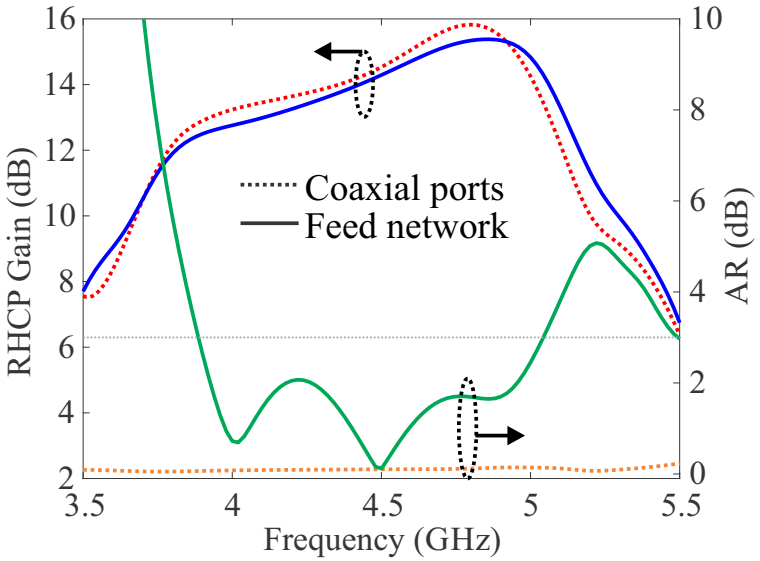

Figure 7.6: Broadside RHCP Gain and Axial Ratio for 2x2 RWMS Scheme.

The field calculator in HFSS is utilized to calculate the current around the vias that are connected to each ring element. As observed in Figure 7.7, the delivered current magnitude to each ring is relatively equal at the frequency range 4 to 5.1 GHz, which falls within the designed bandwidth. The current phase difference between the two neighboring ring element (ΔP_{ij}) is also calculated and plotted in Fig. 7.7. Around the designed frequency spectrum, the phase difference for most adjacent elements (ΔP_{12}, ΔP_{23}, ΔP_{34}) are fluctuating around 80°. However, the phase difference between ring 1 and 4 (ΔP_{14}) is slightly off, and it is oscillating around 110°. The reason for the magnitude and phase fluctuations is due to the poor isolation of the considered feeding network, which leads to magnitude and phase errors that influence the axial ratio [49]. The axial ratio, along with port isolation, can be enhanced by considering a Wilkinson power divider. Although the axial ratio degraded when the parallel feeding topology was incorporated, it is acceptable (below 3 dB) within the designed frequency range.

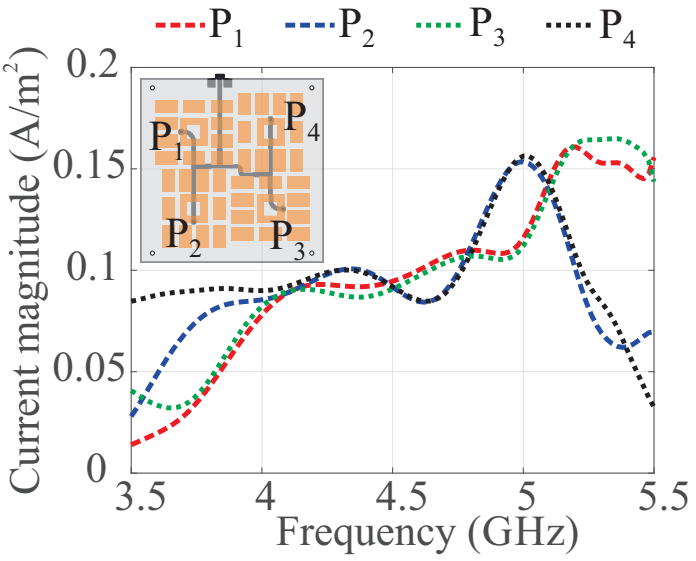

(a) Current Magnitude

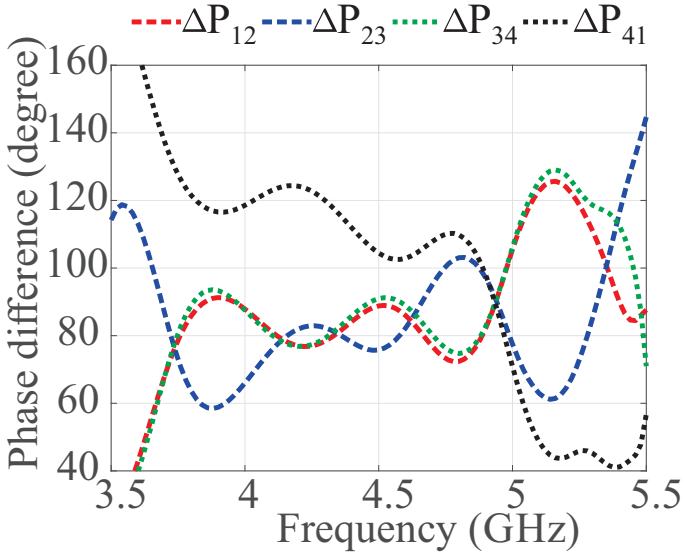

(b) Current Phase Difference

Figure 7.7: Delivered Current Magnitude to Each Ring Element (a), and Current Phase Difference Between Adjacent Elements (b).

7.4 Fabrication and Measurements

To experimentally validate the simulated data, the proposed 2x2 RWMS circular array was fabricated, as depicted in Fig. 6.8. Since linear and circular RWMS arrays share similar characteristics, only the circular array was considered for fabrication. The substrate materials and the dimensions of the fabricated design are identical to those given in Fig. 7.4. An edge mount SMA connector was soldered to the feed network substrate, as demonstrated in Fig. 7.8. Four nylon screws were placed at the corner to tighten the feed and RWMS substrates together and avoid any misalignment.

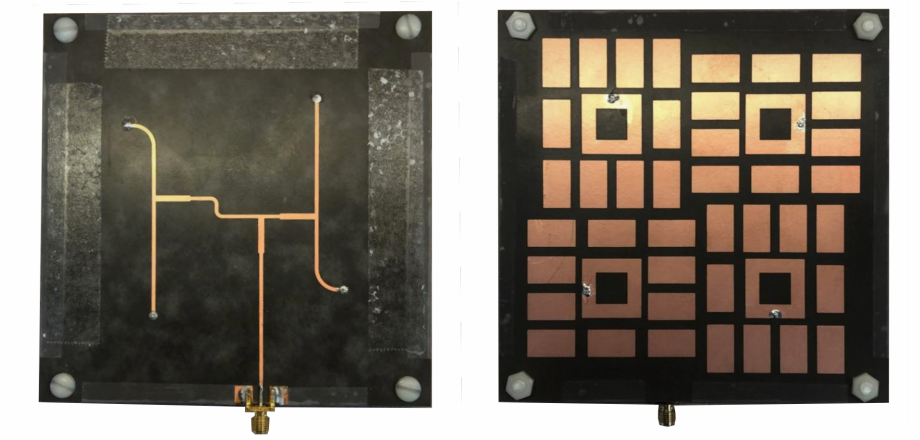

Figure 7.8: Top and Bottom Views of the Fabricated Prototype of the 2x2 RWMS Array Incorporated with the Feed Network.

The comparison of the measured and simulated results are displayed in Figs. 7.9 and 7.10. The simulated and measured S_{11} and the axial ratio show a good agreement; however, the broadside RHCP gain is about 1 dB lower than the simulated value. This deviation could be attributed to the fabrication tolerance and the stacking assembly error. The measured and simulated radiation patterns along different planes are displayed in Fig. 7.10; good agreement is observed between the simulated and measured patterns.

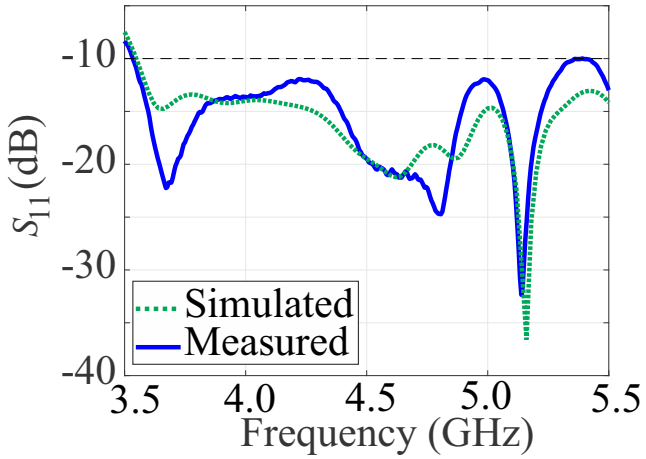

(a) S_{11}

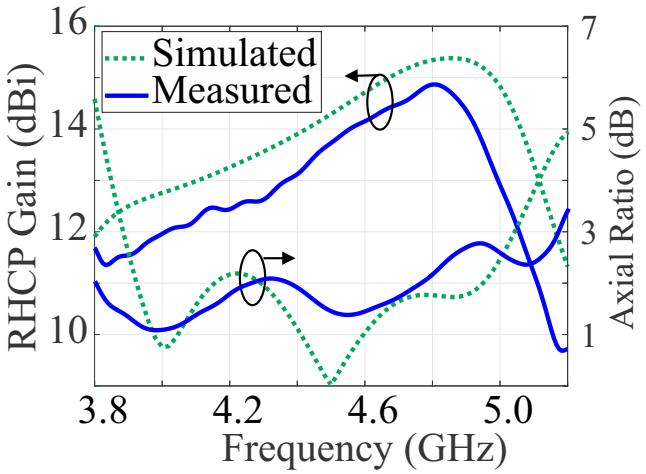

(b) RHCP Gain and Axial Ratio

Figure 7.9: Comparison Between Simulated and Measured Reflection Coefficient, RHCP Broadside Gain, and Axial Ratio.

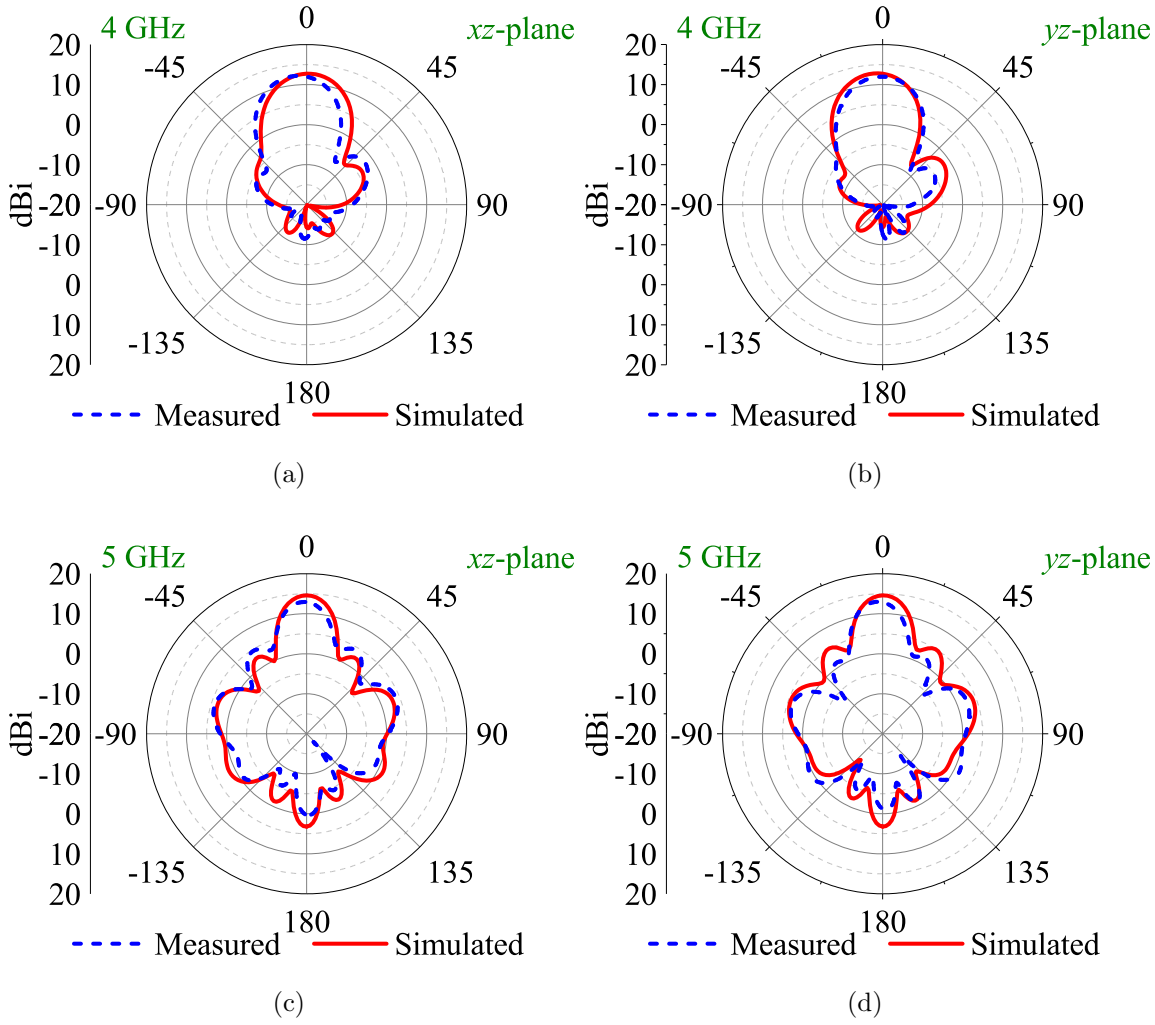

Figure 7.10: Simulated and Measured Radiation Patterns at xz- and yz-Planes.

Chapter 8

CONCLUSIONS AND FUTURE WORK

8.1 Conclusions

The directivities of radiating elements above different ground planes are investigated. Initially, the directivity of radiating element above PEC and PMC ground planes are analyzed. A far-field analytical model for electric and magnetic radiating elements, positioned horizontally above PEC and PMC ground planes are derived using image theory. The directivity, based on the analytical formulations, is compared with that simulated by the finite element method using HFSS; A good agreement is observed between them.

The fixed reflection phase and surface impedance possessed by PEC and PMC ground planes can be altered by modifying the structure geometry. Coated and corrugated PEC along with high impedance surface (HIS) are discussed as they are the most common techniques to modify the PEC behavior. A couple of HIS geometries are reviewed and the reflection phase using HFSS was obtained. In addition, the dispersion diagrams of different surfaces, that are analytically developed, compare very well with HFSS. The dispersion diagrams are then utilized to extract the possible surface waves resonances.

Furthermore, metasurfaces have been favorably utilized to enhance the performance of a circular loop and square-ring radiating elements. For the circular loop element, annular periodic patches are deployed around the loop to alleviate the high mismatch loss and enhance the radiation. When a single annular sector ring is deployed around the loop, a broadside directivity of 9 dBi is attained. To further en-

hance the directivity, the effective area is increased by adding another ring and form a *hybrid* ground plane, which leads to a directivity of 10.5 dBi. For the square ring element, various designs are analyzed to excite surface waves. Among the various possible designs of launching surface waves, the RWMS (Radiator Within Metasurfaces) provides wide matching bandwidths with stable broadside radiation. To further advance the radiation performance, the size of the ground plane is optimized resulting in a matching bandwidth of 27% and a maximum realized gain of 11.9 dBi. The height-profile of the final design ($0.07\lambda_o$), in addition to the simple probe feeding, makes the circular and rectangular design appealing for low-profile applications. To provide an experimental validation of the circular and rectangular loop designs, prototypes were fabricated; an excellent agreement between the simulation and measurement data was achieved.

To further enhance the directivity, a RWMS structure was extended to form different array schemes for linear and circular polarizations. The first arrangement was a 1x4 linear RWMS array, which resulted in a peak gain of 15 dBi in the broadside direction. The second scheme was for circular polarization where a 2x2 RWMS arrangement was adapted; a similar gain was attained with better isolation between the ports. To practically realize the two array schemes, a simple parallel feeding network was designed and incorporated with the arrays.

8.2 Future Work

The proposed square ring element is deployed with uniform periodic patches to enhance the broadside radiation. Furthermore, the design was extended to form arrays with different polarization. Further advancement can be considered as future work, and outlined in what follows:

- *tilted beam radiation*: The proposed RWMS design has many potential applica-

tions when broadside radiation is required. However, some applications require a low-profile design with a tilted beam. This can be accomplished by deploying nonuniform planar periodic patches (see Fig. 8.1) as for leaky wave structures. Most leaky wave designs utilize a monopole as an exciter, which might disturb the height profile. To maintain low profile, one can consider a square ring element embedded within nonuniform patches to form a leaky-wave structure.

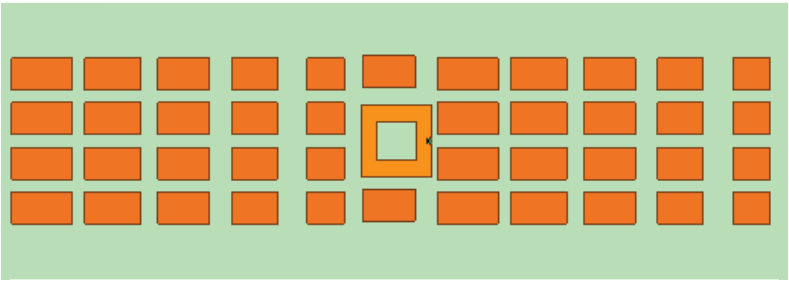

Figure 8.1: Geometry of RWMS Leaky-Wave Structure.

- *Beam scanning with surface wave array*: The proposed RWMS array was analyzed for broadside radiation, where mutual couplings has a less impact on the array performance. The couplings are more pronounced when the beam is directed non-broadside and can limit the scan angle. The capability of scanning the beam can be examined and compared to a conventional square ring array, as illustrated in Fig. 8.2. The study can include comparisons of directivity, beam scanning range, and side lobe level.

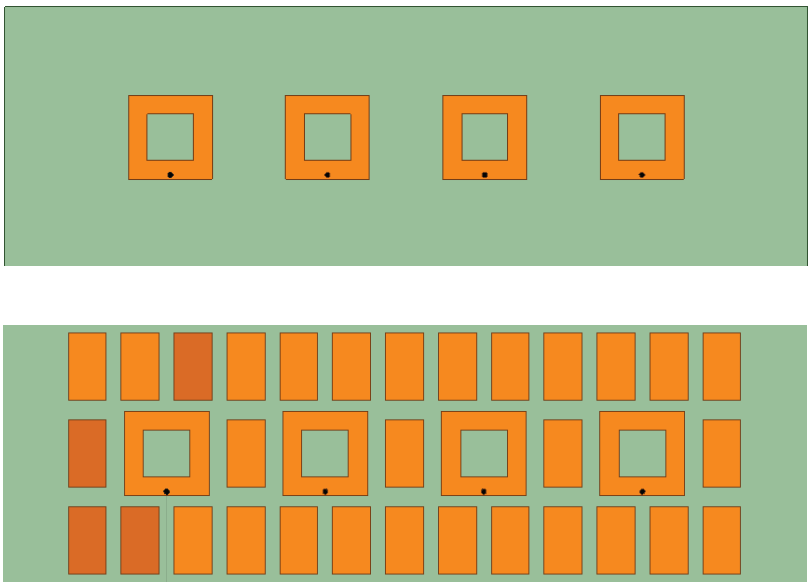

Figure 8.2: Geometry of Conventional Square Ring Array and RWMS Array.

- *Excitation of higher order mode of radiating element using surface waves*: Higher order modes are known for their high input resistances, which result in high reflection coefficient when it is excited with a 50-ohm feed. One possible approach to improve the reflection coefficient is to introduce periodic patches whose surface wave resonance is around the radiating element's resonance. This will improve the matching impedance and the overall radiation.

REFERENCES

[1] D. Sievenpiper, "High-impedance electromagnetic surfaces," Ph.D. dissertation, UCLA, Los Angeles (CA), 1999.

[2] A. P. Feresidis, G. Goussetis, S. Wang, and J. C. Vardaxoglou, "Artificial magnetic conductor surfaces and their application to low-profile high-gain planar antennas," *IEEE Transactions on Antennas and Propagation*, vol. 53, no. 1, pp. 209–215, Jan. 2005.

[3] M. Abu, M. K. A. Rahim, M. K. Suaidi, I. M. Ibrahim, and N. M. Nor, "A triple-band dipole antenna with 0.92 GHz AMC-HIS," in *2010 International Conference on Computer and Communication Engineering (ICCCE)*, May 2010, pp. 1–4.

[4] N. A. Abbasi and R. Langley, "A wideband printed monopole antenna over dual-band AMC," in *2010 Loughborough Antennas Propagation Conference*, Nov. 2010, pp. 221–224.

[5] F. Costa, A. Monorchio, S. Talarico, and F. M. Valeri, "An active high-impedance surface for low-profile tunable and steerable antennas," *IEEE Antennas and Wireless Propagation Letters*, vol. 7, pp. 676–680, 2008.

[6] C. A. Balanis, *Advanced Engineering Electromagnetics*. John Wiley & Sons, 2012.

[7] F. Yang and Y. Rahmat-Samii, *Electromagnetic Band Gap Structures in Antenna Engineering*. Cambridge university press Cambridge, UK, 2009.

[8] N. Rao and K. V. Dinesh, "Performance enhancement of a microstrip antenna by suppression of surface waves using EBG structure in multiple layer substrate," in *2011 IEEE-APS Topical Conference on Antennas and Propagation in Wireless Communications*, Sep. 2011, pp. 935–939.

[9] F. Yang and Y. Rahmat-Samii, "Microstrip antennas integrated with Electromagnetic Band Gap (EBG) structures: a low mutual coupling design for array applications," *IEEE Transactions on Antennas and Propagation*, vol. 51, no. 10, pp. 2936–2946, Oct. 2003.

[10] Y. Huang, A. De, Y. Zhang, T. K. Sarkar, and J. Carlo, "Enhancement of radiation along the ground plane from a horizontal dipole located close to it," *IEEE Antennas and Wireless Propagation Letters*, vol. 7, pp. 294–297, 2008.

[11] H. Li, K. W. Xu, X. B. Wang, R. Kanan, and L. X. Ran, "Low-profile circularly polarised loop antenna assisted with an effective PMC bandwidth," *Electronics Letters*, vol. 49, no. 16, pp. 978–979, Aug. 2013.

[12] M. A. Amiri, C. A. Balanis, and C. R. Birtcher, "Gain and bandwidth enhancement of a spiral antenna using a circularly symmetric HIS," *IEEE Antennas and Wireless Propagation Letters*, vol. 16, pp. 1080–1083, 2017.

[13] P. Deo, A. Mehta, D. Mirshekar-Syahkal, P. J. Massey, and H. Nakano, "Thickness reduction and performance enhancement of steerable square loop antenna using hybrid high impedance surface," *IEEE Transactions on Antennas and Propagation*, vol. 58, no. 5, pp. 1477–1485, May 2010.

[14] M. A. Amiri, C. A. Balanis, and C. R. Birtcher, "Design, simulation and antenna applications of spherical high impedance surfaces," in *2016 IEEE International Symposium on Antennas and Propagation (APSURSI)*. IEEE, 2016, pp. 1911–1912.

[15] M. A. Amiri, C. A. Balanis, and C. R. Birtcher, "Analysis, design, and measurements of circularly symmetric high-impedance surfaces for loop antenna applications," *IEEE Transactions on Antennas and Propagation*, vol. 64, no. 2, pp. 618–629, Feb. 2016.

[16] J. Sarrazin, A. C. Lepage, and X. Begaud, "Circular high-impedance surfaces characterization," *IEEE Antennas and Wireless Propagation Letters*, vol. 11, pp. 260–263, 2012.

[17] N. Llombart, A. Neto, G. Gerini, and P. de Maagt, "Planar circularly symmetric EBG structures for reducing surface waves in printed antennas," *IEEE Transactions on Antennas and Propagation*, vol. 53, no. 10, pp. 3210–3218, Oct. 2005.

[18] C. Wu, T. Makino, R. Maciejko, S. I. Najafi, and M. Svilans, "Simplified coupled-wave equations for cylindrical waves in circular grating planar waveguides," *Journal of Lightwave Technology*, vol. 10, no. 11, pp. 1575–1589, Nov. 1992.

[19] N. Llombart, A. Neto, G. Gerini, and P. de Maagt, "Planar circularly symmetric EBG structures for reducing surface waves in printed antennas," *IEEE Transactions on Antennas and Propagation*, vol. 53, no. 10, pp. 3210–3218, Oct. 2005.

[20] H. Boutayeb and T. A. Denidni, "Gain enhancement of a microstrip patch antenna using a cylindrical electromagnetic crystal substrate," *IEEE Transactions on Antennas and Propagation*, vol. 55, no. 11, pp. 3140–3145, Nov. 2007.

[21] S. R. Best, "Improving the performance properties of a dipole element closely spaced to a PEC ground plane," *IEEE Antennas and Wireless Propagation Letters*, vol. 3, no. 1, pp. 359–363, Dec. 2004.

[22] A. Vallecchi, J. R. D. Luis, F. Capolino, and F. D. Flaviis, "Low profile fully planar folded dipole antenna on a high impedance surface," *IEEE Transactions on Antennas and Propagation*, vol. 60, no. 1, pp. 51–62, Jan. 2012.

[23] Z. N. Chen, Y. Juan, X. Qing, and W. Che, "Enhanced radiation from a horizontal dipole closely placed above a PEC ground plane using a parasitic strip," in *IEEE Transactions on Antennas and Propagation*, Jul. 2016, pp. 4868–4871.

[24] R. Gonzalo, P. De Maagt, and M. Sorolla, "Enhanced patch-antenna performance by suppressing surface waves using photonic-bandgap substrates," *IEEE Transactions on Microwave Theory and Techniques*, vol. 47, no. 11, pp. 2131–2138, Nov 1999.

[25] Fan Yang and Y. Rahmat-Samii, "Microstrip antennas integrated with electromagnetic band-gap (ebg) structures: a low mutual coupling design for array applications," *IEEE Transactions on Antennas and Propagation*, vol. 51, no. 10, pp. 2936–2946, Oct 2003.

[26] F. Yang, A. Aminian, and Y. Rahmat-Samii, "A novel surface-wave antenna design using a thin periodically loaded ground plane," *Microwave and Optical Technology Letters*, vol. 47, no. 3, pp. 240–245, 2005. [Online]. Available: https://onlinelibrary.wiley.com/doi/abs/10.1002/mop.21136

[27] F. Costa, O. Luukkonen, C. R. Simovski, A. Monorchio, S. A. Tretyakov, and P. M. de Maagt, "Te surface wave resonances on high-impedance surface based antennas: Analysis and modeling," *IEEE Transactions on Antennas and Propagation*, vol. 59, no. 10, pp. 3588–3596, Oct 2011.

[28] F. Yang, Y. Rahmat-Sami, and A. Kishk, "Low-profile patch-fed surface wave antenna with a monopole-like radiation pattern," *IET Microwaves, Antennas Propagation*, vol. 1, no. 1, pp. 261–266, February 2007.

[29] M. Alharbi, C. A. Balanis, C. R. Birtcher, and H. N. Shaman, "Hybrid circular ground planes for high-realized-gain low-profile loop antennas," *IEEE Antennas and Wireless Propagation Letters*, vol. 17, no. 8, pp. 1426–1429, Aug 2018.

[30] M. S. Alharbi, C. A. Balanis, and C. R. Birtcher, "Performance enhancement of square-ring antennas exploiting surface-wave metasurfaces," *IEEE Antennas and Wireless Propagation Letters*, vol. 18, no. 10, pp. 1991–1995, Oct 2019.

[31] M. S. Alharbi, M. A. Alyahya, S. Ramalingam, A. Modi, C. A. Balanis, and C. R. Birtcher, "Metasurfaces for reconfiguration of multi-polarization antenna and van atta reflector arrays," 2020, submitted to Electronic Journal.

[32] C. A. Balanis, *Antenna Theory: Analysis and Design.* John Wiley & Sons, 2016.

[33] F. Yang and Y. Rahmat-Samii, "Reflection phase characterizations of the EBG ground plane for low profile wire antenna applications," *IEEE Transactions on Antennas and Propagation*, vol. 51, no. 10, pp. 2691–2703, Oct. 2003.

[34] H. Zhai, K. Zhang, S. Yang, and D. Feng, "A low-profile dual-band dual-polarized antenna with an AMC surface for WLAN applications," *IEEE Antennas and Wireless Propagation Letters*, no. 99, pp. 1–1, 2017.

[35] S. T. Peng, T. Tamir, and H. L. Bertoni, "Theory of periodic dielect waveguides," *IEEE Transactions on Microwave Theory and Techniques*, vol. 23, no. 1, pp. 123–133, 1975.

[36] O. Luukkonen, C. Simovski, G. Granet, G. Goussetis, D. Lioubtchenko, A. Risnen, and S. A. Tretyakov, "Simple and accurate analytical model of planar grids and high-impedance surfaces comprising metal strips or patches," *IEEE Trans. Antennas Propagat.*, vol. 56, no. 6, pp. 1624–1632, 2008.

[37] R. Garg, *Microstrip Antenna Design Handbook*. Artech House, 2001.

[38] S. Oh and L. Shafai, "Investigation into polarization of unloaded and loaded microstrip square-ring antennas," *IEEE Transactions on Antennas and Propagation*, vol. 56, no. 10, pp. 3129–3135, Oct 2008.

[39] P. M. Bafrooei and L. Shafai, "Characteristics of single- and double-layer microstrip square-ring antennas," *IEEE Transactions on Antennas and Propagation*, vol. 47, no. 10, pp. 1633–1639, Oct 1999.

[40] R. G. Quarfoth, "Anisotropic artificial impedance surfaces (Ph. D. thesis)," *UCLA, San Diego (CA)*, 2014.

[41] G. Feng, L. Chen, X. Xue, and X. Shi, "Broadband surface-wave antenna with a novel nonuniform tapered metasurface," *IEEE Antennas and Wireless Propagation Letters*, vol. 16, no. 8, pp. 2902–2905, Aug 2017.

[42] F. H. Lin and Z. N. Chen, "Low-profile wideband metasurface antennas using characteristic mode analysis," *IEEE Trans. Antennas Propagat.*, vol. 65, no. 4, pp. 1706–1713, 2017.

[43] W. Yang, S. Chen, W. Che, Q. Xue, and Q. Meng, "Compact high-gain metasurface antenna arrays based on higher-mode siw cavities," *IEEE Trans. Antennas Propagat.*, vol. 66, no. 9, pp. 4918–4923, 2018.

[44] H. L. Zhu, S. W. Cheung, K. L. Chung, and T. I. Yuk, "Linear-to-circular polarization conversion using metasurface," *IEEE Trans. Antennas Propagat.*, vol. 61, no. 9, pp. 4615–4623, 2013.

[45] S. X. Ta and I. Park, "Low-profile broadband circularly polarized patch antenna using metasurface," *IEEE Trans. Antennas Propagat.*, vol. 63, no. 12, pp. 5929–5934, 2015.

[46] Z. Wu, L. Li, Y. Li, and X. Chen, "Metasurface superstrate antenna with wideband circular polarization for satellite communication application," *IEEE Antennas and Wireless Propagation Letters*, vol. 15, pp. 374–377, 2016.

[47] S. X. Ta and I. Park, "Compact wideband circularly polarized patch antenna array using metasurface," *IEEE Antennas and Wireless Propagation Letters*, vol. 16, pp. 1932–1936, 2017.

[48] R. R. Ramirez and F. D. Flaviis, "A mutual coupling study of linear and circular polarized microstrip antennas for diversity wireless systems," *IEEE Trans. Antennas Propagat.*, vol. 51, no. 2, pp. 238–248, 2003.

[49] D. M. Pozar and D. H. Schaubert, *Microstrip Antennas: The Analysis and Design of Microstrip Antennas and Arrays.* IEEE Press, 1995.